Electronic structure of topological quantum materials probed by angle-resolved photoelectron spectroscopy



Niels B. M. Schröter

Wolfson College

University of Oxford

A thesis submitted for the degree of

Doctor of Philosophy

Michaelmas 2017

Meinen lieben Eltern in Dankbarkeit gewidmet.

Abstract

This thesis investigates the electronic structure of four separate topological quantum material systems by angle-resolved photoelectron spectroscopy (ARPES):

1. LaBi is a semimetal with an extremely large magnetoresistance (XMR) that remains unsaturated even at large magnetic fields. Our ARPES measurements of LaBi indicate the existence of a strong topological phase that may be unique within the family of lanthanum monopnictides. Additionally, our characterization of its bulk electronic structure finds a large imbalance between the electron and hole carrier densities, which challenges the previously assumed scenario of perfect carrier compensation as the origin of the XMR.

2. Three dimensional topological insulators (TIs) can be divided into two classes: strong TIs that host TSSs on all surfaces, and weak TIs, which host TSSs only on some surfaces, which are expected to harbour novel physical phenomena. Yet, despite multiple theoretical proposals and experimental reports, "smoking-gun" evidence for the existence of a weak topological phase is still elusive. Here, by performing ARPES measurements for the surface states of two distinct crystal surfaces, we can conclusively confirm the existence of a weak topological phase in the semimetal $TaSb_2$, which may be related to its negative longitudinal magnetoresistance. Additionally, we present evidence that $TaAs_2$ and $NbAs_2$ are also topologically nontrivial.

3. Graphene is predicted to be a quantum spin Hall insulator, but due to the weak spin-orbit coupling (SOC) of carbon, the predicted bulk energy gap at its Dirac point remains unresolved. Here, we grow ultrathin layers of germanium on Au(1 1 1) in the attempt to realize germanene, a buckled honeycomb structure of germanium atoms, which is predicted to host a similar band structure as graphene with a much larger energy gap. Our ARPES studies of those films reveal the existence of multiple Dirac-like bands that can be tuned by changing the film thickness.

4. The family of A_3BO antiperovskites (A=Ca, Sr; B=Sn, Pb) is predicted to form topological crystalline insulators (TCIs). Our ARPES studies of intrinsically hole doped Sr_3SnO, Ca_3PbO, and Sr_3PbO find good agreement with bulk band structure calculations, but cannot probe the predicted bulk and surface Dirac cones in the unoccupied states. For the superconducting hole doped Sr_3SnO, which may realize unconventional odd-parity Cooper pairing, we can resolve a controversial question about its Fermi surface morphology that may be relevant for its pairing mechanism.

Acknowledgments

The past three years in Oxford have been an incredible time that will shape the rest of my life, and I would like to sincerely thank everyone who made it such an enjoyable experience.

I would like to start with thanking my supervisor, Yulin Chen, for his guidance and the privilege to be his student. I deeply admire his physical intuition and incredible commitment to science, and I am grateful for his encouraging support of my own ideas (at least of the good ones), as well as his honest advice. I learned a lot from him, most importantly to make my own scientific judgments, and the fact that I am pursuing a scientific career after my graduate studies is to a large extend due to his influence.

I would like to thank Phil King and Andrew Boothroyd for acting as examiners of this thesis, your service is greatly appreciated.

Next in line are the other members of the Chen group in Oxford, Cheng Chen, Han Peng, Sandy Ekahana, Yiwei Li, and Ding Pei. I am deeply grateful for your help as collegues, but also your friendship. Now that I am leaving I feel sorry for not spending more time with you (and for not learning Chinese), but I hope that our lives will remain entangled, even though we may end up scattered around the globe. If there is ever anything that I can help you with, please do not hesitate to get in touch!

I also would like to thank the more senior members of the Chen group for their support: Juan Jiang and Xiang Xu for our great collaboration on many projects and our remote beamtimes via QQ at ALS, Haifeng Yang for being the most friendly, selfless, and supporting person I ever met (thus becoming a true role model), and Defa Liu, Aiji Liang, Zhongkai Liu and Lexian Yang for their help during beamtimes, which also goes to their students Lei Shen, Yujie Chen and Chengwei Wang.

During my time in Oxford I also made many friends outside my group who either actively helped me with the results presented here, or contributed to my overall scientific development. First and foremost I would like to thank Matthew Watson and Fernando de Juan for their support and encouragement, working with you was always great fun and I learned a lot from our discussions. I hope that we will stay in touch in the future! I would also like to thank Jian Rui Soh, Liam Duffy, and Thorsten Hesjedal for their support during experiments and paper writing, our scientific discussions, and general banter. I would like to thank Nat Davies for teaching me how to use the supernova and his generally helpful attitude.

Most importantly, I would also like to thank my many external collaborators outside Oxford. I would like to thank Wujun Shi, Shu-Chun Wu and Binghai Yan for their theory support, and Yanfeng Guo, Claus Muehle, Andreas Rost, Nitesh Kumar, Kaustuv Manna, Chandra Shekhar, and Claudia Felser for supplying us with high quality single crystals.

Another important group to thank are the beamline scientists who build and maintained the setups that I used to collect ARPES data. Most of the data in this thesis was taken at beamline I05 of the Diamond Light Source. Moritz Hoesch, Pavel Dudin, Timur Kim, and Hideaki Iwasawa: You guys build an incredible machine, thank you so much for it! I especially enjoyed the opportunity to directly collaborate with Timur on the Ge thin film project (for which I also acknowledge the support of Luke Rhodes, Qixin Yang and Katie Winter), as well as with Hideaki on various superconductors. I also would like to thank the teams at Elettra, Alexei Barinov and Viktor Kandyba from Spectromicroscopy, and Ivana Vobronik, Jun Fujii and Prenab Das from APE, for their extremely friendly and helpful support.

I would like to thank Dieter Schöpplein for paving the way for this thesis in his classroom, you sparked my excitement for physics that still keeps me going.

I would like to thank my family, especially my parents, for their unconditional support and love, and the freedom they granted me to make my own way in life.

Finally, I would like to thank my fiancée Sarah for her incredible patience and understanding, even in the face of insane working hours and a lot of traveling. Oxford was just the first chapter of a life full of adventures with you, and I am excited to live with you through the rest of it!

Preface

The theoretical prediction and subsequent experimental discovery of the topological quantum spin Hall insulator in 2007 marked the beginning of a new era in condensed matter physics. From the concept of topology, whose physical significance was recognized at least since in the 1970s, emerged a new field that led to the subsequent discovery of three-dimensional topological insulators, Dirac semimetals, and Weyl semimetals, which borrowed concepts from particle physics to realize novel phenomena in solids. The hallmark of these topological materials is the existence of so called topological surface states on the interface to their surrounding, which may become useful for applications ranging from spintronics to quantum computing. Due to its surface sensitivity, angle-resolved photoelectron spectroscopy (ARPES) became one of the most important tools to investigate those surface states with momentum resolution, which enabled researchers to uncover the topological nature of a large number of often long known materials. Additionally, ARPES can also probe the bulk band structure for many materials, which makes it a powerful method to investigate the interplay between topology and other phenomena, such as magnetotransport or superconductivity.

Due to its versatility, ARPES was used as the primary tool in this thesis to investigate the electronic structure of novel topological materials. The objectives of our studies were twofold: on the one hand, we wanted to investigate new materials for already know topological phenomena – such as strong topological insulators, quantum spin-hall insulators, or topological crystalline insulators – which promise

improvements over the existing material base, or combine a nontrivial topology with other functionalities. On the other hand, we aimed to find novel topological phases that have not yet been conclusively discovered, such as weak topological insulators.

The presentation of our results will be organized as follows: after two introductory chapters about topological band theory and angle-resolved photoelectron spectroscopy, chapter 3 will present out ARPES study of lanthanum bismuth, a semimetal that hosts a strong topological phase and displays an extremely large, unsaturated magnetoresistance. In chapter 4, we will describe our discovery of a weak topological phase in a family of transition-metal dipnictides. Chapter 5 describes the growth and ARPES study of ultrathin Ge films of various thickness, which was aimed to realize a new type of quantum spin Hall insulator with larger band gap. The final chapter 6 describes our ARPES study of three oxide compounds in the antiperovskite material family that are predicted to be topological crystalline insulators, one of which may host unconventional superconductivity.

Niels B. M. Schröter

Wolfson College and Clarendon Laboratory

Oxford, United Kingdom

Autumn 2017

Contents

1 Introduction to topological band theory **1**
1.1 Topological invariants, Berry phase, and the integer quantum Hall effect 2
1.2 Topological invariants in time-reversal invariant insulators 9
References 18

2 Introduction to angle-resolved photoelectron spectroscopy (ARPES) **20**
2.1 Theory of photoemission 20
2.2 Synchrotron-based ARPES instrumentation 26
References 30

3 Discovery of a strong topological phase and large carrier density imbalance in the semimetal LaBi **33**
3.1 Previous experimental and theoretical studies of the lanthanum and yttrium monopnictides 34
3.2 Open research questions that are motivating the ARPES study of LaBi 43
3.3 Discovery of topological surface states in LaBi 44
3.4 Discovery of large carrier density imbalance in LaBi 51
3.5 Discussion of the results and perspectives for future research 58
References 61

4 Discovery of a weak topological phase in the semimetal $TaSb_2$ **69**
4.1 Previous theoretical and experimental studies of weak topological insulators 70
4.2 Prediction of weak topological phase and magnetotransport effects in the transition-metal dipnictide family TmX (Tm=Ta, Nb; X=As, Sb) 75
4.3 ARPES study of transition-metal dipnictides, and discovery of a weak topological phase 78
4.4 Discussion of the results and perspectives for future research 93
References 95

5 Discovery of Dirac-like bands in the monolayer limit of ultrathin Ge films on Au(111) **100**
5.1 Background and previous experiments on graphene analogues with strong spin-orbit coupling 101
5.2 Characterization of ultrathin Ge films grown on Au(1 1 1) 104

5.3 Band structure evolution with film thickness 107
5.4 Discussion and prospects for further study 113
References 115

6 Electronic structure of topological crystalline insulator candidates in the antiperovskite family A_3BO (A=Ca, Sr; B=Sn, Pb) 120
6.1 Introduction to topological crystalline insulators (TCIs) 121
6.2 TCI phase in the antiperovskite family A_3BO (A=Ca, Sr; B=Sn, Pb) 124
6.3 ARPES study Sr_3SnO, $(Ca_{1-x}La_x)_3PbO$, and Sr_3PbO 128
6.4 Discussion of the results and prospects for further study 132
References 133

7 Summary and conclusions 138
7.1 Investigation of new candidate materials of existing topological phases 138
7.2 Discovery of a weak topological phase in a family of transition-metal dipnictides 141

Publications

Publications and manuscripts related to work covered in this thesis

- **Niels B. M. Schröter**, Matthew D Watson, Liam B Duffy, Moritz Hoesch, Yulin Chen, Thorsten Hesjedal and Timur K Kim
  Emergence of Dirac-like bands in the monolayer limit of epitaxial Ge films on Au(1 1 1)
  2D Materials 4, 031005 (2017)

- J. Jiang*, **N. B. M. Schröter***, S. C. Wu, C. Shekhar, H. Peng, X. Xu, Z. K. Liu, L. X. Yang, C. Chen, H. F. Yang, C.-C. Hwang, S.-K. Mo, C. Felser, B. H. Yan, and Y. L. Chen
  *these authors contributed equally
  Observation of Topological Surface States and Strong Electron/hole Imbalance in Extreme Magnetoresistance Compound LaBi
  (under review)

- **N. B. M. Schröter**, J. Jiang, W. Shi, F. de Juan, Y. F. Guo, L. X. Yang, C. Cheng, H. Peng, S. A. Ekahana, Y. Li, B. H. Yan, Y. L. Chen
  Discovery of a weak topological phase in the semimetal $TaSb_2$
  (to be submitted)

Publications related to work not covered in this thesis

- Han Peng*, **Niels B. M. Schröter***, Jianbo Yin, Huan Wang, Ting-Fung Chung, Haifeng Yang, Sandy Ekahana, Zhongkai Liu, Juan Jiang, Lexian Yang, Teng Zhang, Cheng Chen, Heng Ni, Alexey Barinov, Yong P. Chen, Zhongfan Liu, Hailin Peng, Yulin Chen
  *these authors contributed equally
  Substrate Doping Effect and Unusually Large Angle van Hove Singularity Evolution in Twisted Bi- and Multilayer Graphene
  Advanced Materials 29, 1606741 (2017)

- C. Chen, X. Xu, J. Jiang, S. -C. Wu, Y. P. Qi, L. X. Yang, M. X. Wang, Y. Sun, **N.B.M. Schröter**, H. F. Yang, L. M. Schoop, Y. Y. Lv, J. Zhou, Y. B.

Chen, S. H. Yao, M. H. Lu, Y. F. Chen, C. Felser, B. H. Yan, Z. K. Liu and Y.L. Chen
Dirac Line-nodes and Effect of Spin-orbit Coupling in Non-symmorphic Critical Semimetal MSiS (M=Hf, Zr)
Physical Review B, 95, 125126 (2017)

Chapter 1

Introduction to topological band theory

It is one of the grand challenges in condensed matter physics to define and discover new *phases of matter*. A phase can be understood as a state of matter that maintains certain properties under continuous changes of the system parameters, until eventually a phase transition to a different state occurs where those properties change [1]. An influential theory to classify phases of matter is due to Landau, which describes phase transitions as spontaneous breaking of local symmetries, which leads to the emergence of nonzero local order parameters in the lower symmetry phase [2]. Examples for such local symmetry breaking phase transitions are lattice formation (which breaks translational symmetry), magnetic ordering (which breaks time reversal and approximate spin rotation symmetry), ferroelectricity (which breaks inversion symmetry), and nematic ordering in liquid crystals (which breaks local rotational symmetry).

However, in the early 1970s, it was realized that not all phase transitions can be identified by the breaking of local symmetries and emergence of local order parameters. Instead, phase transitions were identified that are characterized by a change of so called *topological invariants*. For laying the theoretical groundwork of the field of topological phases and phase transitions, David Thouless, Duncan Haldane, and

Michael Kosterlitz were awarded the Nobel Prize in Physics in 2016. The work of Thouless and Haldane led to the development of *topological band theory*, which forms the theoretical bedrock of this thesis and will be discussed in the following sections. We will begin with presenting a pedagogical introduction to topological invariants and their application to describe the integer quantum Hall effect. Subsequently, we will discuss the extension of topological band theory to time-reversal invariant systems, which will be relevant to understand the experimental results presented in the following chapters.

1.1 Topological invariants, Berry phase, and the integer quantum Hall effect

Topological invariants are used in mathematics to classify spaces [3]. Intuitively, one can imagine a topological space as a geometric figure that can be deformed into another one. As long as this deformation is smooth, i.e. does not involve any tearing or puncturing, the topological classification remains constant, which is reflected by a constant topological invariant. An illustrative example for an algebraic topological invariant is the so called Euler charactistic X, which can be defined for polyhedra as

$$X = \text{Vertices} - \text{Edges} + \text{Faces}. \tag{1.1}$$

For instance, when continuously deforming a pyramid with a triagonal base (four vertices, six edges, four faces; $X = 2$) into an octahedron (six vertices, 12 edges, eight faces; $X = 2$) and then into a cube (eight vertices, 12 edges, six faces; $X = 2$), the Euler Invariant remains constant, which means that all these figures can be considered equivalent with regards to this topological classification. However, when punching a quadratic hole into the cube (16 vertices, 32 Edges, 16 faces; $X = 0$), the Euler characteristic changes, which reflects a change in the topological classification. More

generally, for figures that are bound by closed surfaces, the Euler characteristic can be expressed as a surface integral of the Gaussian curvature K [4]

$$X = \frac{1}{2\pi} \int_S K \, dA. \tag{1.2}$$

The Gaussian curvature at any given point on the surface is the product of the two principle curvatures at that point $K = k_1 k_2$. Those principle curvatures k_1, k_2 can be understood as follows: Imagine a surface in three-dimensional Euclidean space. Each point can be assigned a normal vector on the surface. All planes that contain this normal vector are intersecting the surface, which defines curves on the surface that can be assigned a normal curvature. The maximum and minimum values of the normal curvature at that point are called the principle curvatures [5]. When calculating the Euler characteristic for a sphere, we find that the Gaussian curvature is $K = 1/R^2$ everywhere on the surface, which leads to an Euler characteristic of $X = 2$. For a Torus, the Gaussian curvature is negative on the inside whilst positive on the outside, which overall cancels out and gives an Euler characteristic of $X = 0$. The celebrated Gauss-Bonnet theorem of mathematics states that the Euler characteristic for closed surfaces can generally be expressed as

$$X = 2 - 2g, \tag{1.3}$$

where g is the genus, which can be understood as the number of holes in the figure [4]. This shows that the topological classification of spaces by topological invariants does not depend on local details, such as the number of vertices of a geometrical figure, but rather depends on global properties of the space. This insight will become important for our subsequent discussion of the robustness of edge and surface states at the interface between topological materials and their trivial surroundings.

1.1.1 The Berry phase

It turns out that in the quantum mechanical description of the integer quantum Hall effect, which can be considered as the first application of topological band theory, a topological invariant can be defined by a similar integral of a curvature over a closed surface as presented in Equation (1.2). This curvature is the so called Berry curvature, which is related to the Berry phase. To understand the concept of the Berry phase, it is instructive to consider the following classical thought experiment, which is inspired by Griffiths [6]: Imagine transporting a pendulum over a closed surface on a globe that is fixed in space. Let us assume that the pendulum is initially swinging in a plane on the North pole (the direction along which the weight is swinging is represented by the red vectors in Figure 1.1). When slowly transporting the pendulum form the North pole to the equator along a longitude line, it remains swinging in the original plane that it started swinging in. Once the pendulum reaches the equator, we will slowly transport the pendulum eastwards along the equator line. If this transport is slow enough, the pendulum will slowly rotate the plane in which it is swinging with respect to the axis of the globe by changing to a different longitude line. When the pendulum is subsequently transported back to the north pole along a new longitude line, the pendulum will swing in a different plane compared to the initial starting position, as can be seen by the angle between the red vectors at the north pole in Figure 1.1, which can be considered as a change of its phase. Such a phase that is acquired purely due to the geometry of the path taken is called a *geometric phase*. Interestingly, the *Foucault pendulum* is an example of such a classical geometric phase, except that instead of transporting the pendulum over a fixed globe, the earth's rotation will cause an equivalent transport along a closed loop over a sphere that results in an observable rotation of the plane in which the pendulum swings. In quantum mechanics, there is a similar phenomenon of a phase that is acquired due to the geometry of a closed path over which a quantum state is transported in parameter space. This phase is called Berry phase and we will again follow Griffiths [6] to understand this phenomenon.

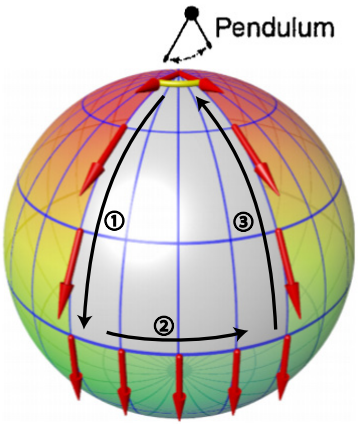


Figure 1.1: **Geometric phase of a pendulum due to adiabatic transport over a closed path on a globe.** The red arrows indicate direction along which the weight of the pendulum is swinging. The black arrows indicate the direction along which the pendulum is transported. Figure adapted from Refs. [6, 17].

Let us assume that the Hamiltonian H of our quantum mechanical system depends on some set of parameters $\boldsymbol{R}(t) = (R_1(t),\ R_2(t),\ R_3(t),\ ...)$, which in turn depend on the time t. If the system is initially in the n^{th} eigenstate $\psi_n(t=0)$ of the Hamiltonian $H(\boldsymbol{R}(t=0))$, and the parameters are subsequently changed sufficiently slowly (i.e. at a time scale much smaller than $2\pi/E_{ab}$, where E_{ab} is the energy difference between some eigenvalues of the Hamiltonian [7]), then the adiabatic theorem states that the system remains in the n^{th} eigenstate over time $\psi_n(t)$, but the final wave function $\Psi_n(t)$ acquires some phase factors

$$\Psi_n(t) = \exp\left(-\frac{1}{\hbar}\int_0^t E_n(t')dt'\right)\exp\left(i\gamma_n(t)\right)\psi_n(t), \tag{1.4}$$

where the first factor includes the so called *dynamical phase* that depends on the instantaneous energy eigenvalues $E_n(t')$ at time t', while the second factor includes the so called *geometric phase* $\gamma_n(t)$. If the Hamiltonian returns to its original position in parameter space after some time T, thus performing a closed loop C, then the

geometric phase takes the form

$$\gamma_n(T) = \oint_C \underbrace{i\langle\psi_n|\nabla_{\boldsymbol{R}}|\psi_n\rangle}_{:=A_n(\boldsymbol{R})} d\boldsymbol{R} \tag{1.5}$$

which is called the Berry phase, and the integrand $A_n(\boldsymbol{R})$ is called the Berry connection. Note that this phase, in contrast to the dynamical phase, only depends on the path taken in parameter space, and not on the time by which it was traversed (hence the name). For a three dimensional parameter space, Stokes theorem can be applied to transform the Berry phase into a surface integral over the surface S enclosed by the loop C

$$\gamma_n(T) = \int_S \underbrace{\nabla \times A_n(\boldsymbol{R})}_{:=\boldsymbol{B_n}(\boldsymbol{R})} \cdot d\boldsymbol{S} \tag{1.6}$$

where $\boldsymbol{B}(\boldsymbol{R})$ is the so called Berry curvature. Note that a gauge transformation such as $\psi_n \to \psi_n \exp(i\eta(\boldsymbol{R}))$ with some scalar function $\eta(\boldsymbol{R})$ will change the Berry connection, but leaves the Berry curvature invariant, which indicates that the Berry phase is a gauge invariant physical quantity[1]. Indeed, it turns out that it can be observed directly, e.g. in ultra cold neutron experiments [8].

The fact that the berry phase is gauge invariant can be used to show that the integral of the Berry curvature over a closed surface is quantized [7], which will become important for the description of the integer quantum Hall effect that follows below. Imagine a closed loop in parameter space that defines the Berry phase line integral. Consider two surfaces that are enclosed by the same loop. One surface S_1 forms the upper half of a sphere, and the other surface S_2 forms the lower half of a sphere. The integral of the Berry curvature over both of these surfaces can only differ by modulo 2π, since the Berry phase is an observable quantity, so $\int_{S_1} \boldsymbol{B}(\boldsymbol{R}) \cdot d\boldsymbol{S} = \int_{S_2} \boldsymbol{B}(\boldsymbol{R}) \cdot d\boldsymbol{S} + 2\pi n$, where n is an integer. Since the curl defines the direction for $d\boldsymbol{S}$, it will point into the sphere for one of the two integrals. If we reverse the

[1] Which, like any phase, is only defined up to mod(2π).

direction of this element, we find an expression for the Berry curvature integrated over the outer surface S of the closed sphere, which resembles the integral over the Gaussian curvature in Equation (1.2):

$$\oint_S \boldsymbol{B}(\boldsymbol{R}) \cdot d\,\boldsymbol{S} = 2\pi n. \tag{1.7}$$

1.1.2 Topology of the integer quantum Hall phase

The integer quantum Hall effect was discovered by Klaus von Klitzing in 1980, which won him the Nobel Prize in Physics in 1985. It occurs in two dimensional electron gases in field effect transistors that are exposed to large magnetic fields at low temperatures, which leads to an integer quantization of their Hall conductivity with applied magnetic field

$$\sigma_{xy} = N\frac{e^2}{h}, \tag{1.8}$$

where N is an integer, e is the elementary charge and h the Planck quantum.

Surprisingly, this quantization is independent on any of the material parameters, such as electrode materials or disorder strength, but seems to be an intrinsic property of the system. In fact, it turns out that the integer quantum Hall effect was the first example of a topological band insulator, which undergoes topological phase transitions when changing the quantization constant N. To understand why the Hall conductivity is quantized, it is instructive to treat the quantum Hall system as a band insulator. The Hamiltonian of the non-interacting 2D electron gas in an electromagnetic field can be obtained by the canonical replacement of the momentum $\boldsymbol{p} \to \boldsymbol{p} + e\boldsymbol{A}$, where $\boldsymbol{A}$ is the vector potential, as

$$H = \frac{1}{2m}\left(-i\hbar\boldsymbol{\nabla} + e\boldsymbol{A}\right)^2 + U(x, y), \tag{1.9}$$

with $U(x, y) = U(x + a, y) = U(x, y + b)$ being the periodic on the 2D Bravais lattice with lattice constants a, b [9]. It turns out that Bloch's theorem cannot be

applied directly, since the lattice translation operator does not commute with the Hamiltonian. It is therefore necessary to define a *magnetic unit cell* that encloses a flux quantum, with enlarged lattice parameters c, d. Since the magnetic lattice translation operator does commute with the Hamiltonian, Bloch's theorem allows us to label the Bloch wavefunction $u^\alpha_{\boldsymbol{k}}(x, y)$ and eigenvalues by a two dimensional momentum vector $\boldsymbol{k}$, which are periodic over the magnetic Brillouin zone. The full wavefunction of the Hamiltonian H is then $\psi^\alpha_{\boldsymbol{k}} = \exp(i\boldsymbol{k} \cdot \boldsymbol{r}) u^\alpha_{\boldsymbol{k}}(\boldsymbol{r})$, with $\boldsymbol{r} = (x, y)$. The integer quantum Hall system thus resembles the band structure of a crystal: there is a spectrum of energy eigenvalues $E^\alpha(\boldsymbol{k})$ that continuously disperse with $\boldsymbol{k}$ and forms bands that are labeled by the band index α and separated from each other by energy gaps. Thouless and coworkers used a formula from linear response theory to evaluate the current perpendicular to a small applied electric field [10]. They showed that the resulting Hall conductivity gives

$$\sigma_{xy} = \sum_\alpha \frac{e^2}{i2\pi h} \int_{BZ} d\boldsymbol{k} [\underbrace{\boldsymbol{\nabla}_{\boldsymbol{k}} \times \langle \boldsymbol{u}^{\boldsymbol{\alpha}}_{\boldsymbol{k}} | \boldsymbol{\nabla}_{\boldsymbol{k}} | \boldsymbol{u}^{\boldsymbol{\alpha}}_{\boldsymbol{k}} \rangle}_{= \boldsymbol{B}^\alpha(\boldsymbol{k})}]_3, \tag{1.10}$$

where the sum is over the fully occupied bands (assuming that the Fermi level lies in a band gap), the integration is over the full magnetic Brillouin zone, and the bracket $[\ldots]_3$ denotes the third component of a vector. Note that a two dimensional Brillouin zone has the topology of a torus, since the points with $\boldsymbol{k} = (k_1, 2\pi/d)$ and $\boldsymbol{k} = (k_1, 0)$ are equivalent, as well as the points $\boldsymbol{k} = (2\pi/c, k_2)$ and $\boldsymbol{k} = (0, k_2)$, with $0 \leq k_1 \leq 2\pi/c$ and $0 \leq k_2 \leq 2\pi/d$. The integral is therefore equivalent to the integral of the Berry curvature over a closed surface, which is quantized as was shown in Equation (1.7), with the topological invariant n known as the Chern number. It turns out that a nonzero Chern number corresponds to point-zeros (more precisely: vortices of the phase) of the Bloch wavefunction in the Brillouin zone, which is independent of the particular potential [9]. In other words, a nonzero Chern number is an obstruction to a smoothly defined phase over the entire torus of the Brillouin zone [13]. The fact

that the sum in Equation (1.10) includes the number of occupied bands indicates that the Hall conductivity, which is proportional to the total Chern number N, can only change if the number of occupied bands changes, which means that the band gap needs to close. This shows the robustness of the topological classification of band insulators against perturbations that do not close a band gap.

An important consequence of the topological classification of the integer quantum Hall state is the existence of metallic edge modes at the interface to a medium of different topological classification. Imagine, for instance, an interface between a quantum Hall state with total Chern number $N = 1$ and a trivial insulator with $N = 0$, which is shown in Figure 1.2(a). An example for such a trivial phase is the vacuum, which can also be considered as an insulator with a band gap for electron-positron pair production [1]. Since at the interface between the two insulators the topological classification is changing, the band gap of the magnetic band structure needs to close (as shown in Figure 1.2(b)), and the resulting metallic states are spatially pinned to the interface where the topological phase transition happens.

1.2 Topological invariants in time-reversal invariant insulators

The extension of topological band theory to time-reversal invariant band insulators was inspired by the *modern theory of polarization*, which links the polarization in dielectrics to the Berry phase of the Bloch wavefunctions [11]. The following description of topological band theory in time-reversal invariant insulators is taken from a review by Ando [12], which is based on the seminal works of Fu and Kane [13, 14]. It will be instructive to start with a two-band model in a single spatial dimension, and later generalize to higher dimensions and multiple bands. Finally, we want to discuss the consequences of the topological classification for electronic states at the edge or surface where a topological phase transition occurs.

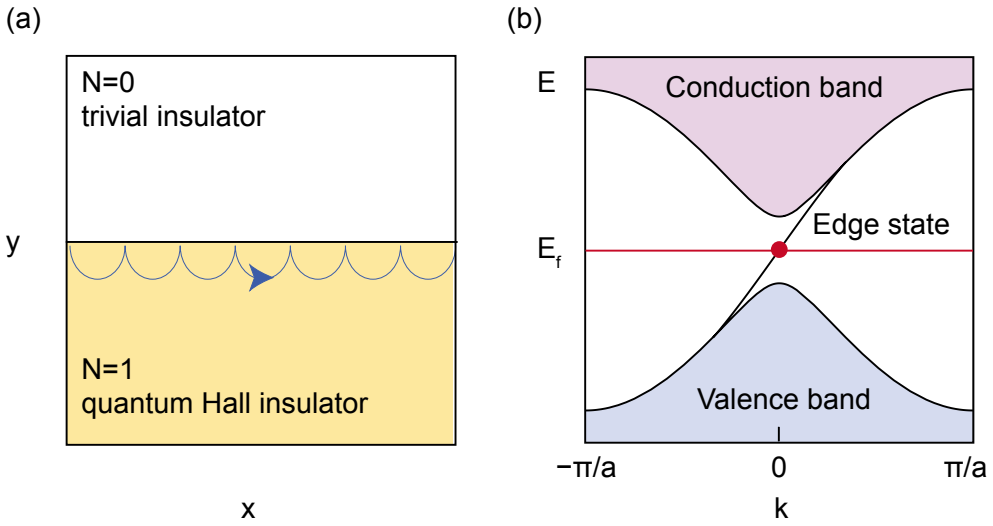


Figure 1.2: **Topological phase transition and resulting edge states at the interface of the integer quantum Hall state.** (a) Illustration of the interface between the topologically nontrivial quantum Hall insulator and a trivial insulator in real space coordinates x, y. The blue curve shows an edge state that is pinned to the interface. (b) Schematic energy momentum dispersion of the integer quantum Hall system, indicating a metallic edge state. Figure adapted from Ref [1].

1.2.1 Two band model of a single Kramers pair for 1D and 2D crystals

For time-reversal invariant fermionic insulators, for every Bloch state at $|u^{\alpha}_{\boldsymbol{k}}\rangle$ there is another state $|u^{\beta}_{-\boldsymbol{k}}\rangle$ with the same energy eigenvalue, and these two states are called *Kramers pairs*. In other words, the energy eigenvalues of a time-reversal invariant fermionic Hamiltonian are at least doubly degenerate. This follows because for fermionic particles (i.e. particles with half-integer spin), the time-reversal operator Θ has the property $\Theta^2 = -1$. To see that this leads to an at least twofold degeneracy, assume that there was a singly degenerate energy eigenvalue with eigenstate $|u^{\alpha}_{\boldsymbol{k}}\rangle$. Due to time-reversal symmetry (i.e. the time-reversal operator commutes with the Hamiltonian), this eigenstate of the Hamiltonian will also be an eigenstate of the time-reversal operator, i.e. $\Theta|u^{\alpha}_{\boldsymbol{k}}\rangle = c|u^{\alpha}_{\boldsymbol{k}}\rangle$, where c is a complex scalar. Thus $\Theta^2|u^{\alpha}_{\boldsymbol{k}}\rangle = |c|^2|u^{\alpha}_{\boldsymbol{k}}\rangle$, which contradicts the postulated property $\Theta^2 = -1$, because $|c|^2 \neq -1$. Thus every eigenvalue must be at least doubly degenerate, which in the

absence of spin-orbit coupling corresponds to the spin-degeneracy [4].

We will now consider a two band system with a single Kramers pair of Bloch states $|u_k^1\rangle, |u_k^2\rangle$ in a 1D chain with lattice constant $a = 1$, which is described by a Hamiltonian $\mathcal{H}$ with lattice periodic potential. The charge polarization P_ρ can be expressed as as an integral of the Berry connection over the full Brillouin zone:

$$P_\rho = \frac{1}{2\pi} \int_{-\pi}^{\pi} dk (A_1(k) + A_2(k)) = P_1 + P_2, \tag{1.11}$$

$$A_i(k) = -i\langle u_k^i | \nabla_k | u_k^i \rangle, \tag{1.12}$$

where P_1, P_2 are the contribution from each inidividual Kramers partner, which are called *partial polarizations*. Fu and Kane [13] defined a new type of polarization, which they called *time-reversal polarization*, as

$$P_\theta = P_1 - P_2, \tag{1.13}$$

which can be understood at the difference between charge polarization of the Kramers partners. Now let us assume that we start changing the Hamiltonian at time $t = 0$ adiabatically in a way that it returns back to its original state after a period T. Time reversal symmetry requires that the Bloch Hamiltonian $H(t) = \exp(i\boldsymbol{k} \cdot \boldsymbol{r})\mathcal{H}(t)\exp(-i\boldsymbol{k} \cdot \boldsymbol{r})$ transforms as $H(-t) = \Theta H(t)\Theta^{-1}$, where Θ is the time-reversal operator described above. As a consequence of the cyclic tuning of the Hamiltonian and the time-reversal invariance, at the time points $t = 0$ and $t = T/2$, the two bands become doubly degenerate for all values of $\boldsymbol{k}$, or in other words, the eigenstates of each Kramers pair are related via the time-reversal operator

$$\Theta|u_k^2\rangle = \exp(-i\chi(k))|u_{-k}^1\rangle \tag{1.14}$$

$$\Theta|u_k^1\rangle = -\exp(-i\chi(-k))|u_{-k}^2\rangle. \tag{1.15}$$

With these results we can now construct a unitary matrix

$$w_{\alpha\beta}(\boldsymbol{k}) = \langle u^{\alpha}_{-\boldsymbol{k}} | \Theta | u^{\beta}_{\boldsymbol{k}} \rangle, \tag{1.16}$$

which becomes antisymmetric (due to the orthogonality of the Bloch wavefunctions) at the time reversal invariant points $t = 0$ and $t = T/2$:

$$w(k) = \begin{pmatrix} 0 & \exp(-i\chi(k)) \\ -\exp(-i\chi(k)) & 0 \end{pmatrix}. \tag{1.17}$$

Using this matrix, one can show (see Ref [12]) that the time-reversal polarization takes the form

$$P_\theta = \frac{1}{i\pi} \log \left(\frac{\sqrt{w_{12}(0)^2}}{w_{12}(0)} \frac{w_{12}(\pi)}{\sqrt{w_{12}(\pi)^2}} \right). \tag{1.18}$$

The argument of the logarithm function log can take the values ± 1, which gives out either 0 or $i\pi + i2\pi h$, with h being an integer. The time-reversal polarization thus takes on values of 0 or 1 (mod 2). It is now interesting to see how P_θ develops in time between the points $t = 0$ and $t = T/2$, at which we obtained the analytical expression of equation (1.18). It turns out that there are only two possible scenarios that define the different topological classes for the Hilbert space of the Bloch wave functions that are mapped from the parameter space (k, t), which takes the form of a Torus (since $k + 2\pi$ and k are the same points, and so are $t + T$ and t). Either P_θ retains the same value at $t = 0$ and $t = T/2$, meaning that $\nu = P_\theta(T/2) - P_\theta(0) = 0$, or it changes its value, thus $\nu = P_\theta(T/2) - P_\theta(0) = 1$ (mod 2). The quantity v is called a topological $\mathbb{Z}_2$ invariant. It is now possible to identify the parameter space (k, t) with the 2D Brillouin zone of a crystal, spanned by (k_1, k_2), where the four time-reversal invariant points Γ_i are mapped as shown in Figure 1.3(a). By computing $w_{12}(k)$ for all Γ_i, the

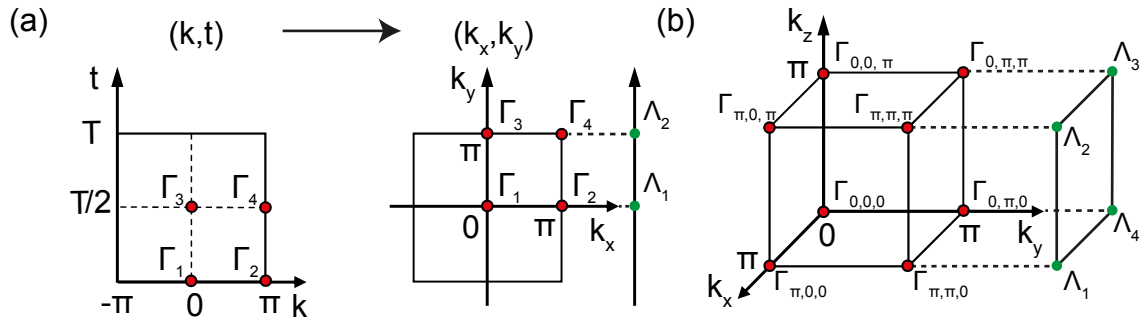


Figure 1.3: **Projections of time-reversal invariant points in the 1D, 2D and 3D Brillouin zone.** (a) Mapping of the time reversal invariant points Γ_i (red dots) from the variable pair (k, t) to the 2D Brillouin zone (k_x, k_y). Additionally the pairwise projection of the bulk time-reversal invariant moments (TRIMs) to the edge TRIMs Λ_i (green dots) is shown. (b) Positions of the bulk TRIMs in the 3D Brillouin zone (red dots), as well as their pairwise projection to the surface TRIMs (green dots). Figure adapted from Ref. [12].

$\mathbb{Z}_2$ invariant can be directly obtained from

$$(-1)^{\nu} = \prod_{i=1}^{4} \frac{w_{12}(\Gamma_i)}{\sqrt{w_{12}(\Gamma_i)^2}}. \tag{1.19}$$

Insulators that are characterized by a topological invariant $v = 1$ are called *topological insulators*, while insulators with $v = 0$ are called trivial insulators.

1.2.2 Extension to multiple Kramers pairs and 3D crystals with and without inversion symmetry

Now let us consider a time-reversal invariant system with $2N$ occupied bands forming N Kramers pairs. As before, we can relate the Kramers pairs with pair index $n \in [1, 2, \ldots, N]$ as

$$\Theta|u_k^{2n}\rangle = \exp(-\chi_n(k))|u_{-k}^{2n-1}\rangle \tag{1.20}$$

$$\Theta|u_k^{2n-1}\rangle = -\exp(-\chi_n(-k))|u_{-k}^{2n}\rangle. \tag{1.21}$$

We can now construct the matrix $w_{\alpha\beta}(k)$ defined in Equation 1.16, which at time reversal invariant points becomes an antisymmetric $2N \times 2N$ dimensional general-

ization of the matrix shown in Equation 1.17. The time-reversal polarization now includes a sum of the Berry connection integral of all the occupied Bloch bands over the whole Brillouin zone, which can be expressed for the 1D scenario via the $w_{\alpha\beta}(k)$ matrix as

$$P_\theta = \frac{1}{i\pi} \log \left(\frac{\sqrt{\det(w(0))}}{\mathrm{Pf}(w(0))} \frac{\mathrm{Pf}(w(\pi))}{\sqrt{\det(w(\pi))}} \right). \tag{1.22}$$

The change in polarization between the time reversal invariant time points can again be classified as before via the $\mathbb{Z}_2$ invariant ν as

$$(-1)^\nu = \prod_{i=1}^{4} \underbrace{\frac{\mathrm{Pf}(w(\Gamma_i))}{\sqrt{\det(w(\Gamma_i))}}}_{:=\delta(\Gamma_i)}. \tag{1.23}$$

Here, the Pfaffian $\mathrm{Pf}(w(\Gamma_i))$ of the antisymmetric matrix $w(\Gamma_i)$ gives $\mathrm{Pf}(w(\Gamma_i)) = w_{12}(\Gamma_i) \cdot w_{34}(\Gamma_i) \cdot \ldots \cdot w_{2N-1,2N}(\Gamma_i) = \exp(-i \sum_{n=1}^{N} \chi_n(\Gamma_i))$. It is related to the determinant of $w(\Gamma_i)$ by $\mathrm{Pf}(w(\Gamma_i))^2 = \det(w(\Gamma_i))$.

When generalizing the theory presented above to 3D crystals, it turns out that there are four $\mathbb{Z}_2$ invariants that describe the change of time-reversal polarization between the eight time-reversal invariant moments that exist in any 3D Brillouin zone [1]. The first index is usually called the strong index ν_0, and is related to the product of the quantities $\delta(\Gamma_i)$ at all eight time-reversal moments (TRIMs) Γ_i shown in Figure 1.3 (2) as

$$(-1)^{\nu_0} = \prod_{i=1}^{8} \delta(\Gamma_i). \tag{1.24}$$

The remaining three indices (v_1, v_2, v_3) are defined by the product of four $\delta(\Gamma_i)$'s at TRIMs Γ_i that are lying in the same plane, but do not include $\Gamma_i = 0$. They can be computed via

$$(-1)^{\nu_1} = \delta(\Gamma_{\pi,0,0})\delta(\Gamma_{\pi,\pi,0})\delta(\Gamma_{\pi,0,\pi})\delta(\Gamma_{\pi,\pi,\pi}) \tag{1.25}$$

$$(-1)^{\nu_2} = \delta(\Gamma_{0,\pi,0})\delta(\Gamma_{\pi,\pi,0})\delta(\Gamma_{0,\pi,\pi})\delta(\Gamma_{\pi,\pi,\pi}) \tag{1.26}$$

$$(-1)^{\nu_3} = \delta(\Gamma_{0,0,\pi})\delta(\Gamma_{0,\pi,\pi})\delta(\Gamma_{\pi,0,\pi})\delta(\Gamma_{\pi,\pi,\pi}). \tag{1.27}$$

Note that a gauge transformation may change the sign of the individual factors $\delta(\Gamma_i)$, but will leave the product of the above formulas invariant [13]. Three dimensional insulators with $v_0 = 1$ are called *strong* topological insulators for reasons that will be discussed later, while insulators with $v_0 = 0$ but at least one of (v_1, v_2, v_3) nonzero are called *weak* topological insulators. Insulators where all indices are zero are called *trivial* insulators. It is customary to write the topological index as $(v_0; v_1, v_2, v_3)$.

We now want to consider a system that has inversion symmetry, which means that the Hamiltonian commutes with the inversion operator, and we can thus choose our Bloch wavefunction basis such that they are eigenfunctions of the inversion operator and Hamiltonian. Fu and Kane [14] showed that under this condition, the factors $\delta(\Gamma_i)$ can be directly computed from the inversion (also called *parity*) eigenvalues $\xi^{\alpha}(\Gamma_i)$ of all occupied states at the TRIMs via

$$\delta(\Gamma_i) = \prod_{n=1}^{N} \xi^{2n}(\Gamma_i). \tag{1.28}$$

Parity eigenvalues can be obtained from the results of density functional theory (DFT) band structure calculations, which can be used to make plausible predictions for the topological classification of solids.

1.2.3 Edge and surface states at the interface of topological insulators

One of the most interesting properties of topological insulators (TIs) is the existence of metallic edge or surface states on the interface to a topologically trivial medium. Similar to the case of the integer quantum Hall state, these states must exist at the interface since the bandgap needs to close to allow for a change of the topological invariant. What is special about the edge states of topological insulators is that they are spin-polarized and protected from elastic backscattering off non-magnetic impurities. In the following we will discuss the relationship between the the surface

electronic structure of TIs and their topological invariants discussed above.

We can see from Figure 1.3 that two bulk TRIMs Γ_a, Γ_b are projected pairwise on the edge or surface TRIMs Λ_i. This allows us to define a surface time-reversal polarization

$$\pi(\Lambda_i) = \delta(\Gamma_a)\delta(\Gamma_b). \tag{1.29}$$

This definition now allows us to classify the surface state dispersion between any two surface TRIMs Λ_a, Λ_b, which is illustrated in Figure 1.4. Generically, any surface state present needs to be twofold Kramers degenerate at the TRIMs, and pertubations such as spin-orbit coupling will lift the degeneracy between TRIMs. If the surface time-reversal polarization is the same between the surface TRIMs $\pi(\Lambda_a) = \pi(\Lambda_b)$, then this means that the surface states will connect pairwise between Λ_a, Λ_b (shown in Figure 1.4(a)), which means that the surface states will cross the Fermi level an even number of times between Λ_a, Λ_b, and pertubations may move any metallic edge states above or below the Fermi energy. However, if the surface time-reversal polarization is changing between surface TRIMs, i.e. $\pi(\Lambda_a) \neq \pi(\Lambda_b)$, this means that the surface states will connect in a zigzag pattern (see Figure 1.4(b)), or in other words, the Kramers paris "switch partners" between Λ_a, Λ_b [14], which leads to an odd number of crossings at the Fermi level. This kind of crossing is special, since perturbations may move the positions of the Kramers pairs energetically, but they cannot remove the metallic state at the Fermi level, which points to a topological origin. For the 2D case, the even or odd number of Fermi level crossings fully determines the topological classification, since this means that one of the factors $\delta(\Gamma_i)$ in Equation (1.23) is different from the three others. For the 3D case, the situation is slightly more complicated. In case of a nonzero strong index $v_0 = 1$, the product of the polarizations gives $\pi(\Lambda_1)\pi(\Lambda_2)\pi(\Lambda_3)\pi(\Lambda_4) = -1$, which means that a single one of the four $\pi(\Lambda_i)$ differs from the others. As a result, there will be an odd number of *Dirac point* band crossings in the Brillouin zone, which are located at the TRIMs and lead to a quasi-linear dispersion relation in their vicinity. For $\nu_0 = 0$, this means

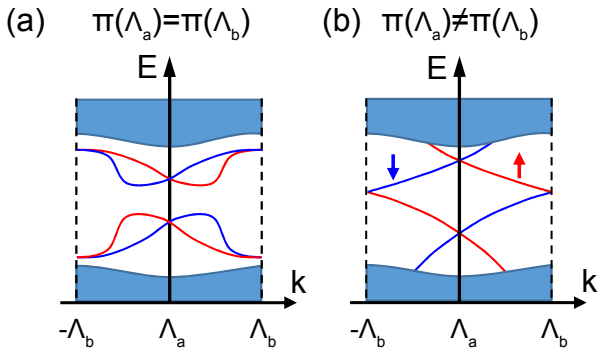


Figure 1.4: **Edge state band structure as a hallmark of a change in the time-reversal polarization.** (a) The surface time-reversal polarization *is not* changing between the surface TRIM's Λ_a, Λ_b, thus the surface states will connect the Kramers degeneracies at Λ_a, Λ_b in a pairwise pattern. As a result, the surface states can be removed from the Fermi level between Λ_a, Λ_b by shifting the positions of the Kramers degeneracies via pertubations. The red and blue bands indicate the Kramers partners. (b) The surface time-reversal polarization *is* changing between the surface TRIM's Λ_a, Λ_b, thus the surface states will connect the Kramers degeneracies at Λ_a, Λ_b in a zigzag pattern. As a result, metallic surface states will persists in the presence of any pertubations that are not breaking time-reversal symmetry. Figure adapted from Ref. [12].

that $\pi(\Lambda_1)\pi(\Lambda_2)\pi(\Lambda_3)\pi(\Lambda_4) = +1$, so either all factors are the same (which leads to an even crossing between all Λ_i) or they are pairwise different, which leads to an even number of *Dirac points* in the BZ.

There is another important property of the interface bands forming a zigzag crossing: States with opposite spin polarization are counterpropergating (see Fig 1.4(b)), which is why they have been called *helical* edge or surface states due to the link between spin and momentum. Interestingly, electrons that are encircling helical Dirac points in 3D will acquire a Berry phase of π, which is predicted to lead to *antilocalization* [1] , and can be measured by spin-resolved angle-resolved photoemission [15]. The spin-polarization of the edge states leads to another surprising consequence: elastic backscattering at non-magnetic impurities is suppressed, which leads to ballistic transport at zero temperature [1]. The protection from backscattering can be understood by considering the two possible scattering paths for elastic backscattering scattering on the edge. A right moving electron can either take a clockwise or

a counterclockwise turn around an impurity to scatter into a left moving mode with opposite spin. The two scatterings paths will therefore differ by a spin-rotation of 2π, which leads to destructive interference between them [16].

References

[1] M Zahid Hasan and Charles L Kane. Colloquium: topological insulators. *Reviews of Modern Physics*, **82**(4):3045, 2010.

[2] Philip Warren Anderson. *Basic notions of condensed matter physics*. Benjamin-Cummings, 1984.

[3] Mikio Nakahara. *Geometry, topology and physics*. CRC Press, 2003.

[4] Charles L Kane. Topological Band Theory and the Z2 Invariant. In Marcel Franz and Laurens Molenkamp, editors, *Topological Insulators*, **6** of *Contemporary Concepts of Condensed Matter Science*, pages 3 – 34. Elsevier, 2013.

[5] Elsa Abbena, Simon Salamon, and Alfred Gray. *Modern differential geometry of curves and surfaces with Mathematica*. CRC press, 2006.

[6] David J Griffiths. *Introduction to quantum mechanics*. Cambridge University Press, 2016.

[7] J.J. Sakurai and J. Napolitano. *Modern Quantum Mechanics*. Addison-Wesley, 2011.

[8] D. J. Richardson, A. I. Kilvington, K. Green, and S. K. Lamoreaux. Demonstration of Berry's Phase Using Stored Ultracold Neutrons. *Physical Review Letters*, **61**:2030–2033, Oct 1988.

[9] Mahito Kohmoto. Topological invariant and the quantization of the Hall conductance. *Annals of Physics*, **160**(2):343–354, 1985.

[10] DJ Thouless, Mahito Kohmoto, MP Nightingale, and M Den Nijs. Quantized Hall conductance in a two-dimensional periodic potential. *Physical Review Letters*, **49**(6):405, 1982.

[11] Raffaele Resta and David Vanderbilt. *Theory of polarization: a modern approach*, pages 31–68. Springer, 2007.

[12] Yoichi Ando. Topological insulator materials. *Journal of the Physical Society of Japan*, **82**(10):102001, 2013.

[13] Liang Fu and Charles L Kane. Time reversal polarization and a Z2 adiabatic spin pump. *Physical Review B*, **74**(19):195312, 2006.

[14] Liang Fu and Charles L Kane. Topological insulators with inversion symmetry. *Physical Review B*, **76**(4):045302, 2007.

[15] D. Hsieh, Y. Xia, L. Wray, D. Qian, A. Pal, J. H. Dil, J. Osterwalder, F. Meier, G. Bihlmayer, C. L. Kane, Y. S. Hor, R. J. Cava, and M. Z. Hasan. Observation of Unconventional Quantum Spin Textures in Topological Insulators. *Science*, **323**(5916):919–922, 2009.

[16] Xiao-Liang Qi and Shou-Cheng Zhang. Topological insulators and superconductors. *Reviews of Modern Physics*, **83**(4):1057, 2011.

[17] Karin Everschor-Sitte and Matthias Sitte. Real-space Berry phases: Skyrmion soccer. *Journal of Applied Physics*, **115**(17):172602, 2014.

Chapter 2

Introduction to angle-resolved photoelectron spectroscopy (ARPES)

Angle-resolved photoelectron spectroscopy (ARPES) is an important tool to directly probe the electronic structure of solids. In this chapter we will give an introduction into the theoretical background of this technique, as well as the instrumentation that is used for ARPES experiments.

2.1 Theory of photoemission

Since the discovery of photoemission by Hertz in 1887 [18], and its relation to the quantization of light by Einstein in 1905 [34], a large body of literature has evolved that details its theoretical description. Here, we will only review the most relevant principles of this technique that are necessary to understand the subsequent chapters, and refer the interested reader for more information to the books by Hüfner [19] and Kevan [20], as well as the reviews by Braun [21] and Damascelli [22].

The photoemission process can be understood in the context of time-dependent perturbation theory in which an interaction Hamiltonian H_{int} is perturbing the electronic system of the solid, which leads to an excitation of the initial N-electron

many-body eigenstates $|\Psi_i^N\rangle$ of the unperturbed Hamiltonian H_0 into a many-body excited state $|\Psi_f^N\rangle$. This many-body state includes a photoelectron, which exits the solid if its kinetic energy exceeds the sample work function ϕ_s of the solid, and the remaining $N-1$ electron many-body system that is left behind. The photoemission intensity I can then be related to the sum of all possible transitions that are connecting initial and final states $I = \sum_{i,f} w_{f,i}$, where the transition rates can be obtained from Fermi's golden rule as [19]

$$w_{f,i} = |\langle \Psi_f^N | H_{int} | \Psi_i^N \rangle|^2 \times \delta(E_f^N - E_i^N - h\nu), \tag{2.1}$$

where the terms describing energy conservation in the delta function are the energy of the initial state E_i^N and final state E_f^N, as well as the energy of the photon $h\nu$. A commonly employed approximation to evaluate the above expression is to neglect interactions between the photoelectron and the remaining $N-1$ electron system, which is called the *sudden approximation* [19, 23]. This means that the final N particle wavefunction can be written as the antisymmetrized product $\Psi_f^N = C[\phi_f(k)\Psi_f^{N-1}]$, where $\phi_f(k)$ is the single-particle wavefunction of the excited photoelectron, Ψ_f^{N-1} the $N-1$ many-body wavefunction of the remaining system (which is generally not an eigenfunction of the bare Hamiltonian H_0, but rather a superposition of eigenfunctions Ψ_m^{N-1}), and C is the antisymmetrization operator. If we can similarly decompose the initial state into the single-particle wavefunction of the photoelectron before excitation and the remaining $N-1$ electron wavefunction $\Psi_i^N = C[\phi_i(k)\Psi_i^{N-1}]$, then we can separate the matrix element of the photoelectron excitation and the excitation of the remaining $N-1$ many-body system, which gives us the following expression for the photoemission intensity

$$I(\boldsymbol{k}, E_{kin}) \propto \sum_{f,i} \underbrace{|\langle \phi_f(k) | H_{int} | \phi_i(k) \rangle|^2}_{:=|M_{i,f}(k)|^2} \sum_m \underbrace{|\langle \Psi_m^{N-1} | \Psi_i^{N-1} \rangle|^2}_{:=|c_m|^2} \times \delta(E_m^{N-1} - E_{kin} - E_i^N - h\nu), \tag{2.2}$$

where E_m^{N-1} is the energy of Ψ_m^{N-1}(a $N-1$ eigenstate of the Hamiltonian H_0), E_{kin} is the kinetic energy of the excited photoelectron, $M_{i,f}(k)$ is the matrix element describing the light-matter interaction between the photon and photoelectron, and c_m is the matrix element describing the many-body interactions of the photohole that was created as a result of the photoelectron excitation. The second sum in the above equation is called the *spectral function* $A(k,E)$ which can be related via a Green's function formalism to the complex self-energy $\sum = \sum' + i\sum''$ via

$$A(\boldsymbol{k},E) = \sum_m |c_m|^2 = \frac{1}{\pi}\frac{\sum''}{(E-\epsilon(\boldsymbol{k})-\sum')^2+\sum''^2}, \tag{2.3}$$

where $\epsilon(\boldsymbol{k})$ is some bare band energy that is typically obtained from *density functional theory* calculations. For so called *weakly interacting systems*, where self-energy effects can be neglected, the spectral function becomes simply $A(\boldsymbol{k}) = \frac{1}{\pi}\delta(E-\epsilon(\boldsymbol{k}))$, in which case the ARPES intensity is sampling the momentum resolved dispersion of the bare bands, thus leading to an intensity distribution as shown in Figure 2.1(a,i). For so called *strongly interacting systems*, it is necessary to take into account additional corrections due to self-energy effects. The self energy can be obtained by simple analytical Fermi-liquid models (see e.g. Ref. [24]) or more sophisticated numerical methods (see e.g. Ref. [25]). The real part of the self energy leads to bare band shifts, and the imaginary parts leads to band broadening. Additionally, the self-energy can also involve an *incoherent* part that leads to satellite lines at higher binding energies (see Figure 2.1(a,ii) and e.g. Ref. [26]), which are caused by low-energy excitations, such as electron-hole pairs [19]. ARPES can therefore directly quantify many-body effects in strongly interacting systems. However, for the interpretation of the ARPES data from materials discussed in this thesis, it seems to be sufficient to neglect self-energy corrections.

Besides the contribution from the spectral function, we have seen from equation 2.2 that the photoemission intensity is also modulated by the matrix elements $M_{i,f}(k)$,

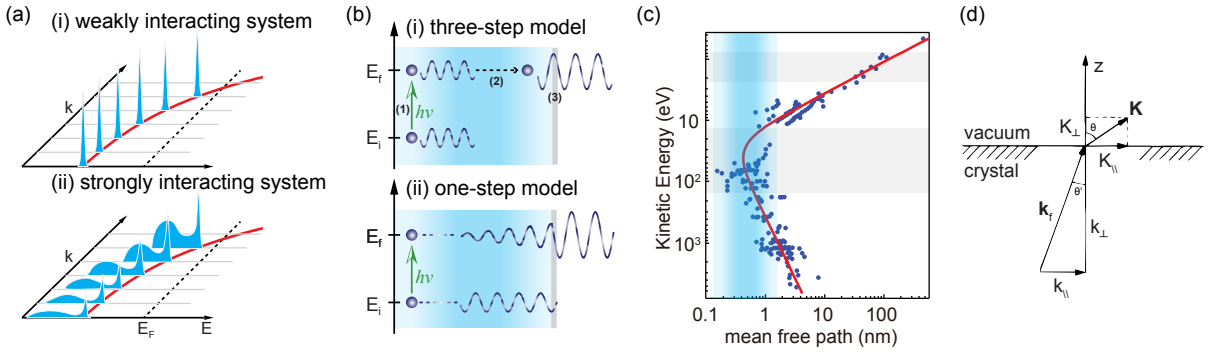


Figure 2.1: **Characteristics of the photoemission process.** (a, i-ii) Measured spectral function for a weakly and strongly interacting system, respectively, shown as blue solid area. Solid red line indicates the bare band structure. (b) Illustration of the three-step and the one-step model of photoemission. (c) Universal curve of the inelastic mean free path of an electron. (d) Relation between measured momentum of the photoelectron outside the solid with wave vector $\mathbf{K}$, and its momentum quantum number $\boldsymbol{k}_f$ in the final state within the solid. Figures (a-c) courtesy of Haifeng Yang, Figure (d) adapted from Ref. [19].

as. There are two approaches to computing them. In the popular *three step model*, the photoemission process is divided into three parts (see Figure 2.1(b,i))

1. In the first step, the photoelectron is excited from a the single particle state $|\phi_i(k)\rangle$ to a final single-particle excited state $|\phi_f(k)\rangle$ that is localized inside the crystal.

2. Subsequently, the electron is transported to the surface. The transport coefficient is related to the inelastic mean free path of the excited electron in the solid, which is photon energy dependent, and can be modelled by the so called universal curve (which is approximately material independent). It is shown in Figure 2.1(c).

3. Finally, the electrons escape from the sample surface into the vacuum. However, only electrons that have a kinetic energy component normal to the surface that is sufficient to overcome the surface potential barrier can escape into the vacuum. For the same reason, the electron momentum normal to the surface is not conserved, while the momentum parallel to the surface remains conserved.

As a result, the components of the final state electron momentum inside of the solid $\boldsymbol{k}_f$ is related to the photoelectron momentum outside of the solid $\boldsymbol{K}$ as follows (also see Figure 2.1(d)):

$$\boldsymbol{k}_{f||} = \boldsymbol{K}_{||} = \sin(\theta)|\boldsymbol{K}| = \sin(\theta)\sqrt{2mE_{kin}/\hbar^2}, \tag{2.4}$$

where $E_{kin} = h\nu - E_b - \phi_s$ is the kinetic energy of the photoelectron, $h\nu$ is the photon energy, E_b is the binding energy of the electron, ϕ_s is the work function if a sample, and θ is emission angle with respect to the surface normal. The perpendicular moment $\boldsymbol{k}_{f\perp}$ can often be approximated with the so called *free electron* final state approximation, where one assumes that the final state energy in the crystal is given by $E = E_{kin} + V_0 = \hbar^2(\boldsymbol{k}_{f||} + \boldsymbol{k}_{f\perp})^2/2m = \hbar^2(\boldsymbol{k}_{f||}^2 + \boldsymbol{k}_{f\perp}^2)/2m$, is the so called *inner potential* that needs to be overcome at the surface. The perpendicular momentum is then given as

$$\boldsymbol{k}_{f\perp} = \sqrt{2m(E_{kin} + V_0)/\hbar^2 - \sin^2(\theta)2mE_{kin}/\hbar^2} = \sqrt{2m([h\nu - E_b - \phi_s]\cos^2(\theta) + V_0)/\hbar^2}. \tag{2.5}$$

The inner potential can be obtained directly from calculations, by comparing the experimental data with band structure calculations, or self-consistently by comparing the obtained periodicity of the band structure along $\boldsymbol{k}_\perp$ with the expected periodicity of the Brillouin zone.

To calculate the amplitude of the matrix element $M_{i,f}(k) = \langle\phi_f(k)|H_{int}|\phi_i(k)\rangle$, one needs to make an approximation for the interaction Hamiltonian. The standard textbook approximation is to use the classical transformation of the Hamiltonian that we have encountered previously $\boldsymbol{p} \to \boldsymbol{p} + e\boldsymbol{A}$, where $\boldsymbol{A}$ is the vector potential of the electromagnetic field. If one further neglects two photon processes and the discontinuity of the vector potential at the surface when applying the dipole approximation (i.e. assuming that the light wavelength is large compared to atomic distances, and thus

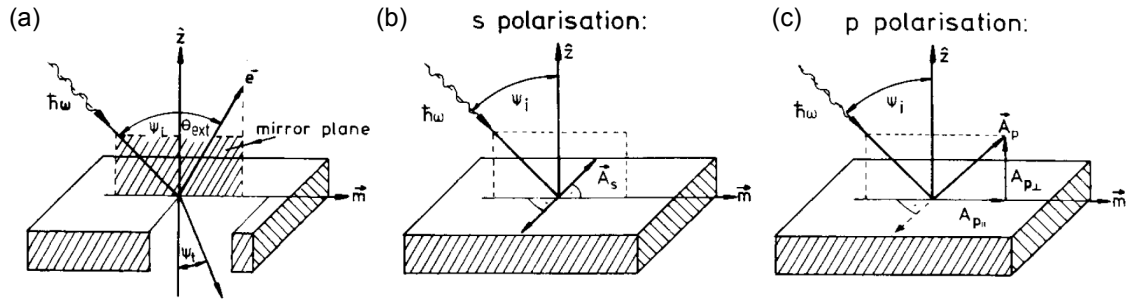


Figure 2.2: **Selection rules and parity of the dipole operator.** (a) Illustration of the alignment between incoming light and outgoing electron in a mirror plane of the sample. (b-c) Illustration of the direction of the dipole operator A for s-polarization and p-polarization. Figure taken from Ref [19].

$\boldsymbol{A} = \boldsymbol{A}_0$ is constant), one arrives at an approximation for the matrix element [19]:

$$M_{i,f}(k) = \langle \phi_f(k) | \boldsymbol{A}_0 \cdot \boldsymbol{r} | \phi_i(k) \rangle. \tag{2.6}$$

From this expression it is possible to gain a qualitative understanding of the selection rules of the photoemission process. Let us consider a scenario where the incoming light, the outgoing electron and detector are aligned along a mirror plane, as shown in Figure 2.2(a). In that case, we can assume that the parity eigenvalue of the final state with respect to the mirror plane is even [19, 22], which means that both the dipole operator$\boldsymbol{A}_0 \cdot \boldsymbol{r}$ and the initial state $|\phi_i(k)\rangle$ need to have the same parity such that the overall matrix element has even parity for a nonzero amplitude (otherwise the terms in the spatial integration will cancel). As a result, one can selectively excite orbitals with different symmetries with respect to the mirror plane by using linear polarized light with either s-polarization (dipole operator is perpendicular to the mirror plane, and thus has odd parity with respect to it, as shown in Figure 2.2(b)) and p-polarization (which has even parity with respect to mirror plane, shown in Figure 2.2(c)). Furthermore, the matrix elements are also photon energy dependent due to a varying photoionization crosssections [22].

Although the above approximations are usually sufficient for a qualitative analysis,

the classical transformation $\boldsymbol{p} \rightarrow \boldsymbol{p} + e\boldsymbol{A}$ to construct the interaction Hamiltonian neglects relativistic effects that can lead to spin-flipping of the electron spin as a result of the light radiation [29], which are relevant for the quantitative analysis of spin-resolved photoemission spectroscopy [27, 28]. More realistic quantitative calculations of the matrix elements can be obtained within so called *one-step* model calculations, that can include spin, energy and wave-vector dependence, as well as detailed multiple electron scattering [21]. The final states in this model are not simple Bloch states, but so called time-reversed low-energy electron diffraction (LEED) states that are damped on the inside of the crystal to simulate the limited escape depth, and are extended into the vacuum, as shown in Figure 2.1(b,ii).

In addition to the spectral-function and matrix-element contributions, the photoemission intensity is also affected by the occupation of states (electrons can only be emitted from occupied states) which can be modelled by including a Fermi function factor $I(E,T) \propto (\exp(E/k_BT)+1)^{-1}$, where k_B is the Boltzmann constant and T is the sample temperature. Furthermore, the measured photoemission intensity distribution is also affected by the instrument resolution and extrinsic background signals due to inelastically scattered electrons (called secondary electrons). There are models to describe these contributions, which were not relevant for the present thesis, but can be found elsewhere [22].

2.2 Synchrotron-based ARPES instrumentation

All of the data presented in this thesis was taken at ARPES endstations at synchrotron light sources. In the following we will therefore present the generic elements of a synchrotron based ARPES set-up. More details about the specific parameters of the individual set-ups will be given where relevant in the subsequent chapters. Most of the data presented in this thesis was collected at beamline I05 at the Diamond Light Source (DLS), UK, and the interested reader can find more details about this

beamline in Ref. [30]. Additional data was also taken at the beamline APE, which is detailed in Ref. [31].

2.2.1 Synchrotron light source

The unique feature of a synchrotron based ARPES set-up is its powerful and tunable light source. In contrast to other light sources used for ARPES, such as noble gas discharge lamps or laser sources, electron synchrotrons can deliver bright light beams ($\sim 10^{12}$ photons/s) over a large photon energy range. This is particularly important for the study of samples with a three-dimensional dispersion relation, since the perpendicular component of the probed electron momentum depends on the available photon energy (as we saw from Equation 2.5). Furthermore, changing the photon energy can tune the photoionization crosssection for certain bands and allows us to focus on the features of interest. In order to generate this very bright photon beam, electrons are accelerated to very high energies (e.g. 3 GeV at DLS), and then circulate in storage rings with perimeters between hundreds to thousands of meters [32]. The most important source of light in modern synchrotrons are so called *undulators*, which consists of a periodic array of magnets that create a sinusoidal magnetic field with wavelength λ_0 along the path of the electron. As a result of the electron motion in the ultra-relativistic limit ($\beta = v/c \approx 1$, $\gamma = (1 - v^2/c^2)^{-1/2} \gg 1$, with electron velocity v), light is radiated along the axis of the electron beam in a small angle $\tan\theta = 1/\beta\gamma$ with wavelength $\lambda \propto \lambda_0$ [32]. Thus, by changing the distance between the magnets that define λ_0, the light wavelength can be tuned to produce very bright light over a continuous wavelength range. Furthermore, by further tuning the magnetic field and path of the electron in the undulator, both linearly polarized as well as circularly polarized light can be produced. The light can then be monochromatized with a grating and focused on the sample via mirrors.

2.2.2 Ultra-high vacuum equipment

As we have seen during the discussion of the three-step model, the inelastic mean free path of electrons is relatively short, of the order of below$\approx$ 1 nm for typical kinetic energies $\approx$ 100 eV, which means that any adlayers on the sample surface will block the photoelectrons emitted from the sample. As a result, the sample surface needs to be prepared such that it is very clean (e.g. via crystal cleaving, annealing, or *in-situ* deposition), and the experiment needs to be conducted in ultra-high vacuum (UHV, technically starting below 10^{-9} mbar, but for ARPES typically in the order of $\approx 10^{-10} - 10^{-11}$ mbar) to avoid a contamination of the sample surface during the duration of the experiment. To maintain such extreme low pressures, single-crystal samples are typically grown $ex-situ$ and inserted into stainless steel vacuum chambers that are connected to the main *analysis* chamber via multiple stages of differential pumping. To achieve such low pressures, a hierarchical combination of different pumping systems is employed that operate at decreasing base pressures. A typical combination involves the following elements [33]: a roughing pump, such as a scroll pump (reaching down to 10^{-3} mbar), is backing a turbomolecular pump, which can already reach very low pressures down to 10^{-11} mbar by pushing residual gas atoms out of the chamber via fast moving rotor blades. To maintain the UHV pressure, one can use an ion pump that is ionizing the residual gas via a plasma discharge, as well as reactive titanium ions that react with the rest gas and get deposited into the walls of the pump. After opening a UHV chamber to ambient conditions, it is usually necessary to heat up the system for a few days to remove water and other impurities from the chamber walls. The vacuum quality can be inspected via pressure gauges and residual gas analyzers, which are a type of mass-spectrometer. To shield the chamber interior from the external magnetic fields that would deflect the photoemitted electrons, an additional mu-metal shielding is usually used.

Besides the chambers and pumping system, another important element is the

sample stage and sample manipulator, which define the measurement geometry of the incoming beam, the sample and the electron analyzer. Modern sample manipulators have up to six degrees of freedom, which makes it possible to spatially scan the beamspot over the sample, and also align the sample and electron analyzer slit along an arbitrary angle. Liquid Helium cooling and thermal shielding of the sample stage on the manipulator can further achieve sample temperatures below $T = 10$ K, which reduces the effects of thermal band broadening and makes it possible to observe electronic phase transitions that happen at low temperatures.

2.2.3 Electron analyzer

For static ARPES experiments, the state-of-the art electron energy analyzer used in many ARPES set-ups around the world is the hemispherical deflection analyzer. Since all measurements in this thesis were conducted using this device, we will only present this type of analyzer. It consists of three elements:

1. *Electron lens*: After the electrons are ejected out of the sample, they pass through a hole into a metal tube that contains the electron lensing system. The electron lenses have two functions: they image the angular spread of the electrons from the sample onto the exit slit of the electron lens, and they retard the electrons, which allows measurements of their kinetic energy with higher resolution.

2. *Hemispheres*: The dispersive element of the analyzer are two hemispherical cups, that function like a bend capacitor. They map the incoming electrons that are passing through the slit on to a two-dimensional plane, one axis being their angular distribution and the other being the energy distribution.

3. *Electron detector*: After passing through the imaging and dispersive elements, the electrons enter multichannel plates (MCPs), which have the function of multiplying the incoming electron current. Subsequently, the electrons hit a phos-

phor screen where the electron current is transformed into a photon flux, which is then detected by a CCD camera. Thus, in a single image, the hemispherical analyzer can simultaneously measure the angular spread of the electrons along the slit as well as their kinetic energy distribution.

References

[18] Heinrich Hertz. Ueber einen Einfluss des ultravioletten Lichtes auf die electrische Entladung. *Annalen der Physik*, **267**(8):983–1000, 1887.

[19] Stefan Hüfner. *Photoelectron spectroscopy: principles and applications*. Springer, 2003.

[20] Stephen Douglas Kevan, editor. *Angle-resolved photoemission: theory and current applications*, **74**. Elsevier, 1992.

[21] J Braun. The theory of angle-resolved ultraviolet photoemission and its applications to ordered materials. *Reports on Progress in Physics*, **59**(10):1267, 1996.

[22] Andrea Damascelli. Probing the electronic structure of complex systems by ARPES. *Physica Scripta*, **2004**(T109):61, 2004.

[23] J.J. Sakurai and J. Napolitano. *Modern Quantum Mechanics*. Addison-Wesley, 2011.

[24] H. Iwasawa, Y. Yoshida, I. Hase, K. Shimada, H. Namatame, M. Taniguchi, and Y. Aiura. High-Energy Anomaly in the Band Dispersion of the Ruthenate Superconductor. *Physical Review Letters*, **109**:066404, Aug 2012.

[25] Antoine Georges, Gabriel Kotliar, Werner Krauth, and Marcelo J. Rozenberg. Dynamical mean-field theory of strongly corre-

lated fermion systems and the limit of infinite dimensions. *Review of Modern Physics*, **68**:13–125, Jan 1996.

[26] Matthew D. Watson, Steffen Backes, Amir A. Haghighirad, Moritz Hoesch, Timur K. Kim, Amalia I. Coldea, and Roser Valentí. Formation of Hubbard-like bands as a fingerprint of strong electron-electron interactions in FeSe. *Physical Review B*, **95**:081106, Feb 2017.

[27] Chris Jozwiak, Cheol-Hwan Park, Kenneth Gotlieb, Choongyu Hwang, Dung-Hai Lee, Steven G Louie, Jonathan D Denlinger, Costel R Rotundu, Robert J Birgeneau, Zahid Hussain, et al. Photoelectron spin-flipping and texture manipulation in a topological insulator. *Nature Physics*, **9**(5):293–298, 2013.

[28] Cheol-Hwan Park and Steven G Louie. Spin polarization of photoelectrons from topological insulators. *Physical Review Letters*, **109**(9):097601, 2012.

[29] Peter D Johnson. Spin-polarized photoemission. *Reports on Progress in Physics*, **60**(11):1217, 1997.

[30] M. Hoesch, T. K. Kim, P. Dudin, H. Wang, S. Scott, P. Harris, S. Patel, M. Matthews, D. Hawkins, S. G. Alcock, T. Richter, J. J. Mudd, M. Basham, L. Pratt, P. Leicester, E. C. Longhi, A. Tamai, and F. Baumberger. A facility for the analysis of the electronic structures of solids and their surfaces by synchrotron radiation photoelectron spectroscopy. *Review of Scientific Instruments*, **88**(1):013106, 2017.

[31] G Panaccione, I Vobornik, J Fujii, D Krizmancic, E Annese, L Giovanelli, F Maccherozzi, F Salvador, A De Luisa, D Benedetti, et al. Advanced photoelectric effect experiment beamline at Elettra: A surface science laboratory coupled with Synchrotron Radiation. *Review of Scientific Instruments*, **80**(4):043105, 2009.

[32] Donald H Bilderback, Pascal Elleaume, and Edgar Weckert. Review of third and next generation synchrotron light sources. *Journal of Physics B: Atomic, molecular and optical physics*, **38**(9):S773, 2005.

[33] P. Hofmann. *Surface Physics: An Introduction*. Philip Hofmann (self-published), 2013.

[34] A. Einstein. Über einen die Erzeugung und Verwandlung des Lichtes betreffenden heuristischen Gesichtspunkt. *Annalen der Physik*, **322**(6):132–148, 1905.

Chapter 3

Discovery of a strong topological phase and large carrier density imbalance in the semimetal LaBi

After reviewing topological band theory and introducing angle-resolved photoelectron spectroscopy (ARPES), we will now turn to an ARPES study of the non-magnetic lanthanum monopnictide LaBi, which contains the first set of new findings covered in this thesis. Before presenting the details of this study, we will review previous experimental and theoretical reports about the non-magnetic rare-earth monopnictide family RX (R=Y, La; X = P, As, Sb, Bi), which will help the reader to put the new results into context. Most of the ARPES data presented here was collected and analyzed in joint collaboration between the author and Dr Juan Jiang, Advanced Light Source, Lawrence Berkeley National Lab, USA, and will be published in our joint publication in Ref. [67].

3.1 Previous experimental and theoretical studies of the lanthanum and yttrium monopnictides

Non-magnetic lanthanum monopnictes that are crystallizing in a simple rock-salt face-centered cubic structure were synthesized and studied since the 1930s [36, 35, 37, 38]. They became an interesting research subject in the 1980s [64, 63] as a reference material for other rare-earth monopnictides that showed heavy-fermion behaviour. Since then, they were studied less frequently, but recently regained attention due to their unusual magneto-transport properties. The starting point for the regained recent interest in this material family was a theoretical study by Zeng and coworkers [39], which predicted the existence of a strong topological phase in the material family LaX (X = P, As, Sb, Bi), based on a *density functional theory* band structure analysis that indicates a band inversion (i.e. energetic re-ordering of bands with opposite parity eigenvalues) between lanthanum d-orbitals and pnictogen p-orbitals at the X point of the Brillouin zone. This finding led to magneto-transport investigations, which revealed the existance of an extremely large magnetoresistance in these compounds, as well as band structure calculations and photoemission studies.

3.1.1 Magneto-transport studies of non-magnetic rare-earth monopnictides YSb, LaSb, and LaBi

Motivated by the unique magneto-transport properties of topological insulators [40], Tafti and coworkers studied the temperature dependence of the resistivity in LaSb in the presence of an external magnetic field [41]. They found that LaSb shows a metallic decrease of the resistivity with very low residual resistivity as small as 80 nΩcm in the absence of a magnetic field. However, in the presence of a magnetic field, the resistivity is at first decreasing with temperature until a minimum at $T = T_m$ (see Figure 3.1(a)), and then rising again upon further temperature decrease

until an inflection point $T = T_i$, after which the resistivity ρ_{xx} is saturating upon further temperature decrease [1]. The magnitude of this resistivity plateau at low temperatures scales quadratically with the applied field, which leads to a positive magnetoresistance $MR = \frac{\rho_{xx}(B)-\rho_{xx}(B=0)}{\rho_{xx}(B=0)} \approx 10^6$ % at magnetic fields of $B = 9$ T and $T = 5$ K, and shows no sign of saturation up to $B = 40$ T [50]. Such an *extremely large magnetoresistance* (XMR) was before only observed in the topological Dirac semimetal Cd_3As_2 [51], Weyl semimetals TaAs, NbP, and NbAs [52, 54, 53], and semimetals $NbSb_2$, $PtSn_4$, and WTe_2 [55, 56, 57]. Although other semimetals such as Graphite or Bismuth also show a large increase of resistance with the application of magnetic fields, their resistivity saturates at moderate to high fields (below ≈ 12 T for graphite and ≈ 35 T for Bismuth [68, 69]), which ultimately limits the absolute value of their magnetoresistance. XMR materials are therefore characterized by a very large *and* unsaturated magnetoresistance at high fields. Soon thereafter, the XMR and resistivity plateau was also found in LaBi [44, 43, 42] and YSb [46, 45] (see Figure 3.1(a-c)). A possible metal-insulator transition was excluded based on a comparison of activation energies between LaSb and LaBi, as well as an analysis of the electronic specific heat, which points to a strong field-induced scattering mechanism as the origin of the resistivity upturn [44].

3.1.2 Band structure calculations and possible mechanisms for the extremely large magnetoresistance

The origin of these unusual magneto-transport properties in the lanthanum and yttrium monopnictides is still under debate, and it also remains unclear whether there is a single mechanism for the field-induced scattering in all of the previously mentioned compounds, or whether the same phenomenon is driven by different mechanisms in different systems. In the following, three possible mechanisms that are discussed in

[1] Note that here we consider the transverse magnetoresistance, meaning that the magnetic field direction is perpendicular to the current flow direction in the absence of the magnetic field.

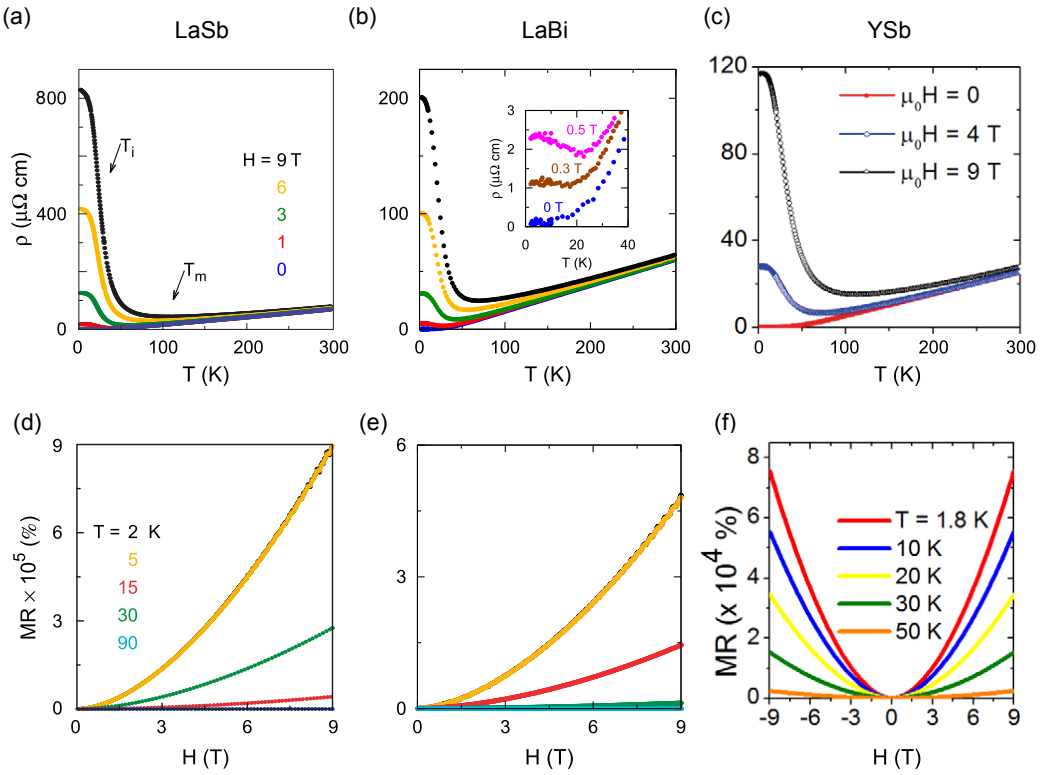


Figure 3.1: **Magneto-transport studies on LaSb, LaBi, and YSb.** (a-c) Temperature dependence of the resistivity ρ in the presence of a magnetic field for LaSb, LaBi, and YSb, respectively. T_m indicates the temperature at the resistivity minimum, and T_i the infliction temperature below which the resistivity starts to saturate. (d-e) Extremely large magnetoresistance (XMR) for various temperatures in LaSb, LaBi, and YSb, respectively. Figures adapted from Refs. [41, 44, 46].

the literature will be presented, which are relevant for the subsequent discussion of our ARPES measurements.

The majority of published literature on LaSb and LaBi suggests that the XMR effect is driven by an almost perfect compensation of electron and hole carriers. This scenario is primarily supported by ab-initio calculations [43, 42, 47], which predict that LaSb and LaBi are semimetals with two hole pockets centered at the Γ-point of the Brillouin zone, and three electron pockets, which are centered at the X-points of the Brillouin zone (see Figure 3.2(a-c)). The shapes of the pockets are predicted to be spherical for the inner hole pocket, octahedral for the outer hole pocket, and elliptical for the electron pockets, with the long axis of the ellipse pointing along the Γ-X direction. The band inversion at the X point leads to an anticrossing between valence and conduction bands, which can be seen in Figure 3.2(d) along with the orbital character of the bands. All the calculations shown in Figure 3.2(b-d) were performed with the PBE functional within the generalized gradient approximation (GGA) [60] by the authors of the references given above. For comparison, using the same method [2], we computed the band structure for the cousin compound YSb (shown in 3.2(e)), which shows an additional small hole pocket at Γ and the absence of an anticrossing along Γ-X, which indicates the absence of a band inversion.

If one treats the charge transport in LaSb and LaBi within the semiclassical *two band model* approximation [48], which assumes that there are only two carrier types in the system (here: electrons and holes) with densities n_e, n_h and mobilities μ_e, μ_h, then the magnetoresistance takes the form

$$\frac{\rho_{xx}(B) - \rho_{xx}(B=0)}{\rho_{xx}(B=0)} = \frac{n_e n_h \mu_e \mu_h (\mu_e + \mu_h)^2 B^2}{(n_e\mu_e + n_h\mu_h)^2 + (n_e - n_h)^2(\mu_e\mu_h)^2 B^2} \xrightarrow{n_e = n_h} \mu_e \mu_h B^2, \tag{3.1}$$

[2] Calculations were performed with the software Wien2k with a full-potential linearized augmented plane-wave and local orbitals basis, using the Perdew–Burke–Ernzerhof parameterization of the Generalized Gradient approximation, including spin-orbit coupling. The $R_{MT}K_{Max}$ parameter was set to 7, experimental lattice constants were used, and the k-point mesh converged at 1000 k-points in the Brillouin zone. [62]

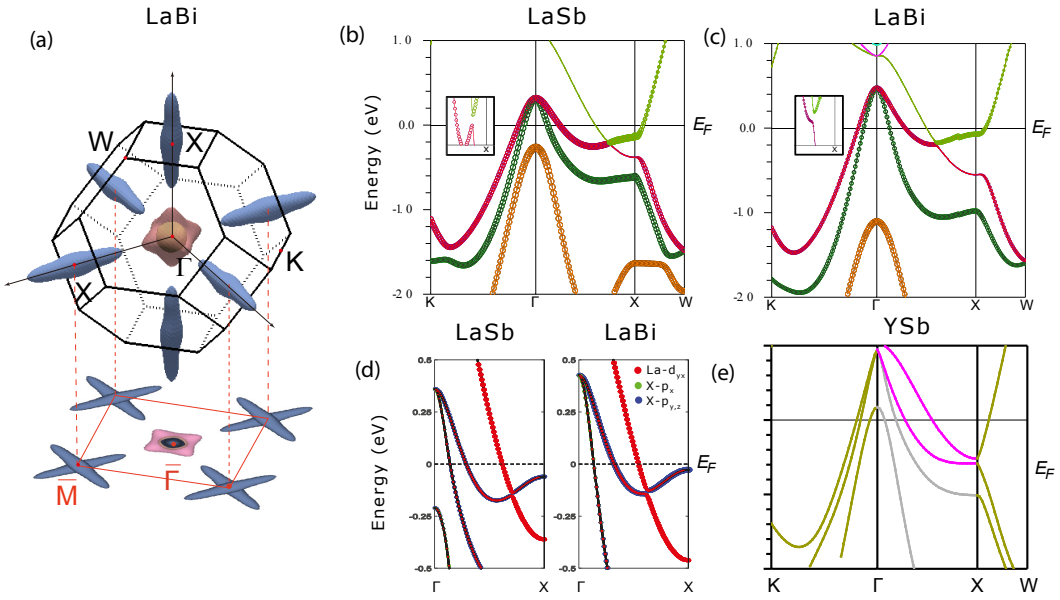


Figure 3.2: **Density functional theory calculations for LaSb, LaBi, and YSb.** (a) Fermi surface pockets in three-dimensional Brillouin zone on LaBi (top) and their projection on the (001) surface Brillouin zone (bottom). (b-c) Band structure along high-symmetry points for LaSb and LaBi, indicating a band inversion that leads to an anticrossing (highlighted in the insets) of valence and conduction band along Γ-X. (d) Orbital character of the electron pockets in LaSb and LaBi. (e) Band structure along high-symmetry points for YSb. Figure (a) courtesy of Xiang Xu. Calculations (b-d) adapted from Refs. [39, 44]. (d) Our own calculation with the same parameters as used in Ref [44].

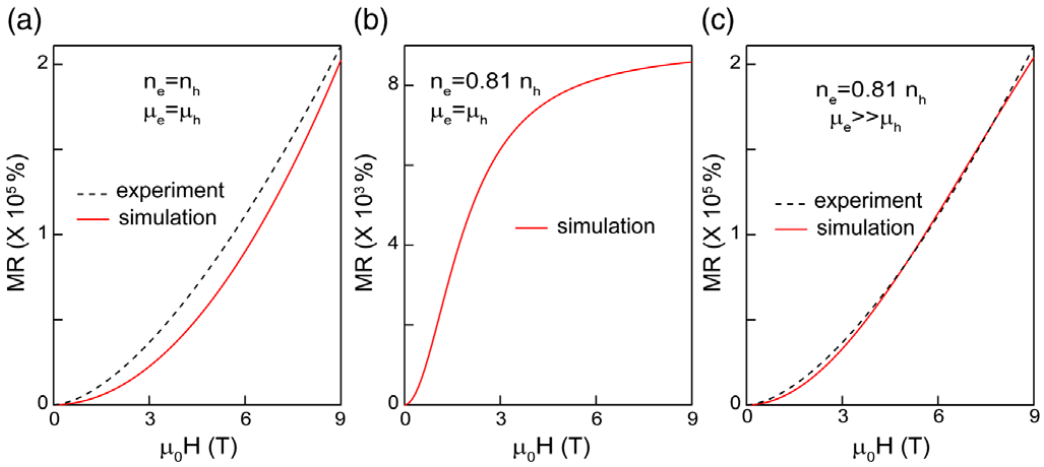


Figure 3.3: **Electron-hole mobility imbalance scenario suggested for YSb.** (a) Comparison of experimental MR with two-band model calculation for carrier compensation and mobility balance. (b) MR calculation for carrier imbalance and mobility balance. (c) Experimental MR and calculation for carrier imbalance and large mobility imbalance. Figure taken from Ref. [49].

which appears to be a good discription of the unsaturating quadratic field dependence of the MR in the rare-earth monopnictides.

However, as we will see later, perfect carrier compensation may indeed not always be fulfilled. Staying within the semi-classical paradigm, He and coworkers proposed a second mechanism for YSb, in which a small imbalance of the electron-hole density can be offset by an imbalance of the carrier mobilities (see Figure 3.3), which leads to a seemingly parabolic field dependence for low fields and a saturating magnetoresistance at high fields [49].

The third mechanism was proposed by Tafti and coworkers, who called the scenario of perfect carrier compensation as the driving mechanism of the XMR into question. Estimating the carrier compensation status from the sign change of the Hall coefficient with temperature, they noted that although LaBi seemed better compensated than LaSb, the XMR in LaBi was typically smaller than in LaSb. They also showed that there seemed to a be universal triangular phase diagram among the XMR materials LaSb, LaBi, $NbSb_2$, $PtSn_4$ and WTe_2 (see Figure 3.4), as well as a universal appearance of d-p orbital band mixing in *ab-initio* calculations of all of these

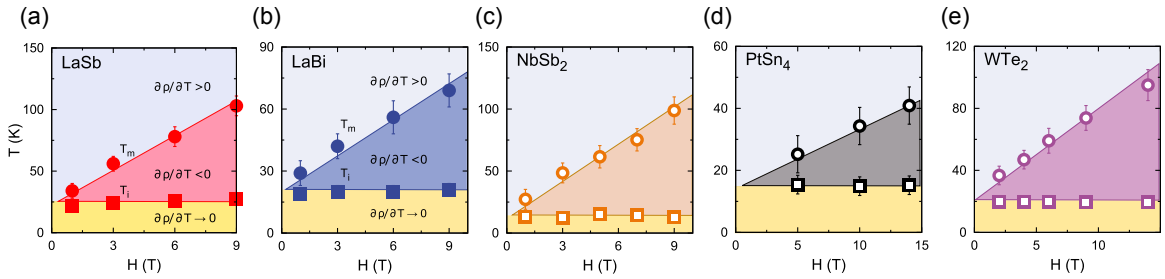


Figure 3.4: **Phase diagram of temperature T_m at resistivity minimum, and temperature T_i at resistivity infliction point for various XMR materials.** Three phases are highlighted: metallic behaviour $\partial\rho/\partial T > 0$, $\partial\rho/\partial T < 0$ insulating behaviour, and saturating behaviour $\partial\rho/\partial T \to 0$.

compounds (see Figure 3.2(d) for LaBi and LaSb). They further pointed out that the XMR single-band semimetals Cd_3As_2 and $Pb_{1-x}Sn_xSe$, which cannot be compensated, also show a large degree of orbital mixing. Based on the similarities between all these XMR materials, Tafti et al. hypothesized that the underlying mechanism of the small residual resistivity $\rho_{xx}(B = 0)$ could be a so far unknown topological mechanism that leads to a protection from backscattering in the bulk. This protection may then be broken by an external magnetic field, which interacts with a pseudospin that is generated by the orbital mixing, and results in the XMR due to substantial rise of backscattering [44]. It remains unclear, however, how this third mechanism can be related to the quadratic field dependence of the XMR.

3.1.3 ARPES studies and modified band-structure calculations of LaSb and YSb

The unusual magneto-transport properties of the nonmagnetic rare-earth pnictides motivated us and other groups to perform ARPES measurements on these compounds, which were all conducted at about the same time. At this point we will only discuss the results from other groups for YSb and LaSb, and leave the results on LaBi for the subsequent discussion of our own results. The objectives of these measurements were twofold: on the one hand it was interesting to confirm whether the predicted nontriv-

ial topology would lead to the appearance of topological surface states, which can be detected with ARPES. This is particularly intriguing because these compounds have no global band gap as the previous generation of TIs, but instead a local band gap at all k-points. One may therefore ask whether the coexistence of trivial bulk Fermi surface pockets would affect the topological classification. On the other hand, it was important to investigate the carrier compensation status by measuring the volume of the Fermi surface pockets, which is a critical ingredient for some of the proposed mechanisms of the XMR that were discussed above. The carrier concentration determination was particularly important, since angle-dependent quantum osciallation measurements - which are normally used to determine the volume of Fermi surface pockets - were mostly unable to detect frequency component from the outer hole pocket that was predicted by the *ab-initio* calculations [41, 44, 43, 42], although most recently there seems to have one successful angle-dependent measurement for LaSb [58].

The first angle-dependent quantum oscillation measurement by Tafti and coworkers indicated a frequency component that scaled with an angle dependence of $F(\theta) \propto 1/\cos(\theta - n\pi/2)$, which was interpreted as the signature of a surface state pocket. Such findings were initially supported by ARPES measurements that reported the existence of an anticrossing and surface state Dirac points along X-Γ-X [61] (see Figure 3.5(a-b)). However, subsequent soft X-ray ARPES measurements by Oinuma et al. [59], which have a better resolution along the k_z direction due to the longer electron penetration depth [70], showed that these cones are likely due to k_z-broadening and a superposition of the dispersion along X-Γ-X and W-X-W, which are both projected on the direction $\overline{M}$-$\overline{\Gamma}$-$\overline{M}$ in the (001) surface Brillouin zone (see Figures 3.2(a) and 3.5(c-g)). According to Oinuma et al., LaSb shows neither a band inversion nor topological surface states. This alternative finding was explained by pointing out that PBE-GGA calculations often underestimate band gaps, and that the band gap at the X-point can be better described by the mBJ functional, which removes the band inversion

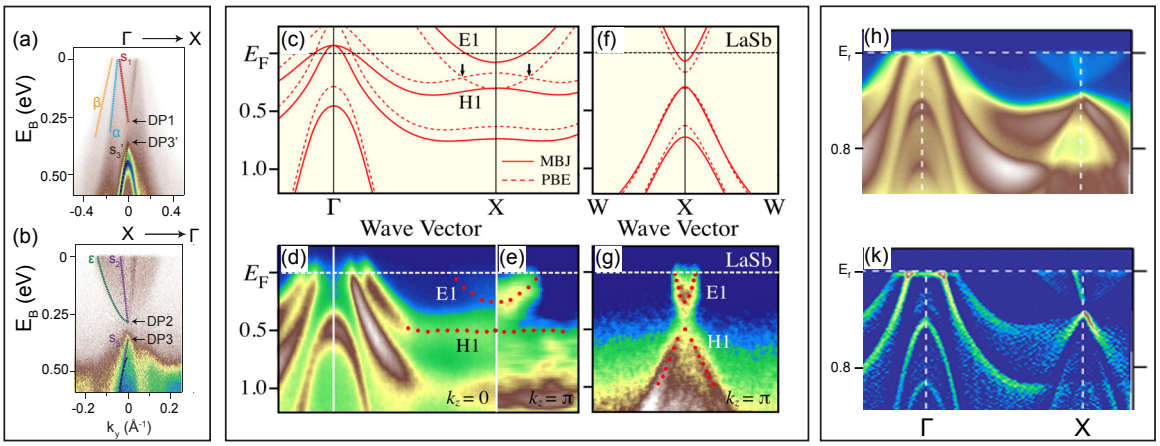


Figure 3.5: **ARPES measurements and ab-initio calculations for LaSb.** (a-b) VUV ARPES measurements at hv=22 eV, claiming the existance of multiple Dirac points (DP1,DP2,DP3) and surface states (s_1,s_2,s_3), adapted from Ref [61]. (c-g) Ab-initio calculations vs. soft X-ray ARPES data (hv=510 eV), adapted from Ref. [59]. (h-g) VUV ARPES measurements, and curvature plot, taken at hv=53 eV. Adapted from Ref. [50].

and anticrossing at X (see Figures 3.5(c-d)). Another high-resolution ARPES study by Zeng et al. [50] appears to agree with this interpretation (see 3.5(h-k)). However, also in the mBJ-based calculations, LaSb appears to be almost carrier compensated [50, 47], with elliptical electron pockets that can lead to an $F(\theta) \propto 1/\cos(\theta)$ angle dependence of their quantum oscillation frequency [58].

Similar to LaSb, ARPES studies of YSb by He et al. [49] have found that the band structure in this compound is also better described by calculations based on the mBJ functional, and that no band inversion or topological surface states are present. This is not surprising, given that the calculation based on the PBE-GGA functional in Figure 3.2(e) showed no band inversion. However, in contrast to LaSb, the ARPES measurements of the YSb found that its electron and hole pocket volumes are not perfectly compensated ($n_e \approx 0.81 n_h$). This finding led He et al. to the hypothesis of a large electron-hole mobility imbalance ($\mu_e = 9{\times}10^5$ and $\mu_h = 3.5{\times}10^3$ cm^2/Vs) that can offset the carrier imbalance, as was discussed in the previous section and shown in Figure 3.3. However, it remains unclear what may cause such a large carrier mobility imbalance in YSb. Very recently, a preprint of a quantum oscillation study

appeared that found YSb to be almost compensated, with $n_e \approx 0.94 n_h$ [71]. It is so far unclear what caused the deviation between the findings from these two methods, which will be further discussed in the final subsection below.

In summary we can conclude from the above discussion of the existing literature that the rare-earth monopnictides LaSb and YSb appear to be topologically trivial, which is indicated by the absence of a band inversion induced anticrossing and topological surface states. Consequently, the nontrivial topology is an unlikely origin of the XMR in these compounds, which may instead be caused by a combination of carrier density compensation or large carrier mobility difference.

3.2 Open research questions that are motivating the ARPES study of LaBi

After reviewing the literature on the rare-earth monopnictides, two open questions are presenting themselves:

1. **Is the topologically trivial nature of LaSb and YSb universal for all rare-earth monopnictides, or are there family members that are topologically nontrivial?** This question is important, since a nontrivial topology in combination with band-inversion induced orbital d-p mixing was proposed as a possible origin of the XMR in LaSb and LaBi, and may point to a so far unknown protection from backscattering *in the bulk* that leads to very large carrier mobilities. Furthermore, it is interesting to find a topologically nontrivial phase despite the absence of a global band gap, as was predicted by band structure calculations [39]. Moreover, given that the other rare-earth monopnictides LaSb and YSb appear to be trivial, a potentially nontrivial member LaBi would open the possibility to study a topological phase transition by elemental doping. Finally, one should recognize that the large family of rare-earth monopnictides hosts a plethora of exotic correlated phenomena [65]. Finding

a topological nontrivial phase in the lanthanum monpnictides would therefore give hope to realize more exotic topological phases in correlated systems, such as in the low carrier cerium monopnictides [66].

2. **Is the almost perfect carrier compensation in LaSb the main origin of the XMR in the lanthanum monopnictides, or are there family members that show the XMR in the absence of carrier compensation?** If there are compounds that deviate from perfect carrier compensation, can the XMR be explained by other mechanisms, such as an imbalance in carrier mobilities? This research question is interesting because there is currently no consensus about the mechanism of the XMR in the lanthanum monopnictides, although a majority of the published literature is advocating perfect carrier compensation as the main origin.

Both of these research questions can be answered by our ARPES study of LaBi, which will be discussed in the following sections.

3.3 Discovery of topological surface states in LaBi

LaBi is the compound with the heaviest elements among the lanthanum pnictide family. Since the band inversion in topological materials is often driven by spin-orbit coupling, which is typically stronger for compounds containing elements with high atomic number, it can be expected that LaBi should be the most likely candidate in the LaX family to show a topologically nontrivial phase.

LaBi crystallizes in a rocksalt fcc lattice with lattice constant $a = 6.58$ Å and two atom basis (one La and Bi atom each), which is shown in Figure 3.6(a). The elemental composition of the samples used for the subsequent ARPES measurement was confirmed via core level spectroscopy, which showed the characteristic lanthanum and bismuth peaks, as shown in Figure 3.6(b). To facilitate the search for topological surface states, our collaborators at the Max-Planck Institute for Chemical Physics of

Solids in Dresden, Germany, performed surface state calculations for the LaBi (001) surface based on the generalized gradient approximation (GGA)[3], which are shown in Figure 3.6(c). The surface state calculation predicts the existence of three Dirac points, two of which are located at the $\overline{M}$ point and one is located at the $\overline{\Gamma}$ point, which leads to a total of three Dirac points close to the Fermi level in the Brillouin zone, as is illustrated in Figure 3.6(d). Although perturbations may move the positions of the Dirac points above the Fermi level, there will always be an odd number of surface state crossings between $\overline{\Gamma}$-$\overline{M}$, and an even number of surface state crossings between $\overline{\Gamma}$-$\overline{X}$, as well as $\overline{X}$-$\overline{M}$. Thus the product of the time-reversal polarizations at the time-reversal invariant momenta must be $\pi(\overline{\Gamma})\pi(\overline{X})\pi(\overline{X})\pi(\overline{M}) = -1$ (see the discussion in the previous chapter), which corresponds to a strong topological phase. However, as we have seen from the discussion in the previous sections, the GGA approximation may underestimate the band gap at X, so any theoretical description requires experimental confirmation.

To give an overview of the experimentally determined ARPES data, and to compare our results with the ab-initio calculations, Figure 3.7 shows our ARPES data taken at the photon energy $hv = 126$ eV. This photon energy corresponds to the $k_z = \Gamma$ plane in the three dimensional Brillouin zone (BZ), as is illustrated in Figure 3.7(a). Note that there are two sets of high symmetry point that are equivalent in the bulk BZ, but nonequivalent when projected on the (001) surface: The X points are projected onto the Γ points (called $\overline{\Gamma}$ in the surface BZ), while the X* points are projected onto the W points (called $\overline{M}$ in the surface BZ). Figure 3.7(b) shows the resulting relationship between the high symmetry points in the $k_z = \Gamma$ plane in the bulk and the surface BZ. The measured equal energy surfaces for the $k_z = \Gamma$ plane are shown in Figures 3.7(c,1-3) and contrasted with bulk band structure cal-

[3]The calculations were performed with the Vienna *ab-initio* simulation package (VASP) using the generalized gradient approximation (GGA), including spin-orbit coupling as a perturbation. The surface state spectrum was obtained by projecting the density of states to four atomic layers of on the top of a half-infinite surface with the Green's function method based on tight-binding Wannier function parameters.

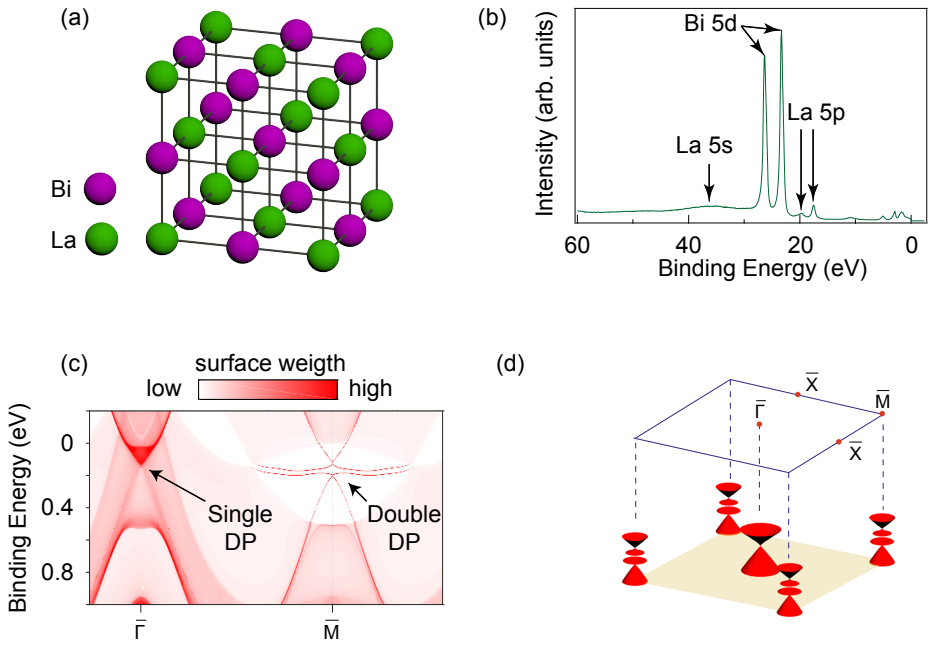


Figure 3.6: **Overview of LaBi's structural and surface electronic properties.** (a) Illustration of LaBi's crystal structure. (b) Measured core level spectrum of LaBi. (c) Surface state claculation for the [0 0 1] surface, courtesy of Shu-Chun Wu, Max-Planck Institute Dresden. (d) Illustration of surface Dirac cone positions in projected [0 0 1] surface Brillouin zone.

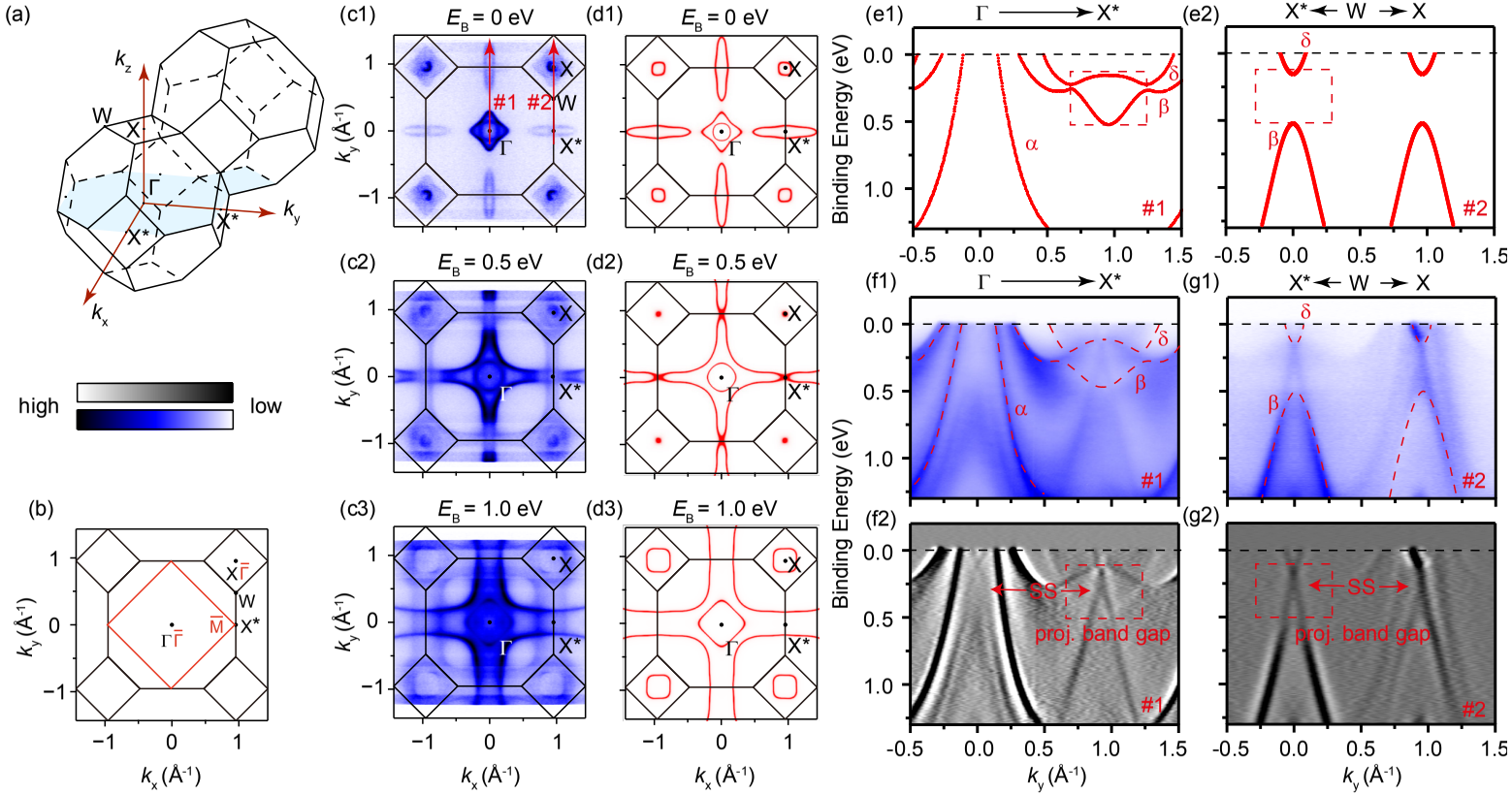


Figure 3.7: **Overview of ARPES measurements for $k_z = \Gamma$ plane.** (a) Illustration of the position of the $k_z = \Gamma$ plane in the 3D Brillouin zone (blue shaded plane). (b) Projection of the surface Brillouin zone and high symmetry points (red solid lines and letters) to the bulk $k_z = \Gamma$ plane boundaries. (c,1-3) Equal energy surface for binding energies $E_b = 0,\ 0.5,\ 1.0$ eV. (d,1-3) Corresponding calculations of the equal energy surfaces for the same binding energies. (e,1-2) Calculation of the bulk band dispersion along $X^* - \Gamma - X^*$ and $X^* - W - X$, which correspond to the high symmetry directions #1,#2 in (c1). The red dashed box indicates the position of a projected band gap at the $\overline{M}$ point of the surface BZ. (f-g) ARPES raw data and second derivative plot along the same high symmetry directions. The red label SS and red arrows indicate surface states in the projected band gaps. All data was taken at $hv = 126$ eV. Figures were drawn in joint collaboration with Juan Jiang, Advanced Light Source, Lawrence Berkeley National Lab, USA, and will be published in Ref. [67].

culations[4] in Figure 3.7(d,1-3), which show a qualitatively good agreement. Note, however, that the size of the elliptical electron pockets at X* appear to be smaller in the measurement than in the calculation. Furthermore, in addition to the strong bands from the $k_z = \Gamma$ plane, the ARPES measurements also show some weak bands that are projected from the $k_z = X$ plane (which will be further discussed in the next figure), which originates from the effect of k_z broadening due to the limited electron penetration depth in the vacuum ultra-violet (VUV) photon energy range (6 eV to approx. 120 eV) [70]. However, from the equal energy surfaces it is fairly easy to distinguish these two sets of bands. Figures 3.7(e,1-2) show the calculated dispersions along $X^* - \Gamma - X^*$ and $X^* - W - X$, which correspond to the high symmetry directions #1,#2 shown in Figure 3.7(c1). The labels α, β, δ, correspond to the bands that form the inner hole pocket, outer hole pocket, and electron pocket, respectively. The red dashed box indicates the approximate boundaries of a projected band gap, i.e. for all values of k_z, there are no bulk bands in this energy and k_y momentum range. Figures 3.7(f-g) show the raw ARPES data and second derivative data for the cuts along #1,#2 shown in Figure 3.7(c1), respectively. Dashed lines are a guide for the eye of the bulk band positions. The second derivative plots clearly show the existence of electronic states in the projected bulk band gap, which we will subsequently identify as surface states.

Before discussing the in-gap states, we also want to discuss the ARPES data for the $k_z = X$ plane, which is presented in Figure 3.8. Figure 3.8(a) shows the position of the $k_z = X$ plane in the 3D Brillouin zone, and Figure 3.7(b) the projections of high symmetry points to the surface BZ. The experimental equal energy surfaces in Figure 3.8(c,1-3) correspond qualitatively well with the calculations shown in Figure 3.8(d,1-3), but the elliptical electron pockets in the ARPES measurements are again smaller than predicted by the calculation. When comparing the calculated band

[4]Note that these bulk calculations were performed with the HSE06 hybrid functional implemented in VASP, instead of the bare GGA method that was used for the surface state calculation shown in Figure 3.6(c). All of the bulk band structure calculations that are discussed subsequently were calculated with the HSE06 method.

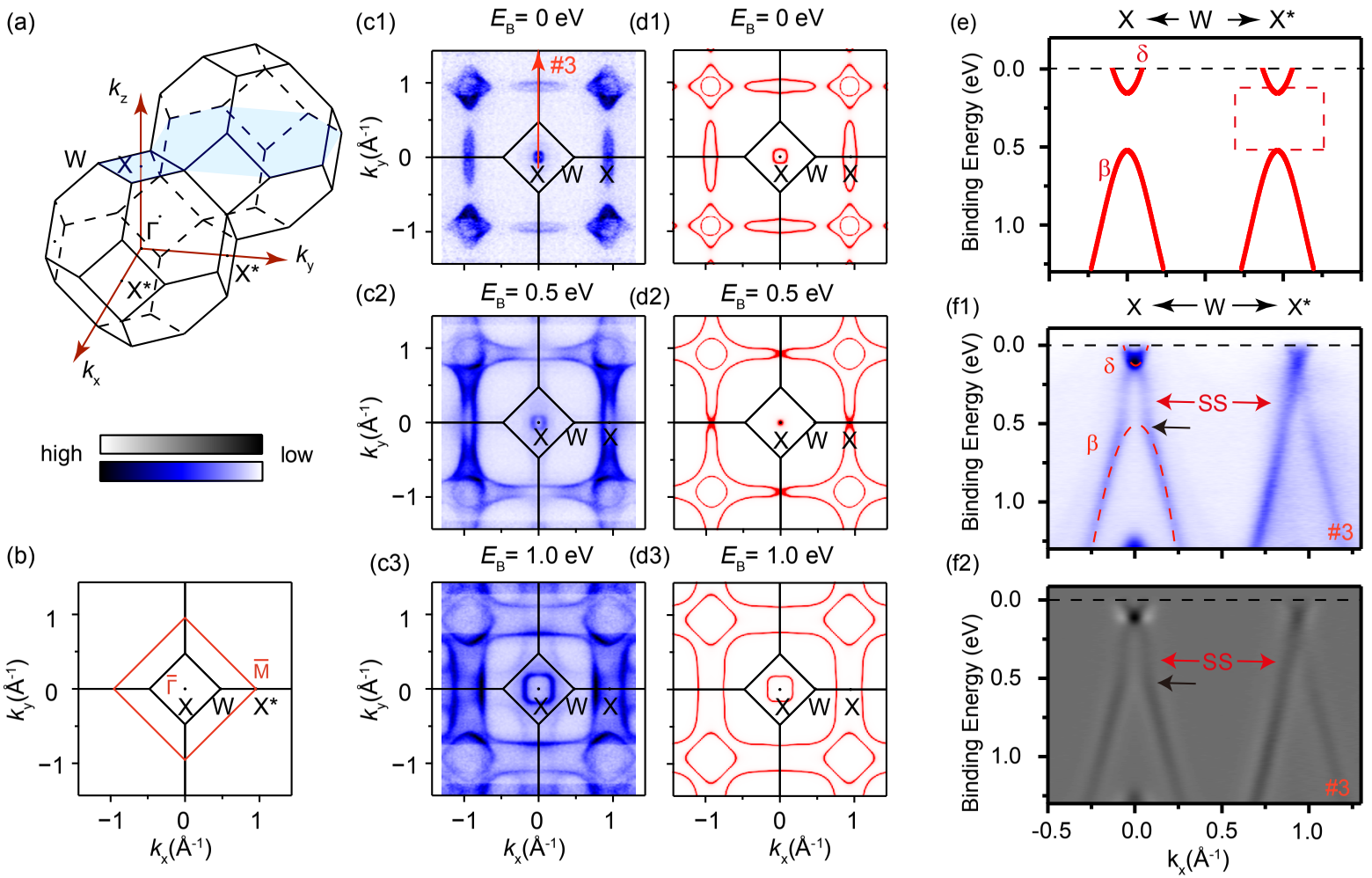


Figure 3.8: **Overview of ARPES measurements for $k_z = X$ plane.** (a) Illustration of the position of the $k_z = X$ plane in the 3D Brillouin zone (blue shaded plane). (b) Projection of the surface Brillouin zone and high symmetry points (red solid lines and letters) to the bulk $k_z = X$ plane boundaries. (c,1-3) Equal energy surface for binding energies $E_b = 0,\ 0.5,\ 1.0$ eV. (d,1-3) Corresponding calculations of the equal energy surfaces for the same binding energies. (e) Calculation of the bulk band dispersion along $X^* - W - X$, which corresponds to the high symmetry direction #3 (c1). The red dashed box indicates the position of a projected band gap at the $\overline{M}$ point of the surface BZ. (f,1-2) ARPES raw data and second derivative plot along the same high symmetry directions. The red label SS and red arrows indicate surface states in the projected band gaps. The black arrow indicates a discontinuity at the top of the valence band at X. All data was taken at $hv = 168$ eV. Figures were drawn in joint collaboration with Juan Jiang, Advanced Light Source, Lawrence Berkeley National Lab, USA, and will be published in Ref. [67].

dispersion in Figure 3.8(e) with the experimental dispersions in Figure 3.8(f,1-2), one can again identify an in-gap state in the projected band gap at X*. Additionally, there is a discontinuity in the dispersion at the top of the valence band β at $E_b \approx 0.5$ eV (indicated by a black arrow), which indicates that the band above is unlikely a result of k_z broadening (which should give a smoothly evolving projection of bands), but is instead of surface origin, which will be corroborated in the following discussion.

To further investigate the origin of the in-gap states, we conducted high resolution ARPES measurements at low photon energies (hv=54 eV), as well as photon energy dependent measurements, which are shown in Figure 3.9. To ease the identification of surface states in the experimental data, Figure 3.9(a1) shows the surface state calculation shown in Figure 3.6(c) at the $\overline{\Gamma}$ point with a re-scaled color map that suppresses the weak surface weight of the projected bulk bands and only leaves the strong surface weight of the surface states visible. Figure 3.9(a2-3) shows the corresponding high resolution ARPES measurement and second derivative plot, which show the existence of the surface state and Dirac point predicted by the calculation. Similarly, Figure 3.9(b1-3) show the existence of predicted double Dirac points in the projected band gap at the $\overline{M}$ point. For reference, we also show the Fermi surface pockets and equal energy surfaces of the three surface states in figures (c1-3).

Finally, we want to give evidence that the previously discussed states are nondispersive along the momentum direction direction perpendicular to the sample surface k_z, which is the hallmark their surface character. Figure 3.10(a1) shows the Fermi surface in the k_z vs. k_y plane, which is perpendicular to the (001) cleavage plane, and which was constructed by scanning the photon energy over a large range (hv=30-200 eV) and converting the result in the framework of the free electron final state approximation (inner potential V_0 =9 eV). This Fermi surface allows us to identify two sets of bands at the $\overline{M}$ and $\overline{\Gamma}$ points that are nondispersive along k_z, which correspond to the surface states identified in Figures 3.9(a,b). Note that one can recognize some blurred Fermi surface at around $k_z \approx 5.75$ Å close to $\overline{M}$ and $\overline{\Gamma}$, which corresponds

to the elliptical bulk electron pocket and two bulk hole pockets that we expect from the bulk calculation shown in 3.10(a2). The excellent correspondence between the Fermi surface pocket positions in the k_x vs. k_y plane and k_z vs. k_y plane, which is a consequence of the cubic crystal symmetry, shows that the free electron final state approximation allows us to accurately determine the k_z momentum. The green lines in Figure 3.9(a1) show the k_z positions of the cuts with photon energy hv =126 eV ($k_z = \Gamma$) and hv =168 eV ($k_z = X$) that were used for the mapping in the Figures 3.7 and 3.8. Additional evidence for the applicability of the free electron final state approximation is given in 3.10(b,1-2). Figure 3.10(b,1) shows the $X - \Gamma$ dispersion along the k_z direction for a cut with $k_y = 0$, which is in good agreement with the expected bulk calculation. The flat dispersion of the Dirac point cannot easily be resolved due to the overlapping bulk bands.

Before discussing the significance of our discovery of topological surface states in LaBi, we want to report our study of the carrier compensation status in the same compound. We further like to note that other groups also performed ARPES measurements on LaBi, which also concluded that LaBi is topologically nontrivial [61, 72, 73].

3.4 Discovery of large carrier density imbalance in LaBi

As we have learned from the first section of this chapter, the origin of the extremely large magnetoresistance in the lanthanum monopnictides is under debate, with a majority of reports proposing perfect electron/hole density compensation as the relevant mechanism. However, besides the parabolic field dependence of the observed magnetoresistance, which seems to suggest perfect carrier compensation within the two band model approximation (see Equation 3.1), there is no experimental evidence for this scenario. Angle-dependent quantum oscillation measurements - which can measure the area of the Fermi surface cross-section perpendicular to the applied magnetic

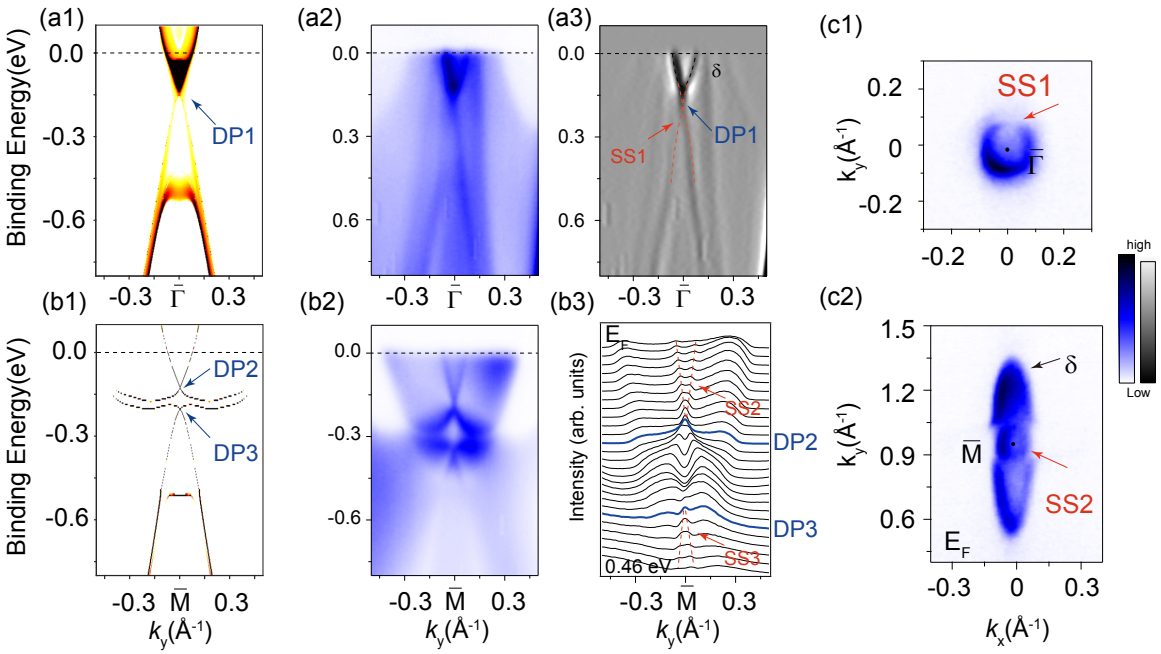


Figure 3.9: **Comparison of surface state calculation with high resolution ARPES data.** (a1-3) Surface state calculation (changed color scale compared to Figure 3.6(c)), raw ARPES data, and second derivative plot of the surface state (SS1) at $\overline{\Gamma}$. Blue arrow indicates the Dirac point (DP1) position. Photon energy used was $h\nu$ =54 eV. (b1-3) Surface state calculation, raw ARPES data, and momentum distribution curves of the surface states (SS1, SS2) at $\overline{M}$. Blue arrow indicates the Dirac point (DP2,DP3) positions. Photon energy used was $h\nu$ =54 eV. (c1-2) Fermi surface pockets of the surface states at $\overline{\Gamma}$ and $\overline{M}$. Figures were drawn in joint collaboration with Juan Jiang, Advanced Light Source, Lawrence Berkeley National Lab, USA, and will be published in Ref. [67].

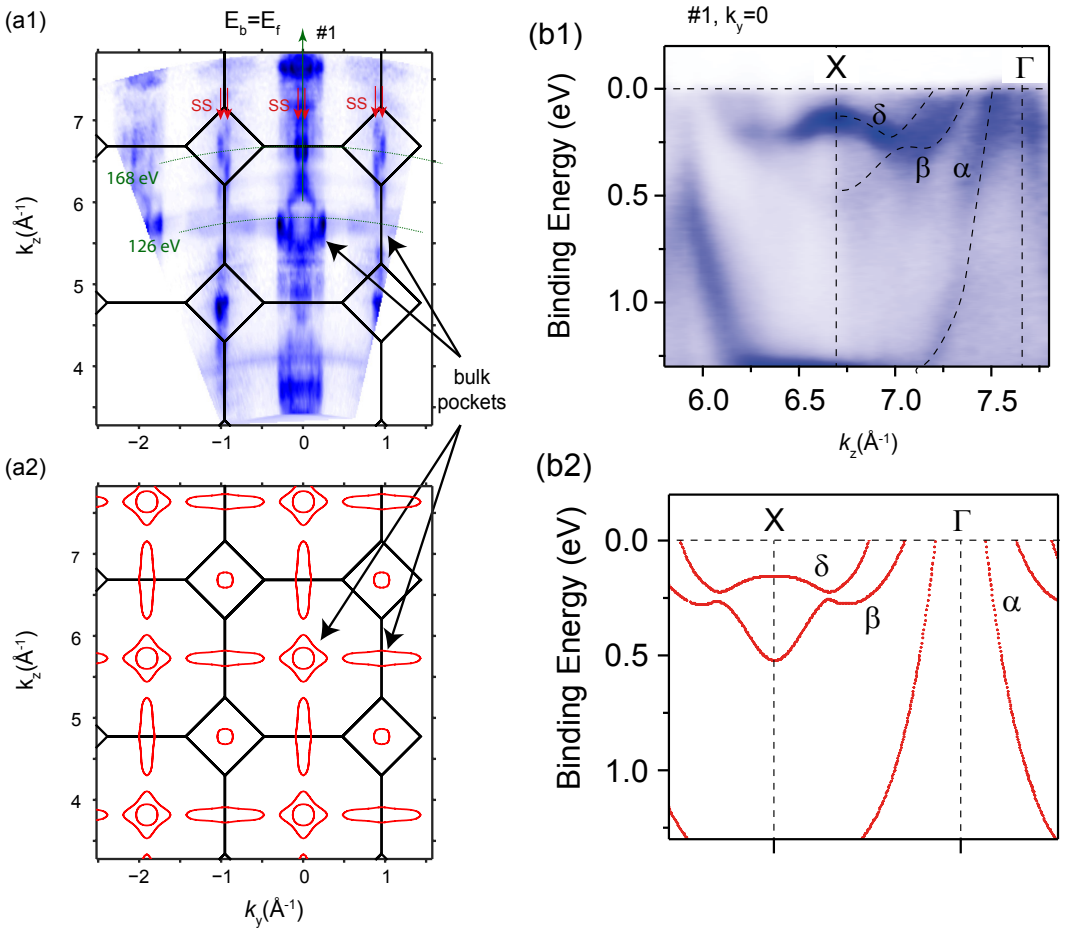


Figure 3.10: k_z **dependence of surface states and bulk bands in LaBi.** (a1-2) Experimental and theoretical Fermi surface for the k_y vs. k_z plane, respectively. Red arrows indicate surface states that are nondispersive along k_z. Green dashed lines indicate the k_z positions of the cuts taken at hv=126 eV and 168 eV shown in the previous figures. Black arrows indicate position of bulk pockets. (b1-2) Experimental and theoretical band dispersion along the direction #1 indicated by the green arrow in (a1), respectively. Dashed black lines are guide to the eye. For the transformation of the experimental data, the free-electron final state approximation with inner potential V_0 =9 eV was used. Figures were drawn in joint collaboration with Juan Jiang, Advanced Light Source, Lawrence Berkeley National Lab, USA, and will be published in Ref. [67].

field and thereby confirm a theoretically predicted volume by varying the angle between sample and field - were so far unable to observe a frequency corresponding to the octahedral outer hole pocket in LaBi[5] [44, 43, 42]. Thus, another independent experimental investigation of the carrier compensation status in LaBi is urged, which is particularly pressing since LaBi's nontrivial topology has also been related to the appearance of the XMR.

In order to fill this gap in the current literature, we further analyzed the experimentally obtained Fermi surfaces to determine the volumes of the electron and hole pockets. Since the Fermi pocket volumes in the Brillouin zone are proportional to the carrier densities in the unit cell, the ratio of the pocket volumes will give the ratio of the carrier densities. To determine the Fermi pocket volumes, we performed a peak fitting to the momentum-distribution curves at the Fermi energy to our data shown in Figures 3.7 and 3.8 to determine the shape of the Fermi surface pocket cross-section in the $k_z = \Gamma$ and $k_z = X$ plane. The results of the peak fitting, which was performed by Dr Juan Jiang, is shown in Figure 3.11 for two representative high symmetry directions. Figure 3.11(a) shows a fitting of the bands in the $k_z = \Gamma$ plane along the high symmetry line $X^* - \Gamma - X^*$with six observer peaks tracking the $\alpha-$ and $\beta-$pockets, as well as the surface state pocket. Additionally, a constant background for all $k_{\backslash\backslash}$ was included. Since the peaks of the surface state pocket and the inner $\alpha-$hole pocket in Figure 3.11(a) are very close to each other, the fitting with six observer peaks yielded an nonphysical result: the left and right hand side of of the observer peak positions were not symmetric, although they should be according to the symmetry of the Brillouin zone. Thus, this fitting result cannot be reliable. To improve the fitting, the author of this thesis suggested to neglect the surface state contribution and only fit the bulk hole pockets with four observer peaks. The result of the improved fitting by Dr Jiang is shown in Figure 3.11(b), which shows symmetric observer peaks which are at positions very close to the local maximums of the

[5]Note that the same was true until recently about LaSb. However, the authors of Ref. [58] seem to have successfully measured all pockets in LaSb.

raw data. A representative fitting of the bands forming the electron pockets in the $k_z = X$ plane is shown in Figure 3.11(c) and shows a very good agreement with the experimental data.

The peak positions extracted from the fitting on and off the high symmetry lines are shown in Figures 3.12(a,1-2). Based on the band structure calculations, we approximated the three dimensional shape of the Fermi surface pockets with an ellipse for the electron pocket, a sphere for the inner hole pocket, and an octahedral shape for the outer hole pocket, which were then fitted to the experimental cross-sections. The resulting three dimensional pockets are shown in Figures 3.12(a,3).

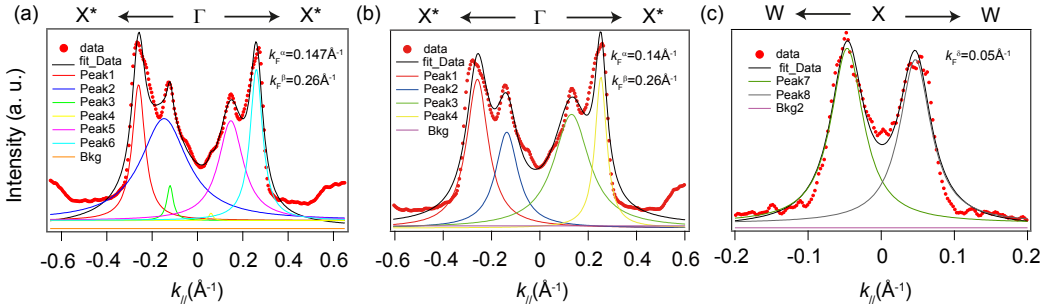


Figure 3.11: **Results of the peak fitting along two high symmetry lines.** (a) Peak fitting of the bands in the $k_z = \Gamma$ plane along the $X^* - \Gamma - X^*$ path with six observer peaks. (b) Peak fitting of the bands in the $k_z = \Gamma$ plane along the $X^* - \Gamma - X^*$ path with four observer peaks. (c) Peak fitting of the bands in the $k_z = X$ plane along the $W - X - W$ plane. Observer peaks and background are shown as solid lines, while the raw data is represented by red dots.

From our approximation of the Fermi surfac pocket volumes, we were able to approximate the carrier density ratio as $n_e/n_h = 0.4 \pm 0.1$, which largely deviates from unity. We furthermore determined in the same manner the carrier density ratio in a second sample, which gave $n_e/n_h = 0.6 \pm 0.1$. The experimental Fermi surfaces for these two samples are compared in Figures 3.12(b,1) and (c,1), which indicates larger electron pockets in sample 2 than in sample 1. The volume difference can be explained by a shift in the Fermi level, which is also apparent in the band dispersions of the surface state at $\overline{M}$, which show a energy shift of the Dirac point positions of about ≈ 100 meV, as shown in Figures 3.12(b,2) and (c,2).

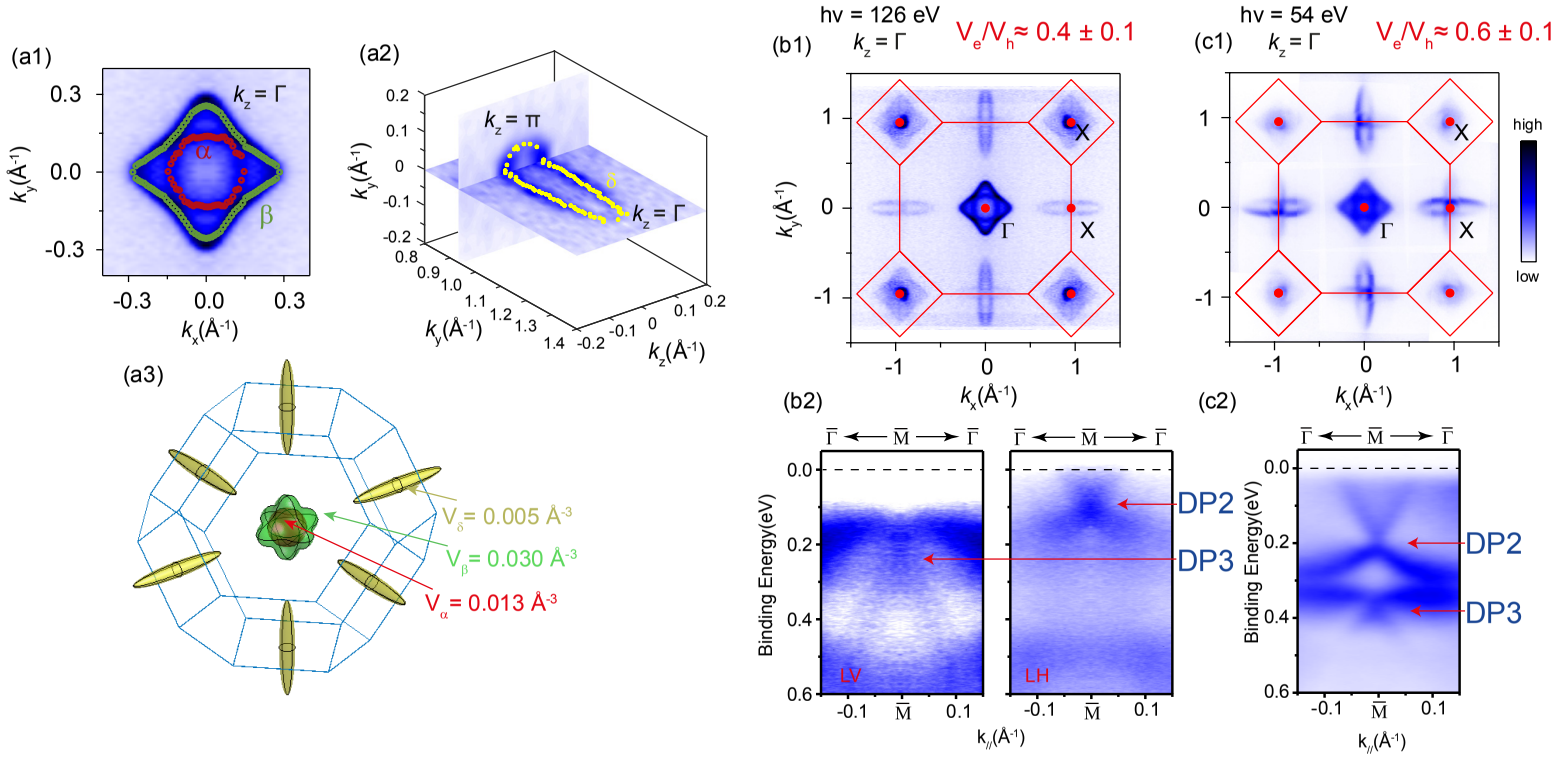


Figure 3.12: **Determination of Fermi surface pocket volumes in LaBi.** (a,1-2) Peak positions of the hole pocket and electron pocket bands at the Fermi level, extracted from momentum distribution curve fitting. (a,3) Resulting three dimensional volume of the hole and electron pockets in the Brillouin zone. (b,1-2) Sample 1: Fermi surface and surface state dispersion at $\overline{M}$, respectively. Taken at $hv = 126$ eV, $k_z = \Gamma$. (c,1-2) Sample 2: Fermi surface and surface state dispersion at $\overline{M}$, respectively. Taken at $hv = 54$ eV, $k_z = \Gamma$. All measurements were taken with linear-horizontal polarization (LH), except for the first panel in figure (b2), which was taken with linear-vertical (LV) polarization. Figures were drawn in joint collaboration with Juan Jiang, Advanced Light Source, Lawrence Berkeley National Lab, USA, and will be published in Ref. [67].

Sample #	Residual Resistivity Ratio	MR(%) @ T=2K and B=9T
1	339	90000
2	205	42200
3	193	38000
4	190	45000
5	180	42000

Table 3.1: Magnetoresistance measurements of samples from the same batch as those used for the ARPES measurements presented here.

We now tried to investigate the consequences of our findings for the applicability of the two band model description of the XMR, as given in Equation 3.1. Both of our samples used for the ARPES measurements came from the same growth method and the same batch, which were grown by Nitesh Kumar, Max-Planck Institute for Chemical Physics of Solids in Dresden, Germany. Our collaborators in Dresden selected five samples from this batch for magnetotransport measurements, which all resulted in the same order of magnitude of magnetoresistance at B =9T, which are shown in Table 3.1. It is plausible to assume that the samples measured in our ARPES measurement would show a magnetoresistance of the same order of magnitude as the other samples from the batch. We performed a fitting to the field dependence of the magnetoresistance with the two band model formula presented in equation 3.1 under the assumption of a carrier density ratio $n_e/n_h = 0.36$, which is within the error range that we determined in the ARPES measurements. We used three sets of data for the fitting: Figure 3.13(a) shows the experimental data obtained by our collaborators for one of the samples, with up to $MR \approx 80000\%$ at B =9T. To simulate the variation of the magnetoresistance across the batch, we created two additional artificial datasets by rescaling the experimental results by a factor of 0.5 (corresponding to the lowest observed XMR in real LaBi samples with up to $MR \approx 40000\%$ at B =9T) and a factor 0.1. Note that the assumption behind the rescaling is that the magnetoresistance may be weaker in some samples due to a higher residual resistance at zero field $\rho_{xx}(B = 0)$, but that it maintains the parabolic shape. The fitting curves show good agreement, but the fitting results in an extremely large mobility differences (three to

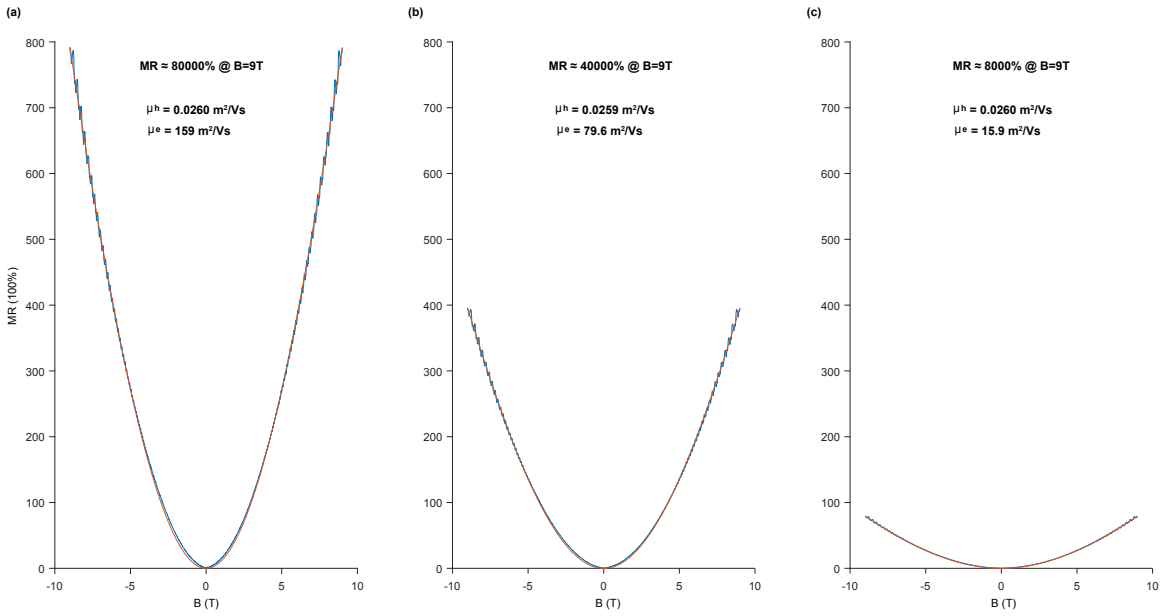


Figure 3.13: **Fitting of the two-band model to experimental and rescaled magnetoresistance data of LaBi.** (a) Experimental field dependence of the magnetoresistance (blue) and fitting curve (orange) based on the two-band model, taken at temperature T =2K. (b-c) Rescaled magnetoresistance data with factors 0.5 and 0.1, respectively, to simulate variation of magnetoresistance among different samples. All fittings assumed carrier density ratio $n_e/n_h = 0.36$ obtained by ARPES. Fitting parameter results for the mobilities are given as insets. Experimental data courtesy of Nitesh Kumar, Max-Planck Institute for Chemical Physics of Solids in Dresden, Germany.

four orders of magnitude, as given in Figure 3.13) between electrons and holes, which is two to three orders of magnitude larger than what was suggested by He et al. for YSb.

3.5 Discussion of the results and perspectives for future research

Before starting out discussion, let us briefly summarize the results presented above. We have shown that

1. LaBi shows a double Dirac cone surface state at the $\overline{M}$ point and a single Dirac cone at the $\overline{\Gamma}$ bar point, as was predicted by the band structure calculations of

our collaborators.

2. two LaBi samples measured by ARPES show a large electron/hole carrier density imbalance. A fitting of the two band model to the field dependence of the magnetoresistance leads to an extremely large mobility imbalance between electron and hole carriers.

What do these findings imply for the research questions that we have formulated above?

Firstly, as we have mentioned before, the special surface state structure is the hallmark of a strong topological phase, which means that LaBi is topologically nontrivial. This is remarkable, since the topological phase remains robust despite the absence of a global gap that is present in topological insulators. Thus LaBi is a topological semimetal with a local band gap and surface states similar to a topological insulator (which have closed Fermi surfaces), which is different from the recently discovered topological Weyl semimetals that have no local band gap and host topological Fermi-arc surface states (which show open Fermi surfaces when considering only one side of a sample) [74, 75, 76]. As we have seen before, it has been shown that LaSb is topologically trivial, which is most likely due to the weaker spin-orbit coupling caused by the lighter pnictogen atom. Therefore, it can be expected that LaP and LaAs, which include even lighter pnictogen atoms, are also topologically trivial, which also holds for YSb, as we have seen before. Thus, LaBi stands out as the only compound in the lanthanum monopnictide family that is topologically nontrivial. This finding opens the possibility for further research to study the topological phase transition that can be expected by doping LaBi with lighter elements. Furthermore, it would be interesting to investigate the interplay between topology and electronic correlations in LaBi, which most recently has been found to become superconducting under pressure [77]. If LaBi remains topologically nontrivial under pressure, it may therefore become a topological superconductor, which has been been proposed to host exotic Majorana fermions that are their own antiparticles and may be relevant for applications in

quantum computing.

Secondly, the absence of carrier compensation and the strong variation of the Fermi level between samples is surprising, since previous ab-initio studies assumed that LaBi would be compensated, similar to the trivial LaSb. However, it is not uncommon that the Fermi level of real samples may deviate from theoretical predictions, since during growth there may be self doping effects e.g. due to vacancies. It therefore is important whether the carrier densities that were deduced from the ARPES results are representative of the real carrier densities in the bulk sample. It should be noted that ARPES probes electrons close to the sample surface, and that the surface sensitivity can affect properties such as spin-polarization of the photo-emitted electrons [78]. On the other hand, it has been shown that carrier densities deduced from ARPES broadly agree with bulk sensitive probes, such as quantum osciallations , for high carrier density samples[6], as long as no contamination of the surface takes place [79]. Since LaBi has relatively large Fermi surface pockets, the effect of band bending should be small, and since the samples were cleaved in ultra-high vacuum, the sample surface should be clean and relatively free of contamination. It remains therefore unclear why the Fermi surface volumes measured at the surface of LaBi by ARPES should be different from the bulk. To further investigate this question, a combination of quantum oscillation and ARPES studies on the same samples are urged, which is important, since we have found that the Fermi level between samples from the same batch may vary to an extend that may significantly affect the carrier compensation status. This finding of a variable Fermi level between different samples may also explain the apparent inconstancy between carrier densities determined by ARPES and quantum oscillations in YSb. If the ARPES results are indeed a reliable probe for the density in the bulk, this would substantially question the prevalent theory for the origin of the XMR in LaBi. Given that the XMR effect is ubiquitous in all of the samples measured by our collaborators (see Table 3.1), as well as all the

[6]Note that for low carrier density samples, the effect of band bending at the surface may become significant, see e.g. Ref. [79].

samples measured by all other groups [44, 43, 42], it can be assumed that the XMR effect should also be present in two samples measured in our ARPES experiments. Applying a two band model that incorporate the carrier densities from our ARPES measurements resulted in an extremely large mobility difference, which substantially larger than what was suggested for YSb [49]. It is unclear what could cause such an extremely large carrier mobility difference, and it seems more likely that the two band model description of LaBi breaks down. Incorporating a three band model, which treats the inner and outer hole pocket carriers separately [80], leads to essentially similar mobility amplitudes, which is most likely due to the fact that the inner hole pocket density is negligible compared to the outer hole pocket density. So far, the only alternative hypothesis for the origin of the XMR is the proposal by Tafti et al. [44], which relates the large mobilities found in the absence of a magnetic field to LaBi's nontrivial topology. However, this hypothesis has so far no theoretical foundation, since in our current understanding only carriers in topological surface states are protected from backscattering, and it is unclear how this mechanism may explain the parabolic field dependence of the magnetoresistance. Thus, the true origin of the XMR in LaBi remains a subject of further investigation.

References

[35] A Iandelli and E Botti. Sulla struttura cristallina dei composti delle terre rare con i metalloidi del V gruppo. Composti 1:1 col bismuto. *Atti della Accademia Nazionale dei Lincei, Classe di Fisiche, Matematiche e Naturali, Rendiconti*, **26**:p233–p238, 1937.

[36] A Iandelli and E Botti. Sulla struttura cristallina dei composti delle terre rare con i metalloidi del V gruppo. - Fosfuri di lantanio, cerio e prasiodimio. *Atti della Accademia Nazionale dei Lincei, Classe di Scienze Fisiche, Matematiche e Naturali, Rendiconti, Serie 7 (1, 1925-1945)*, **24**:p459–p464, 1936.

[37] A Iandelli and E Botti. Sulla struttura cristallina dei composti delle terre rare con i metalloidi del V gruppo. - Arseniuri e antimoniuri di lantanio, cerio e prasiodimio. *Atti della Accademia Nazionale dei Lincei, Classe di Scienze Fisiche, Matematiche e Naturali, Rendiconti, Serie 7*, **25**:p498–p502, 1937.

[38] LH Brixner. Structure and electrical properties of some new rare earth arsenides, antimonides and tellurides. *Journal of Inorganic and Nuclear Chemistry*, **15**(1-2):199–201, 1960.

[39] Minggang Zeng, Chen Fang, Guoqing Chang, Yu-An Chen, Timothy Hsieh, Arun Bansil, Hsin Lin, and Liang Fu. Topological semimetals and topological insulators in rare earth monopnictides. *arXiv preprint arXiv:1504.03492*, 2015.

[40] Zhi Ren, A. A. Taskin, Satoshi Sasaki, Kouji Segawa, and Yoichi Ando. Large bulk resistivity and surface quantum oscillations in the topological insulator Bi_2Te_2Se. *Physical Review B*, **82**:241306, Dec 2010.

[41] FF Tafti, QD Gibson, SK Kushwaha, N Haldolaarachchige, and RJ Cava. Resistivity plateau and extreme magnetoresistance in LaSb. *Nature Physics*, **12**(3):272, 2016.

[42] Shanshan Sun, Qi Wang, Peng-Jie Guo, Kai Liu, and Hechang Lei. Large magnetoresistance in LaBi: Origin of field-induced resistivity upturn and plateau in compensated semimetals. *New Journal of Physics*, **18**(8):082002, 2016.

[43] Nitesh Kumar, Chandra Shekhar, Shu-Chun Wu, Inge Leermakers, Olga Young, Uli Zeitler, Binghai Yan, and Claudia Felser. Observation of pseudo-two-dimensional electron transport in the rock salt-type topological semimetal LaBi. *Physical Review B*, **93**(24):241106, 2016.

[44] Fazel Fallah Tafti, Quinn Gibson, Satya Kushwaha, Jason W. Krizan, Neel Haldolaarachchige, and Robert Joseph Cava. Temperature-field phase diagram of extreme magnetoresistance. *Proceedings of the National Academy of Sciences*, **113**(25):E3475–E3481, 2016.

[45] Orest Pavlosiuk, Przemysław Swatek, and Piotr Wiśniewski. Giant magnetoresistance, three-dimensional Fermi surface and origin of resistivity plateau in YSb semimetal. *Scientific reports*, **6**, 2016.

[46] NJ Ghimire, AS Botana, D Phelan, H Zheng, and JF Mitchell. Magnetotransport of single crystalline YSb. *Journal of Physics: Condensed Matter*, **28**(23):235601, 2016.

[47] Peng-Jie Guo, Huan-Cheng Yang, Bing-Jing Zhang, Kai Liu, and Zhong-Yi Lu. Charge compensation in extremely large magnetoresistance materials LaSb and LaBi revealed by first-principles calculations. *Physical Review B*, **93**(23):235142, 2016.

[48] John M Ziman. *Principles of the Theory of Solids*. Cambridge University Press, 1972.

[49] Junfeng He, Chaofan Zhang, Nirmal J. Ghimire, Tian Liang, Chunjing Jia, Juan Jiang, Shujie Tang, Sudi Chen, Yu He, S.-K. Mo, C. C. Hwang, M. Hashimoto, D. H. Lu, B. Moritz, T. P. Devereaux, Y. L. Chen, J. F. Mitchell, and Z.-X. Shen. Distinct Electronic Structure for the Extreme Magnetoresistance in YSb. *Physical Review Letters*, **117**:267201, Dec 2016.

[50] L.-K. Zeng, R. Lou, D.-S. Wu, Q. N. Xu, P.-J. Guo, L.-Y. Kong, Y.-G. Zhong, J.-Z. Ma, B.-B. Fu, P. Richard, P. Wang, G. T. Liu, L. Lu, Y.-B. Huang, C. Fang, S.-S. Sun, Q. Wang, L. Wang, Y.-G. Shi, H. M. Weng, H.-C. Lei, K. Liu, S.-C. Wang, T. Qian, J.-L. Luo, and H. Ding.

Compensated Semimetal LaSb with Unsaturated Magnetoresistance. *Physical Review Letters*, **117**:127204, Sep 2016.

[51] Tian Liang, Quinn Gibson, Mazhar N Ali, Minhao Liu, RJ Cava, and NP Ong. Ultrahigh mobility and giant magnetoresistance in the Dirac semimetal Cd3As2. *Nature Materials*, **14**(3):280–284, 2015.

[52] Chandra Shekhar, Ajaya K. Nayak, Yan Sun, Marcus Schmidt, Michael Nicklas, Inge Leermakers, Uli Zeitler, Yurii Skourski, Jochen Wosnitza, Zhongkai Liu, Yulin Chen, Walter Schnelle, Horst Borrmann, Yuri Grin, Claudia Felser, and Binghai Yan. Extremely large magnetoresistance and ultrahigh mobility in the topological Weyl semimetal candidate NbP. *Nature Physics*, **11**(8):645–649, 2015.

[53] Nirmal Jeevi Ghimire, Yongkang Luo, Madhab Neupane, DJ Williams, ED Bauer, and F Ronning. Magnetotransport of single crystalline NbAs. *Journal of Physics: Condensed Matter*, **27**(15):152201, 2015.

[54] Xiaochun Huang, Lingxiao Zhao, Yujia Long, Peipei Wang, Dong Chen, Zhanhai Yang, Hui Liang, Mianqi Xue, Hongming Weng, Zhong Fang, Xi Dai, and Genfu Chen. Observation of the Chiral-Anomaly-Induced Negative Magnetoresistance in 3D Weyl Semimetal TaAs. *Physical Review X*, **5**:031023, Aug 2015.

[55] Mazhar N. Ali, Jun Xiong, Steven Flynn, Jing Tao, Quinn D. Gibson, Leslie M. Schoop, Tian Liang, Neel Haldolaarachchige, Max Hirschberger, N. P. Ong, and R. J. Cava. Large, non-saturating magnetoresistance in WTe2. *Nature*, **514**(7521):205–208, 2014.

[56] Kefeng Wang, D Graf, Lijun Li, Limin Wang, and C Petrovic. Anisotropic giant magnetoresistance in NbSb2. *Scientific Reports*, **4**:7328, 2014.

[57] Eundeok Mun, Hyunjin Ko, Gordon J. Miller, German D. Samolyuk, Sergey L. Bud'ko, and Paul. C. Canfield. Magnetic field effects on transport properties of $PtSn_4$. *Phys. Rev. B*, **85**:035135, Jan 2012.

[58] F. Han, J. Xu, A. S. Botana, Z. L. Xiao, Y. L. Wang, W. G. Yang, D. Y. Chung, M. G. Kanatzidis, M. R. Norman, G. W. Crabtree, and W. K. Kwok. Separation of Electron and Hole Dynamics in the Semimetal LaSb. *ArXiv e-prints*, August 2017.

[59] H. Oinuma, S. Souma, D. Takane, T. Nakamura, K. Nakayama, T. Mitsuhashi, K. Horiba, H. Kumigashira, M. Yoshida, A. Ochiai, T. Takahashi, and T. Sato. Three-dimensional band structure of LaSb and CeSb: Absence of band inversion. *Physical Review B*, **96**:041120, Jul 2017.

[60] John P. Perdew, Kieron Burke, and Matthias Ernzerhof. Generalized Gradient Approximation Made Simple. *Physical Review Letters*, **77**:3865–3868, Oct 1996.

[61] X. H. Niu, D. F. Xu, Y. H. Bai, Q. Song, X. P. Shen, B. P. Xie, Z. Sun, Y. B. Huang, D. C. Peets, and D. L. Feng. Presence of exotic electronic surface states in LaBi and LaSb. *Phys. Rev. B*, **94**:165163, Oct 2016.

[62] P. Blaha, K. Schwarz, G. Madsen, D. Kvasnicka, and J. Luitz. *WIEN2k, An Augmented Plane Wave + Local Orbitals Program for Calculating Crystal Properties*. Karlheinz Schwarz, Techn. Universitaet Wien, Austria, 2001.

[63] Akira Hasegawa. Fermi Surface of LaSb and LaBi. *Journal of the Physical Society of Japan*, **54**(2):677–684, 1985.

[64] A Hasegawa. Electronic structure of La monopnictides. *Journal of Physics C: Solid State Physics*, **13**(33):6147, 1980.

[65] L Petit, R Tyer, Z Szotek, W M Temmerman, and A Svane. Rare earth monopnictides and monochalcogenides from first principles: towards an electronic phase diagram of strongly correlated materials. *New Journal of Physics*, **12**(11):113041, 2010.

[66] N. Alidoust, A. Alexandradinata, S.-Y. Xu, I. Belopolski, S. K. Kushwaha, M. Zeng, M. Neupane, G. Bian, C. Liu, D. S. Sanchez, P. P. Shibayev, H. Zheng, L. Fu, A. Bansil, H. Lin, R. J. Cava, and M. Zahid Hasan. A new form of (unexpected) Dirac fermions in the strongly-correlated cerium monopnictides. *ArXiv e-prints*, April 2016.

[67] J. Jiang*, N. B. M. Schröter*, S.-C. Wu, N. Kumar, C. Shekhar, H. Peng, X. Xu, C. Chen, H.F. Yang, C.-C. Hwang, S.-K. Mo, C. Felser, B.H. Yan, Z.K. Liu, L.X. Yang, and Y.L. Chen. Observation of Topological Surface States and Strong Electron/hole Imbalance in Extreme Magnetoresistance Compound LaBi. (submitted, under review. *these authors contributed equally).

[68] G Timp, PD Dresselhaus, TC Chieu, G Dresselhaus, and Y Iye. Anomalous magnetoresistance of graphite at high magnetic fields. *Physical Review B*, **28**(12):7393, 1983.

[69] Benoît Fauqué, Baptiste Vignolle, Cyril Proust, Jean-Paul Issi, and Kamran Behnia. Electronic instability in bismuth far beyond the quantum limit. *New Journal of Physics*, **11**(11):113012, 2009.

[70] VN Strocov. Intrinsic accuracy in 3-dimensional photoemission band mapping. *Journal of Electron Spectroscopy and related phenomena*, **130**(1):65–78, 2003.

[71] J. Xu, N. J. Ghimire, J. S. Jiang, Z. L. Xiao, A. S. Botana, Y. L. Wang, Y. Hao, J. E. Pearson, and W. K. Kwok. Origin of the extremely

large magnetoresistance in the semimetal YSb. *Physical Review B*, **96**:075159, Aug 2017.

[72] Jayita Nayak, Shu-Chun Wu, Nitesh Kumar, Chandra Shekhar, Sanjay Singh, Jörg Fink, Emile E. D. Rienks, Gerhard H. Fecher, Stuart S. P. Parkin, Binghai Yan, and Claudia Felser. Multiple Dirac cones at the surface of the topological metal LaBi. *Nature Communications*, **8**:13942, 2017.

[73] R. Lou, B.-B. Fu, Q. N. Xu, P.-J. Guo, L.-Y. Kong, L.-K. Zeng, J.-Z. Ma, P. Richard, C. Fang, Y.-B. Huang, S.-S. Sun, Q. Wang, L. Wang, Y.-G. Shi, H. C. Lei, K. Liu, H. M. Weng, T. Qian, H. Ding, and S.-C. Wang. Evidence of topological insulator state in the semimetal LaBi. *Physical Review B*, **95**:115140, Mar 2017.

[74] Su-Yang Xu, Ilya Belopolski, Nasser Alidoust, Madhab Neupane, Guang Bian, Chenglong Zhang, Raman Sankar, Guoqing Chang, Zhujun Yuan, Chi-Cheng Lee, Shin-Ming Huang, Hao Zheng, Jie Ma, Daniel S. Sanchez, BaoKai Wang, Arun Bansil, Fangcheng Chou, Pavel P. Shibayev, Hsin Lin, Shuang Jia, and M. Zahid Hasan. Discovery of a Weyl fermion semimetal and topological Fermi arcs. *Science*, **349**(6248):613–617, 2015.

[75] B. Q. Lv, N. Xu, H. M. Weng, J. Z. Ma, P. Richard, X. C. Huang, L. X. Zhao, G. F. Chen, C. E. Matt, F. Bisti, V. N. Strocov, J. Mesot, Z. Fang, X. Dai, T. Qian, M. Shi, and H. Ding. Observation of Weyl nodes in TaAs. *Nat Phys*, **11**(9):724–727, 2015.

[76] L. X. Yang, Z. K. Liu, Y. Sun, H. Peng, H. F. Yang, T. Zhang, B. Zhou, Y. Zhang, Y. F. Guo, M. Rahn, D. Prabhakaran, Z. Hussain, S. K. Mo, C. Felser, B. Yan, and Y. L. Chen. Weyl semimetal

phase in the non-centrosymmetric compound TaAs. *Nat Phys*, **11**(9):728–732, 2015.

[77] F. F. Tafti, M. S. Torikachvili, R. L. Stillwell, B. Baer, E. Stavrou, S. T. Weir, Y. K. Vohra, H.-Y. Yang, E. F. McDonnell, S. K. Kushwaha, Q. D. Gibson, R. J. Cava, and J. R. Jeffries. Tuning the electronic and the crystalline structure of LaBi by pressure: From extreme magnetoresistance to superconductivity. *Physical Review B*, **95**:014507, Jan 2017.

[78] J. M. Riley, MeevasanaW, BawdenL, AsakawaM, TakayamaT, EknapakulT, T. K. Kim, HoeschM, S. K. Mo, TakagiH, SasagawaT, M. S. Bahramy, and P. D. C. King. Negative electronic compressibility and tunable spin splitting in WSe2. *Nat Nano*, **10**(12):1043–1047, 2015.

[79] James G. Analytis, Jiun-Haw Chu, Yulin Chen, Felipe Corredor, Ross D. McDonald, Z. X. Shen, and Ian R. Fisher. Bulk Fermi surface coexistence with Dirac surface state in Bi_2Se_3: A comparison of photoemission and Shubnikov–de Haas measurements. *Phys. Rev. B*, **81**:205407, May 2010.

[80] Tadao Kasuya, Masafumi Sera, Yasushi Okayama, and Yoshinori Haga. Normal and Anomalous Hall Effect in CeSb and CeBi. *Journal of the Physical Society of Japan*, **65**(1):160–171, 1996.

Chapter 4

Discovery of a weak topological phase in the semimetal $TaSb_2$

As we have learned in the introductory chapter about topological band theory, three dimensional topological insulators with time-reversal symmetry are characterized by a topological index $(v_0; v_1, v_2, v_3)$. Fu and Kane proposed to divide them into two classes: *strong* topological insulators, for which the strong index is $v_0 = 1$; and *weak* topological insulators, for which $v_0 = 0$, but at least one weak index $v_i = 1$ $(i = 1, 2, 3)$. Almost all so far known topological insulators are *strong* topological insulators [81], and we will see later that for the few *weak* topological insulator candidates, there is only indirect experimental evidence for their topological classification. In this chapter, we will first review the theoretical background for weak topological insulators, as well as the experimental evidence for their existence reported in the literature so far. We will subsequently present band structure calculations for the semimetal $TaSb_2$ and related compounds $NbAs_2$ and $TaAs_2$, which predict that this material family should host a *weak* topological phase, as well as exotic magnetotransport data, which makes these transition-metal dipnictides an interesting research subject. Finally, we will present our experimental data on $TaSb_2$ – complemented with surface band structure calculations – which for the first time provides direct evidence for the existence of

a weak topological phase by measuring a trivial *dark surface* without topological surface states, as well as a nontrivial *topological surface* with topological surface states. Additionally, we will show that $NbAs_2$ and $TaAs_2$ may also be topologically nontrivial. Some of the Figures presented here will be published in Ref. [114]. Most of the presented data was was taken by the author of this thesis at beamline I05 of the Diamond Light Source, UK, except for the data shown in Figure 4.5(b,i) and (c,i), which the author took at the beamline APE in Elettra, and Figures 4.3 and 4.4, which were taken by Dr. Jiang at beamline 10.0.1 at the Advanced Light Source. The author of this thesis conducted all of the data analysis and prepared all of the figures. Our study was supported by the co-authors of Ref. [114]. All measurements were taken at a temperatures below T=20 K and in an UHV environment with base pressure better than 3×10^{-10} mbar.

4.1 Previous theoretical and experimental studies of weak topological insulators

Fu and Kane coined the terms *weak* and *strong* topological insulators (TIs) with respect to the protection of Kramers degeneracies against disorder. They argued that the strong topological phase and topological invariant v_0 would retain their meaning in the presence of disorder, while weak topological invariants (v_1, v_2, v_3) are only defined for clean systems with perfect translational invariance [82]. However, it was later shown that weak topological insulators are in fact more robust against disorder than Fu and Kane originally believed. To understand their arguments, as well as the experimental results presented subsequently, we want to give a brief review about the theoretical background of weak and strong TIs.

4.1.1 Theoretical background of weak TIs

In the previous introductory chapter about topological band theory, we learned that topological insulators are characterized by a single $\mathbb{Z}_2$ invariant in two dimensions that leads to helical edge states. such two-dimensional TI is also called the *quantum spin hall insulator* (QSHI) phase. The simplest route to construct a three-dimensional TIs from their two-dimensional counterparts is to stack QSHI layers on top of each other. The top and and bottom surface of this stack remains insulating, whilst the side surfaces form anisotropic surface states. This three-dimensional topological insulator will have $v_0 = 0$, since we have seen in the previous theory chapter that if $v_0 = 1$, then the product $\pi(\Lambda_1)\pi(\Lambda_2)\pi(\Lambda_3)\pi(\Lambda_4) = -1$ for the time-reversal invariant moments (TRIMs) Λ_i of any surface, but this would imply that there will be a metallic surface state on the top and bottom surface, which is not the case here. However, the weak indices of this insulator are nontrivial, and they define the stacking direction of the layers $\boldsymbol{G}^{v_1,v_2,v_3} = v_1\boldsymbol{b_1} + v_2\boldsymbol{b_2} + v_3\boldsymbol{b_3}$, where $\boldsymbol{b_1}, \boldsymbol{b_2}, \boldsymbol{b_3}$ are the primitive reciprocal lattice vectors [82]. Note, however, that there is some ambiguity in the definition of the stacking direction [83], thus all surfaces with miller index $[h_1, h_2, h_3]$ that fulfill the condition

$$(h_i - v_i) \bmod 2 = 0, \tag{4.1}$$

where $i = 1, 2, 3$, will have only trivial surface states, but no topological ones that show an odd number of crossings between TRIMs.

We have argued before that a strong topological insulator with $v_0 = 1$, which cannot be adiabatically connected to the stacked QSHI system, will have an odd number of Dirac points in the Brillouin zone. Due to the counterpropagation of electrons with opposite spin on the surface, electron spins are rotating by 2π when the electron is transported around a Dirac point on the Fermi surface, which leads to a Berry phase of π. This nontrivial Berry phase leads to a sign change in the weak

localization correction[1] for weakly disordered systems. Also in the presence of strong disorder it has been shown that the surface states of strong TIs cannot be localized [84].

A weak topological insulator can be adiabatically connected to the stack of QSHI states that we described above. Fu and Kane argued that a pairwise coupling of neighboring layers (which would violate lattice translational symmetry) will gap the edge modes, and that a random disorder that breaks translation symmetry would thus lift the protection of the Kramers pairs in weak TIs and lead to Anderson localization of surface states while preserving time-reversal symmetry. However, Ringel and coworkers [83] have shown that as long as the random disorder is not strong enough to close the bulk band gap, there will always be delocalized states on the surface of a weak TI, independent of the strength of the disorder. They showed that for the case of weak disorder, there will be a similar antilocalization correction to the classical conductivity as in the case of strong TIs. Strong disorder in the surfaces layers will make those insulating, but creates a perfect metallic sheet beneath the disordered surface. Mong and coworkers [85] showed that in the case of a special disorder potential, the weak TIs can show a unique scaling behavior of the conductivity with system size that can lead to localization. However, due to the lack of experimental candidates, the question of the topological protection of the surface states of a weak topological insulator remains largely unexplored.

Besides their exotic surface states, weak topological insulators have also been predicted to show exotic one-dimensional metallic channels on line dislocations [86], as well as on step edges [87]. Similar to the edge states of a quantum-spin hall system, the spin of the electrons in these 1D channels is polarized in a way that counterpropagating electrons have opposite spin. As a result, a similar topological protection from backscattering is expected for these electrons as for two-dimensional topological insulators [87]. These predictions may offer interesting possibilities to design spin-

[1]Weak localization is a quantum mechanical correction to the classical resistivity in weakly disordered systems that is usually positive, but negative for surface states of strong TIs.

poarized circuits by engineering a network of step-edges or line dislocations on the insulating *dark* surface of a weak TI. However, due to the lack of experimental candidates, there are so far no studies reporting the investigation of devices based on such designs.

In the following, we want to briefly review the few weak topological insulator candidate materials that have been investigated experimentally, which will highlight the need for ARPES studies of the topological surface states in weak TIs.

4.1.2 Literature review of experimental evidence for the existence of weak TIs

The major obstacle in the experimental verification of weak topological insulators is the lack of natural cleaving planes that would allow access to both the *dark surface* of a weak TI (which may host trivial, but no topological surface states, such as the top and bottom of a QSHI stack) as well as the *topological surface,* which hosts an even number of topological surface states. As a result, there is only one theoretical prediction of a weak TI candidate material that can be cleaved on two surfaces, β-Bi_4I_4, which was initially predicted to have the topological index (0; 0 0 1) [88]. However, the method used for this prediction were standard *density functional theory* calculations employing the generalized gradient approximation, which resulted in a relatively small band gap of 0.158 eV. Such a small gap casted doubt on the validity of the topological classification. Indeed, more sophisticated calculations based on the GW-approximation [88], as well as hybrid functionals [89] showed a change in the number of band inversions at different high symmetry points, which led to a more realistic topological classification of (1; 1 1 0). Thus, β-Bi_4I_4 is not a weak, but a strong TI, which was further corroborated by the measurement of topological surface states measured with ARPES [88]. However, the similar compound β-Bi_4Br_4 is predicted to be a weak TI [89].

Another important weak TI candidate is $Bi_{14}Rh_3I_9$, which consists of honeycomb

layers that have $RhBi_8$ cubes on their corners, which are separated by trivial insulating spacer layers [90]. The design principle behind this compound is to replicate the honeycomb lattice of graphene (which was the first QSHI candidate [84]), but to induce a much larger band gap due to the heavy Bismuth atoms. Ab-initio calculations predicted a weak topological phase with topological index (0; 0 0 1). Although this material can be easily cleaved, only the dark 001 surface is accessible for ARPES measurements, which show the absence of topological Dirac cones on this surface [90]. Although the lack of topological surface states can be expected on the dark surface, it is insufficient evidence that $Bi_{14}Rh_3I_9$ is indeed a weak TI, since it may just be a trivial insulator without any topological surface states. More convincing evidence is given by scanning tunneling spectroscopy studies (STS), which show the existence of subnanometer wide electron channels on step edges of the honeycomb layer [91]. However, since STS is not momentum resolved, it cannot provide conclusive evidence that the observed edge states are indeed of topological origin, i.e. that the edge states show an odd number of crossings between TRIMs, which – as we have seen in the theory chapter about topological band theory – is the hallmark of topological surface and edge states.

Similar to $Bi_{14}Rh_3I_9$, Bi_1Te_1 and Bi_2TeI are weak TI candidates[2] with predicted topological index (0; 0 0 1) [92, 95, 94] . As in the case of $Bi_{14}Rh_3I_9$, it is only possible to cleave these materials along the *dark surfaces*, and the only evidence for their nontrivial weak topology are states on step-edges, which have been investigated for Bi_2TeI via STS [93].

As we have seen from the brief literature review above, in the decade after the prediction of the weak topological insulator material class, only a few candidates were synthesized and measured successfully. However, "smoking gun" evidence of a momentum resolved surface state with odd number of Fermi level crossings between

[2]Note that both Bi_1Te_1 and Bi_2TeI are also predicted to be *topological crystalline insulators* [107]. As a result, they host additional surface states on their *dark surfaces* that are protected by crystalline symmetries, and not time-reversal symmetry. These surface states can be distinguished from the time-reversal protected ones, since they do not show odd crossings between TRIMs.

time-reversal invariant momenta – as has been shown many times for strong TIs – remains elusive for all experimentally investigated weak TI candidates up until now. The main obstacle for a conclusive identification of a weak topological phase remains the inability to cleave the candidate materials on surfaces that host topological surface states protected by time-reversal symmetry. In the following section, we will for the first time demonstrate the measurement of a weak topological phase by overcoming this limitation.

4.2 Prediction of weak topological phase and magnetotransport effects in the transition-metal dipnictide family TmX (Tm=Ta, Nb; X=As, Sb)

4.2.1 Unusual magnetotransport properties of the transition-metal dipnictides

The transition metal dipnictide family TmX (Tm=Ta, Nb; X=As, Sb) recently attracted interest due to their unusual magnetotransport properties. Similar to the lanthanum monopnictides discussed in the previous chapter, $NbAs_2$, $TaAs_2$ and $TaSb_2$ all show a resistivity plateau at low temperatures (exemplified for $TaAs_2$ in Figure 4.1(a)), and an extremely large transverse[3] magnetoresistance (XMR) that remains unsaturated at large magnetic fields (see Figure 4.1(b) for $TaAs_2$) [97, 98, 96, 99, 101, 100]. For instance in $TaAs_2$, the magnetoresistance reaches up 200,000% at B =9 T and 4,000,000% at B =65 T [96]. Even more surprisingly, for all aforementioned compounds there are reports of negative longitudinal[4] magnetoresistance (see Figure 4.1(c)) [97, 96, 101].

[3]The transverse magneto resistance is measured when the magnetic field is perpendicular to the applied current direction.

[4]The longitudinal magnetoresistance is measured when the magnetic field is parallel to the applied current direction.

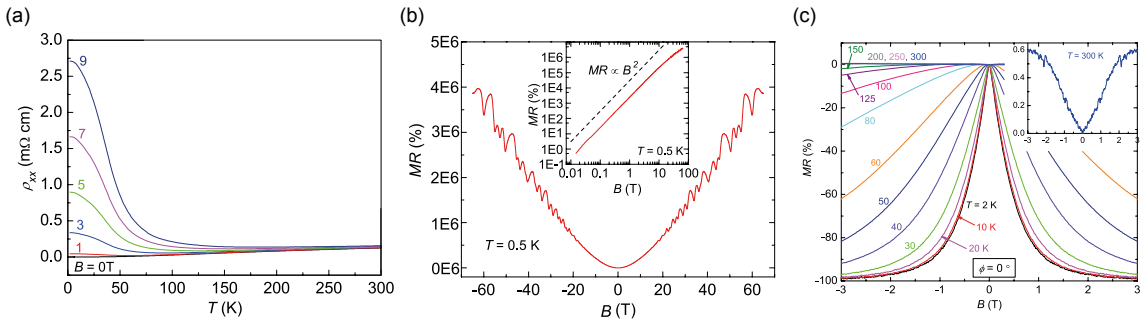


Figure 4.1: **Magnetotransport properties of $TaAs_2$.** (a) Temperature dependence of transverse resistivity for various applied magnetic fields (magnetic field and applied current direction are perpendicular). (b) Transverse magnetoresistance taken at temperature T =0.5 K. (c) Longitudinal magnetoresistance (magnetic field parallel to applied current) for various temperatures. Inset shows longitudinal magnetoresistance close to room temperature at T =300 K.

In the recently discovered Weyl semimetals, a negative longitudinal magnetoresistance is associated with the exotic *chiral anomaly*, which is caused due to charge pumping between two Weyl nodes in the presence of a parallel electric and magnetic field. However, the *chiral anomaly* is not the only possible origin of a negative magnetoresistance, which may also be caused by artifacts such as poor sample/contact geometry [98, 97]. The origin of the negative longitudinal magnetoresistance in the transition-metal dipnictides is currently still under debate, with some experimental groups suggesting an artificial origin by comparing different contact geometries [98], while others are proposing that there may be a magnetic field induced topological phase transition to a Weyl semimetal due to the Zeeman splitting of bands, which may cause the appearance of Weyl points [102], which are otherwise forbidden in the transition-metal dipnictide family due to the prensence of inversion and time-reversal symmetry in the absence of a magnetic field[5]. Another proposal hypothesizes a link between the unusual magnetoresistance and the weak topological phase that is predicted for the TmX family [100].

[5]Weyl points require the breaking of either time-reversal symmetry $\mathcal{T}$ or inversion symmetry $\mathcal{P}$, because if their product $\mathcal{T}*\mathcal{P}$ is conserved, then all bands must be doubly degenerate [84]. However, a Weyl point consists of the crossing of a single pair of bands, and can thus not be realized in a material where $\mathcal{T}*\mathcal{P}$ is conserved. A crossing of two doubly degenerate bands is called a Dirac point.

	$NbAs_2$	$TaAs_2$	$TaSb_2$
a	9.354	9.329	10.223
b	3.381	3.385	3.645
c	7.795	7.753	8.292
β	119.40	119.7	120.39

Table 4.1: **Experimental lattice parameters of the transition-metal dipnictides.** All compounds crystallize in a base-centered monoclinic structure. Values taken from Ref. [103].

4.2.2 Band structure calculations and weak topological phase in transition-metal dipnictides

The unusual magnetotransport properties reported above motivated a number of theoretical studies to investigate the bandstructure of the transition-metal dipnictides via *density functional theory* calculations. Here we will follow the most comprehensive discussion by Xu et al. [103].

All of the aforementioned compounds crystallize in the centrosymmetric base-centered monoclinic space group C12/m1 (number 12), with similar lattice parameters as shown in Table 4.1. As an example, we show the crystal structure of $TaSb_2$ in Figure 4.2(a), which also indicates two of the natural crystal facets occuring in the as-grown crystals, which can be used to cleave the crystal: the [0 0 1] surface, as well as the [1 1 1] surface[6]. We determined the position of the cleave along the two crystal directions by comparison of our surface state calculation with the experimental data, which will be discussed in more detail below. Note that this notation uses the primitive reciprocal lattice vectors (blue arrows in Figure 4.2(b)) to construct the miller indices of the surface normals. The resulting Brillouin zone of the lattice is shown in Figure 4.2(b), which indicated the positions of the high symmetry points that are used in the band structure calculations shown in Figure 4.2(c-e,1). From those band structure calculations, we can see that all of the dipnictides are semimetals with

[6] In fact, $TaSb_2$ also shows natural facets along the [1 0 0] and [0 1 1] directions, which can be used to cleave the crystal. However, although we managed to cleave the crystal along the [1 0 0] direction, we do not show the resulting ARPES data here, since it is of inferior quality and not necessary to determine the topological classification of $TaSb_2$.

substantial bulk density of states at the Fermi level. Furthermore, we can see that two bands are crossing the Fermi level, which form both electron and hole pockets. When replacing Nb by Ta and As by Sb, the spin-orbit induced splitting between conduction- and valence bands is increasing [103], as can be expected when substituting heavier elements. As a result, $TaSb_2$ has less electron pockets than $NbAs_2$ and $TaAs_2$, which can also be seen from the Fermi surfaces in Figures 4.2(c-e,2).

Due to the continuous energy gap between valence and conduction bands, it is possible to define and compute a $\mathbb{Z}_2$ topological index, even in the absence of a global energy gap, as we have seen in the previous chapter on LaBi. Xu et al. computed the $\mathbb{Z}_2$ index by calculating the parity eigenvalues of conduction and valence bands, which resulted in a topological index of (0; 1 1 1) for all transition-metal dipnictides. Thus, it can be expected that the these materials host a weak topological phase, with nontrivial topological surface states on all surfaces other than the dark surfaces defined by Equation (4.1). In the following, we will confirm this prediction for $TaSb_2$, and provide evidence that suggest that $NbAs_2$ and $TaAs_2$ are also topologically nontrivial.

4.3 ARPES study of transition-metal dipnictides, and discovery of a weak topological phase

As we have seen in the previous section, the transition metal dipnictides are predicted to host a weak topological phase, and are furthermore promising candidates to be cleaved on multiple surfaces. In this section, we will first present a comprehensive ARPES study of $TaSb_2$, which includes a measurement of both the dark surface without topological surface states, as well as a surface with topological surface states. Additionally, we will present evidence for topological surface states in $NbAs_2$ and $TaAs_2$, which shows that these compounds are topologically nontrivial, and most likely also host a weak topological phase.

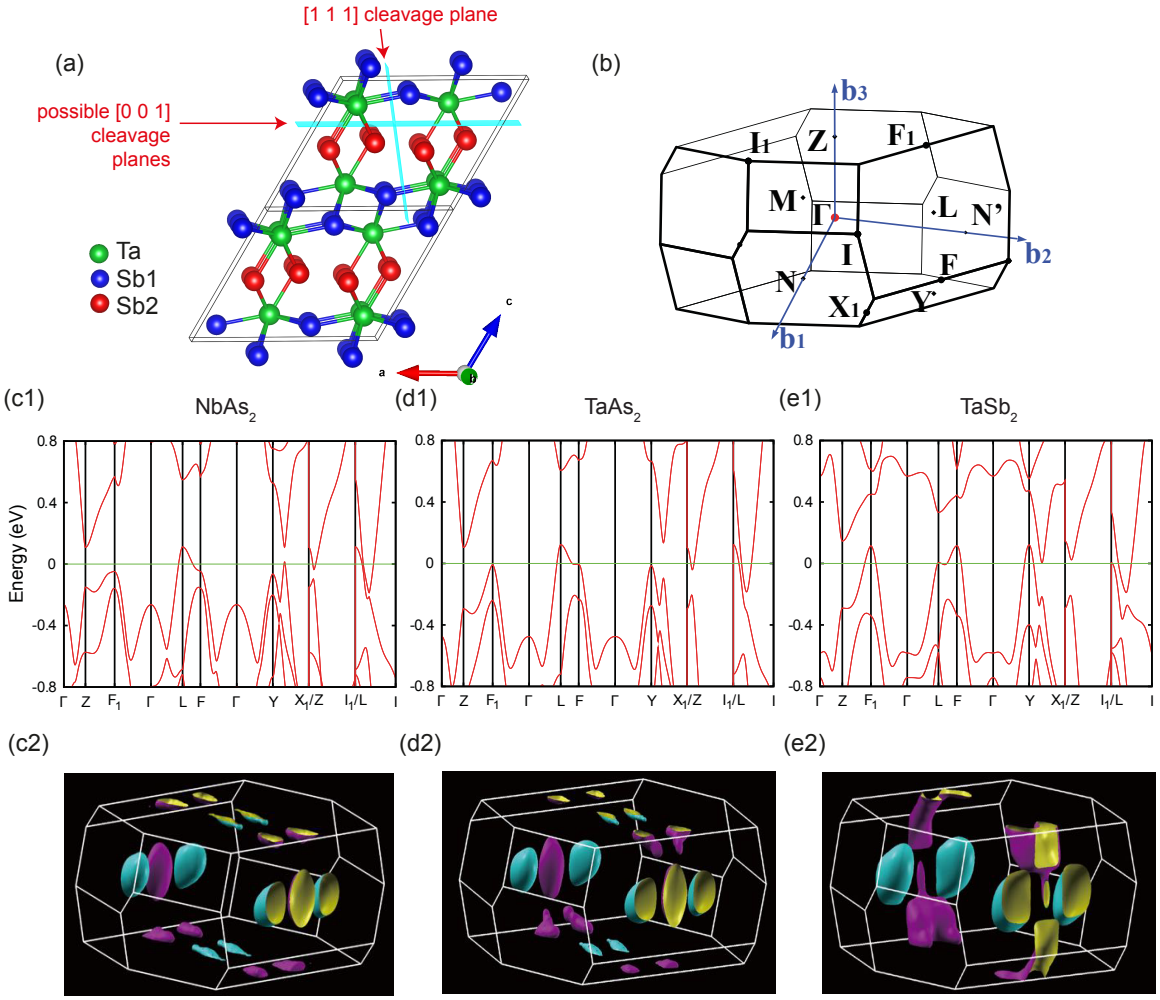


Figure 4.2: **Overview of the transition-metal dipnictide crystal- and band structure.** (a) Base-centered monoclinic crystal structure of $TaSb_2$, showing stack of two conventional unit cells. The blue planes and red arrows indicate possible cleavage planes in the [0 0 1] and [1 1 1] directions (reference: primitive reciprocal lattice vector). The red, blue and green arrow indicate the conventional lattice vector directions. The crystal structure was rendered with VESTA [108]. (b) Brillouin zone of base-centered monoclinic lattice, blue arrows indicate the primitive reciprocal lattice vectors, showing high-symmetry points. Adapted from Ref [103] (c-e,1) Band dispersions of the transition-metal dipnictides along the high-symmetry points shown in (b). Taken from Ref [103] (c-e,2) Resulting Fermi surfaces, with purple color indicating hole-pockets and cyan indicating electron pockets. Adapted from Ref [100].

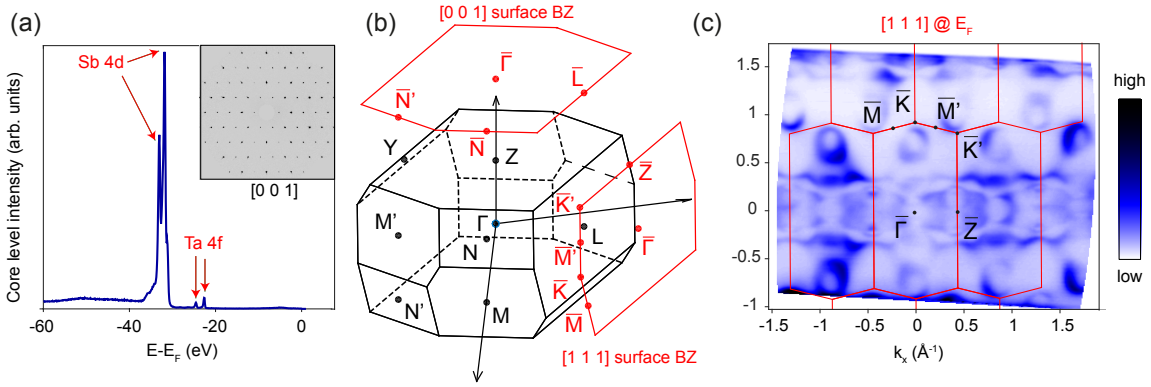


Figure 4.3: **Characterization of the $TaSb_2$ samples and identification of their measured cleavage planes.** (a) Core level spectrum of $TaSb_2$(taken with 100 eV photon energy). Red arrows indicating the characteristic antimony and tantalum core level peaks. The inset shows a reconstructed XRD pattern corresponding to a cut thorugh reciprocal space perpendicular to the [0 0 1] direction. (b) Bulk Brillouin zone, primitive reciprocal lattice vectors, and high symmetry points of $TaSb_2$ shown in black. Also shown in red are the [0 0 1] and [1 1 1] surface Brillouin zones and surface high symmetry points. (c) Fermi surfaces of a sample cleaved along the [1 1 1] direction (taken with hv=70 eV photon energy), indicating excellent agreement with the symmetry expected by the surface BZs (shown as red lines). The intensity modulation in different Brillouin zones is likely due to matrix element effects.

4.3.1 Discovery of a weak topological phase in $TaSb_2$

We begin the discussion of our experimental results by presenting some information about the sample characterization. Figure 4.3(a) displays the core level spectrum of one of our measured samples, which shows the characteristic antimony 4d and and tantalum 4f doublet peaks and therefore confirms the correct elemental composition of our samples. The inset of this Figure shows an reconstructed XRD pattern corresponding to a crossection through reciprocal space that is orthogonal to the [0 0 1] direction, which shows the expected "stretched" hexagonal symmetry of the [0 0 1] surface Brillouin zone. The XRD characetrization was also used to confirm the expected lattice constants of the samples, as well as to index their natural cleavage planes in order to correctly align the samples on the ARPES sample holders and to intentionally cleave them along certain directions. The expected surface Brillouin zones are shown as red lines in Figure 4.3(b), together with the bulk Brillouin zone

and reciprocal lattice vectors and high symmetry points. The surface BZs were used to confirm the correct cleavage planes in our ARPES data. Figure 4.3(c) shows a wide Fermi surface map whose symmtry is in excellent agreement with the expected [1 1 1] surface Brillouin zone, thus confirming the correct orientation of the cleavage plane and correct sample alignment.

Before discussing surface states in $TaSb_2$, we want to present ARPES measurements of the $TaSb_2$ bulk band structure in Figure 4.4 and compare it to bulk band structure calculations, which were provided by Dr Wujun Shi, Max-Planck Institute for Chemical Physics of Solids in Dresden, Germany. In almost all samples that we measured, the photoemission intensity is dominated by surface states, which makes it hard to extract the bulk band information. However, in one of the samples, by coincidence, the surface bands were suppressed, which may be due to some accidental contamination of the surface, similar to aged sample surfaces [104]. Alternatively, this sample may have been cleaved at elevated temperatures (when samples are cleaved too early after transfer onto the sample stage, the sample may not be cooled down yet), which can lead to an increased surface defect density and result in the suppression of surface states [105]. Figure 4.4(a) shows the predicted Fermi surface pocket structure for TaSb2, which shows both hole (red) and electron (blue) pockets. The blue planes are parallel to the [1 1 1] cleavage planes, so the k_z momentum will be perpendicular to these planes. Figure 4.4(b1) shows the experimental Fermi surface for this cleavage plane. Due to the limited escape depth of the electrons and the resulting k_z broadening, the Fermi surface shows band projections from various k_z values, which we simulated by plotting the Fermi surface for various k_z values, as shown in Figure 4.4(b2). Additionally, we also show the band dispersions and corresponding bulk band calculations in Figures 4.4(c,1-2) and 4.4(d,1-2) along the $\overline{\Gamma} - \overline{K}$ and $\overline{Z} - \overline{K'}$ directions, respectively. From the inspection of the Fermi surfaces and band dispersions, we can conclude that the experimental bulk band structure is overall in good agreement with the predicted bulk band structure. Specifically,

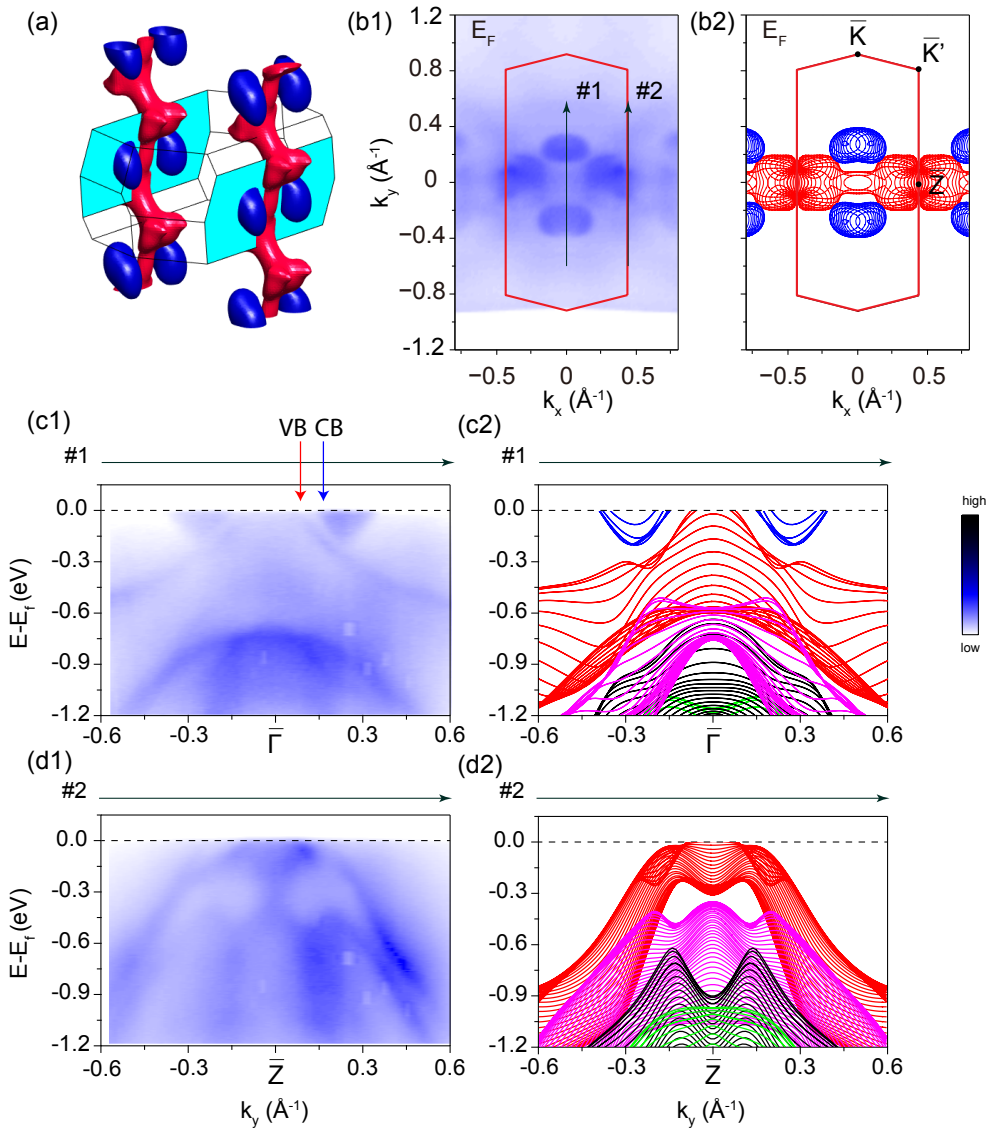


Figure 4.4: **Bulk band structure of $TaSb_2$.** (a) Overview of the predicted Fermi surface pockets in the three dimensional Brillouin zone (BZ), based on density-functional calculations. The hole pocket is indicated in red, and the electron pockets are shown in blue. The light blue side of the BZ indicates the planes perpendicular to the [1 1 1] direction. (b1) Experimental Fermi surface for the [1 1 1] surface (taken at hv=70 eV with linear-vertical polarization), the red solid lines indicate the surface Brillouin zone. (b2) Corresponding theoretical Fermi surface contours, calculated for 40 points between $k_z = [-\pi/d, \pi/d]$, where d is the layer spacing. The red lines indicate the hole bands, the blue lines the electron bands. (c,1-2) Experimental and theoretical band dispersions along the $\overline{\Gamma} - \overline{K}$ direction, which is also indicated by the black arrow #1 in (b1). The red and blue arrows indicate the boundaries of the hole pocket (valence band VB) and electron pocket (conduction band CB). The other colors (magenta, black and green) indicate the band dispersions of other bands not crossing E_F, plotted for different k_z values. Here, we show bands for 40 points between $k_z = [-\pi/d, \pi/d]$. (d,1-2) The same as (c,1-2), but for the $\overline{Z} - \overline{K'}$ direction, indicated by the black arrow #2 in (b1).

the electron and hole pockets are well separated (as is indicated by the blue and red arrows in Figure 4.4(c,1)), which is important for the definition of a weak topological phase that requires a continuous local gap between conduction and valence bands. Furthermore, the good agreement also lends credence to our subsequent surface band structure calculations, which are partially based on artificially created bulk slabs, and are thus related to the bulk calculations.

4.3.1.1 Dark [1 1 1] surface of $TaSb_2$

We will now turn our discussion to the surface state band structure of $TaSb_2$, and will begin by classifying the surface states of the [1 1 1] surface. Figure 4.5(a,i-ii) shows the Fermi surface of a typical $TaSb_2$ sample cleaved at the [1 1 1] surface measured with two photon energies, 55 eV, which shows the full Brillouin zone, and 24 eV, which shows only the center of the Brillouin zone with higher momentum resolution. Furthermore, a number of high symmetry points of the surface Brillouin zone are indicated. Note that only the $\overline{\Gamma}$, $\overline{M}$, $\overline{M}'$ and $\overline{Z}$ points are time-reversal invariant moments, but not $\overline{K}$ and $\overline{K}'$. In contrast to the previously inspected Fermi surface without surface states shown in Figure 4.4(b1), here we see that the bulk states are suppressed (although there are still some weak signatures of electron and hole pockets) and that there are additional surface states, which are indicated by red arrows. The most prominent surface state feature is a double hole pocket that is close to the $\overline{K}$ and $\overline{M}$ points of the Brillouin zone. To investigate whether these surface states are topological or trivial, we will now examine the number of surface crossings at the Fermi level between time-reversal invariant moments (TRIMs). From the band dispersions displayed in Figures 4.5(b, i-ii), we can see that there are two pairs of surface states that are crossing the Fermi level between $\overline{\Gamma} - \overline{K}$, which are at the same positions for measurements with 24 eV and 55 eV photons. We denote these bands as surface states, since they show no dispersion when measuring them with different photon energies, which corresponds to probing different k_z values, as is expected for

two-dimensional states confined to the sample surface. Furthermore, those bands also clearly appear in our slab surface state calculations[7], shown by red dots and red solid lines in Figure 4.5(b, iii), which were provided by Dr Wujun Shi, Max-Planck Institute for Chemical Physics of Solids in Dresden, Germany. Additionally, Figure 4.5(b, iii) also displays the bulk states for a range of k_z values (solid yellow lines) which simulates the k_z broadening of the bulk, and shows characteristic electron pockets that can also be seen in our experimental data.

After identifying these two surface state pairs, we can see from Figure 4.5(a,i-ii) that any path on the Fermi surface that is connecting the TRIMs $\overline{\Gamma}$, $\overline{M}$ will cross both surface state pairs at least once, but possibly also multiple times, thus leading to an overall even number of crossings. For instance, on a path from $\overline{\Gamma}$ to $\overline{K}$ to $\overline{M}$ (which is not a TRIM), there are 8 crossings along $\overline{\Gamma} - \overline{K}$ (initially crossing SS pair 2 once, and then crossing SS pair 1 three times), and from $\overline{K}$ to $\overline{M}$ there are no surface state crossings, which leads to an overall even number of SS crossings between $\overline{\Gamma}$ and $\overline{M}$. Hence, the product of the time-reversal polarizations discussed in the previous chapter about topological band theory must be $\pi(\overline{\Gamma})\pi(\overline{M}) = 1$. We now want to investigate the experimental band dispersion along $\overline{K}' - \overline{Z} - \overline{K}'$, which is shown in Figure 4.5(c,i-ii) for two photon energies (24 eV and 54 eV, respectively), and compare it to the slab band calculation and bulk band calculation in Figure 4.5(c,iii). The measurement at 55 eV shown in (c,ii) was taken with higher energy resolution an therefore allows to zoom in on the features near the Fermi level. We

[7]Density-functional theory (DFT) calculations were performed using the Vienna Ab-initio Simulation Package (VASP) with plane wave basis. The interactions between the valence electrons and ion cores were described by the projector augmented wave method . The exchange and correlation energy was formulated by the generalized gradient approximation with the Perdew-Burke-Ernzerhof scheme. The plane-wave basis cutoff energy was set to 300.0 eV. The Γ-centered k points were used for the first Brillouin-zone sampling with a spacing of 0.03 Å^{-1}. We used the experiment lattice constant (ICSD: 651600). In all the static calculations, the spin-orbit coupling were included. For the surface band structure calculations, a slab model was used as the structure for the DFT calculation. Ten unit cells were stacked along the (0 0 1) or (1 1 1) direction with 20 Å vacuum. The top and bottom 2 unit cells were freely relaxed until the maximum force on each atom was less than 5 meV/Å, while the other center atom were fixed as the bulk. The size of the red dots indicates the weight of the electronic states at the surface of the slab – larger dots correspond to surface states.

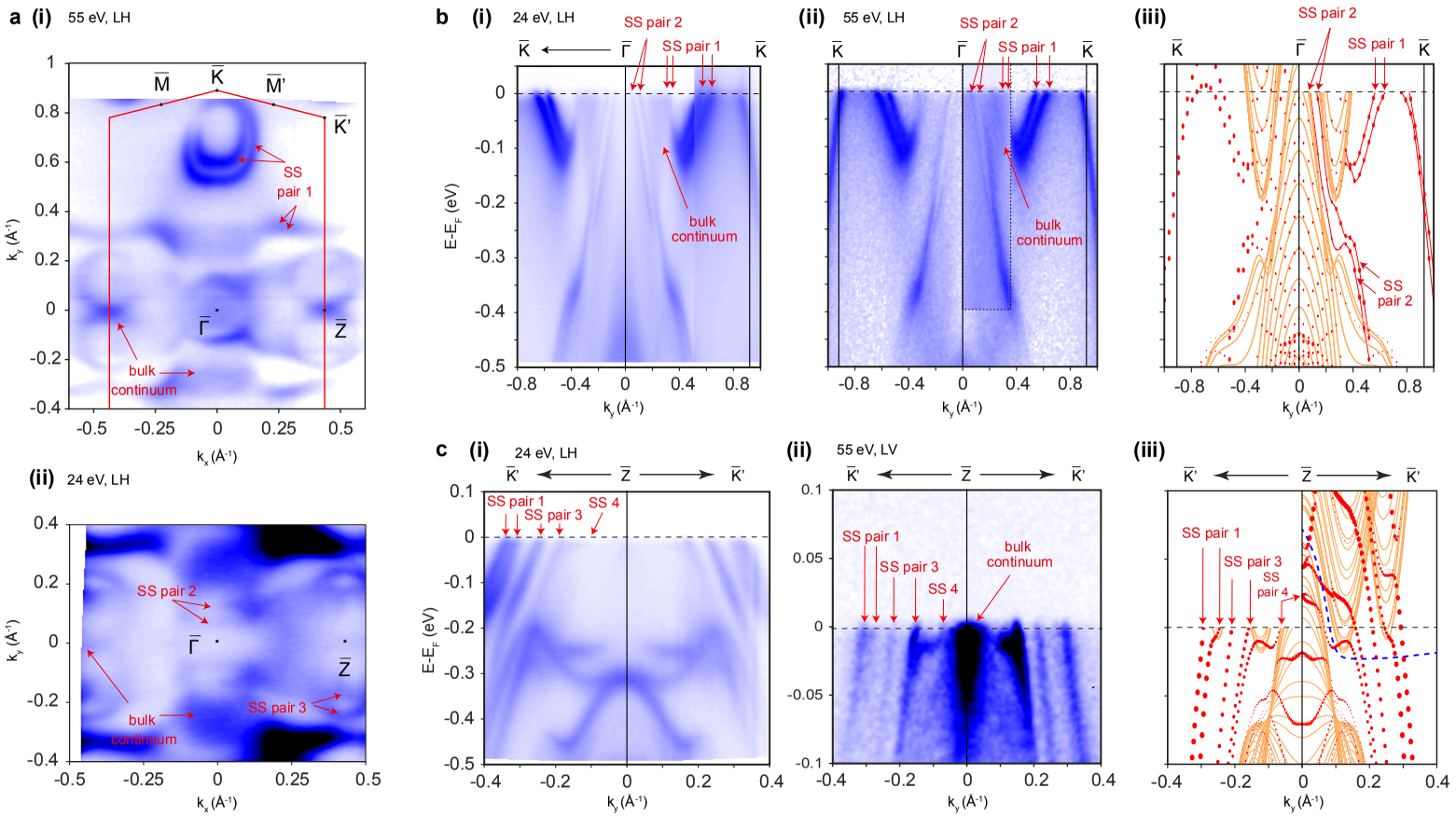


Figure 4.5: **Surface band structure of the dark [1 1 1] surface of $TaSb_2$.** (a) Fermi surface of the [1 1 1] cleavage plane taken with 55 eV photon energy and linear-horizontal (LH) polarization. The red arrows indicate pairs of surface states, as well as a continuum of bulk states forming an electron pocket between $\overline{\Gamma}$ and $\overline{K}$, as well as a hole pocket at $\overline{Z}$, which are smeared out due to the k_z broadening. The red solid line indicates the boundaries of the surface Brillouin zone. (b,i-ii) Experimental band dispersion along the $\overline{K} - \overline{\Gamma} - \overline{K}$ direction, taken with 24 eV and 55 eV photon energy and LH polarization, respectively. The inset in (b,ii) shows a spectrum taken with higher momentum resolution. Red arrows indicate two pairs of surface states, as well as a faint continuum of bulk states forming an electron pocket. (b,iii) Theoretical band dispersion of surface states (red dots and solid red line as guide to the eye) showing two pairs of trivial surface states, as well as continuum of bulk states for various k_z values (orange solid lines). (c,i-ii) Experimental band dispersion along the $\overline{K}' - \overline{Z} - \overline{K}'$ direction, taken with 24 eV and 55 eV photon energy and linear-horizontal (LH) and linear-vertical (LV) polarization, respectively. Red arrows indicate two pairs of surface states (SS pair 1 and SS pair 3), a single surface state (SS 4) as well as a faint continuum of bulk states near the Fermi level. (c,iii) Theoretical band dispersion of surface states (red dots and solid red line as guide to the eye) showing three pairs of trivial surface states, as well as continuum of bulk states for various k_z values (orange solid lines). The Fermi level in the bulk and surface state calculation was shifted to a higher energy by 100 meV. The dashed blue line indicates a hypothetical varying chemical potential that separates the bulk and valence bands, and crosses the surface states 8 times.

can see that the slab calculation is in excellent agreement with the experimental data after a rigid band shift of 100 meV, which may indicate intrinsic n-type doping of the sample. In the high energy resolution measurement in Figure 4.5(c,ii) we can identify five surface states that are crossing the Fermi level, and the comparison with the slab calculation shows that these are corresponding to three pairs of surface states (SS pair 1, SS pair 3, and SS pair 4) that are crossing the Fermi level. Due to the strong continuum of bulk states at the Fermi level in the vicinity of the $\overline{Z}$ point (which according to the bulk calculation should be hole-like), it is only possible to resolve one of the two bands that make up the SS pair 4. However, from the slab calculation, which shows excellent agreement with the resolvable surface bands, we can clearly see that the trivial SS pair 4 forms a Kramers point above the Fermi level at $\overline{Z}$, and that both surface states of this Kramers pair are dispersing towards the Fermi level in the vicinity of the $\overline{Z}$ point, and therefore must contribute an even number of crossings at the Fermi level. In other words, a perturbation may push this Kramers point below the Fermi level, such that both bands of surface state pair 4 would not cross it, which shows that it is topologically trivial. Alternatively, we can also imagine a locally varying chemical potential that is threaded through the local band gap (shown by the blue dashed line in Figure 4.5(c,iii)). We can see that the surface states in the slab calculation are crossing this line an even number of times. If a perturbation would now shift the bulk bands in a way that would open a global gap, the topological classification would not change, and therefore the number of crossings of surface states between conduction and valence bands would remain even. Since our bulk and surface state calculations are in excellent agreement with the experiment, we can conclude from this argument that there must be an even number of crossings of surface states between $\overline{Z} - \overline{K}'$. Since we can seen from the Fermi surface that there are no bands crossing between $\overline{M}' - \overline{K}'$, we can conclude that the number of crossings between $\overline{Z} - \overline{M}'$ (the other two TRIMs in the surface BZ besides $\overline{\Gamma}$ and $\overline{M}$) must also be even. We can thus conclude that $\pi(\overline{Z})\pi(\overline{M}') = 1$.

As a result, the overall product of the time-reversal invariant momenta of the [1 1 1] surface BZ is therefore $\pi(\overline{\Gamma})\pi(\overline{M})\pi(\overline{Z})\pi(\overline{M}') = 1$, thus $\upsilon_0 = 0$ (as we have discussed in the previous theory chapter), or in other words, $TaSb_2$ cannot be a strong topological insulator. Furthermore, since $\overline{M}$ and $\overline{M}'$ are symmetry equivalent, their time-reversal polarizations must be the same, i.e. $\pi(\overline{M}) = \pi(\overline{M}')$. Thus, from the above follows $\pi(\overline{\Gamma}) = \pi(\overline{M}) = \pi(\overline{Z}) = \pi(\overline{M}')$, and thus the [1 1 1] surface hosts no topological surface states. If we can show that $TaSb_2$ has nonzero weak indices, this implies that [1 1 1] is a *dark surface* of a weak TI with topological index (0; 1 1 1). In the following we will investigate the [0 0 1] surface of $TaSb_2$, and will show that its weak indices must indeed be nontrivial.

4.3.1.2 Topological [0 0 1] surface of $TaSb_2$

We will now turn to the analysis of our ARPES data of the [0 0 1] surface, which was obtained by aligning and cleaving the crystal along a plane that forms an angle of 82.9 degrees with respect to the [1 1 1] direction. Figure 4.6(a) displays the Fermi surface, which shows excellent agreement with the symmetry of the surface Brillouin zone boundaries shown as solid red lines, which is larger than the previously examined [1 1 1] surface BZ. Furthermore, the same figure also shows the high symmetry points $\overline{\Gamma}$, $\overline{N}$, $\overline{N}'$ and $\overline{L}$, which are all time-reversal invariant moments. We will now investigate the experimental band dispersion along the $\overline{N} - \overline{\Gamma} - \overline{N}$ direction, which is shown in Figure 4.6(b) and can be compared to the surface state calculation [8] 1in Figure 4.6(c), which was provided by Dr Wujun Shi, Max-Planck Institute for Chemical Physics of Solids in Dresden, Germany. This time, the surface states are not shown as red dots, but as solid red lines, and the bulk band continuum (i.e. the bulk bands for all values of k_z) is shown by solid red areas. The Fermi level in the calculation was again shifted by 100 meV in order to align the measured

[8] The surface states of semi-infinite model is calculated by the surface Green's function based on the tight binding model [109]. The image part of the surface Green's function is relative the local density of states from which we can obtain the surface states. The tight binding model parameters are constructed from the Wannier basis supplied by the Wannier90 code [110, 111].

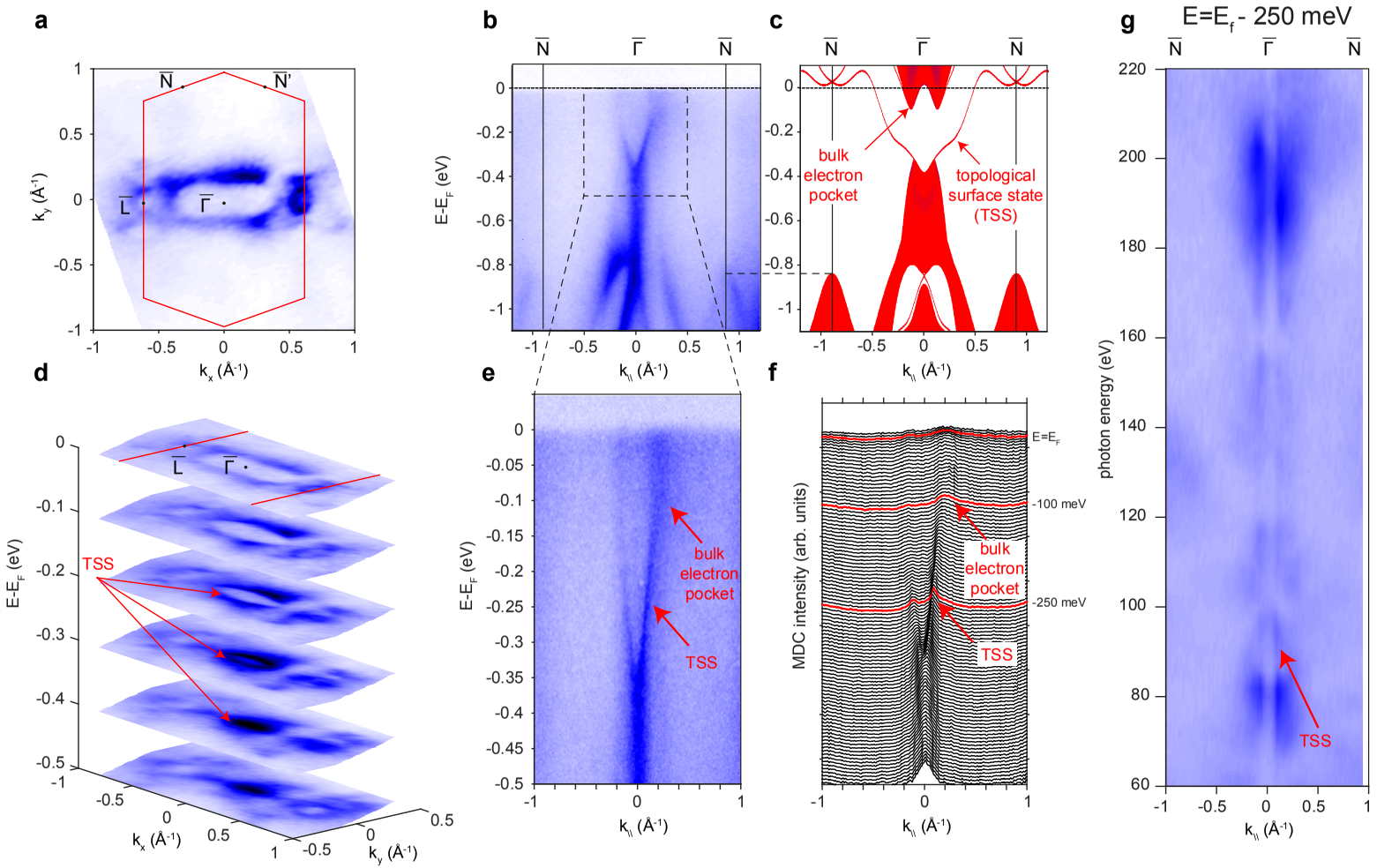


Figure 4.6: **Surface band structure of the topological [0 0 1] surface of $TaSb_2$.** (a) Fermi surface taken with photon energy of 80 eV. Red solid line indicates the surface Brillouin zone boundary of the [0 0 1] surface. (b) Experimental band dispersion along $\overline{N} - \overline{\Gamma} - \overline{N}$ the taken with a photon energy of hv=95 eV. (c) Surface state calculation, shifted by 100 meV to simulate electron doping. Solid areas indicate bulk regions, sharp solid line indicates surface states. (d) Equal energy surfaces, taken with hv=80 eV. Red arrows indicate the position of the topological surface state (TSS). (e) High energy resolution measurement, taken at hv=95 eV. Red arrows indicate the position of the bulk band pocket and the surface state. (f) Momentum distribution curve (MDC) of the data shown in (e), indicating a broad peak close to the Fermi level that corresponds to the bulk pocket due to k_z broadening, and the sharp peak of the TSS at higher binding energies. (g) Photon energy dependent dispersion of the bands along $\overline{N} - \overline{\Gamma} - \overline{N}$ at binding energy of $E_b = 250$ meV. Vertical line indicates two-dimensional surface state.

valence band top with the calculated valence band top at the $\overline{N}$ point (as indicated by the black horizontal dashed line between Figures b and c), which may indicate intrinsic n-type doping. The calculation predicts two electron pockets (indicated by red arrows) above a projected band gap (~300 meV) in the vicinity of the $\overline{\Gamma}$ point, which is bridged by a single surface state band that is crossing the Fermi level once between the TRIMs $\overline{\Gamma} - \overline{N}$. Indeed, the measured spectrum shows a sharp and linearly dispersing band along $\overline{\Gamma} - \overline{N}$ in the region between $150 - 350$ meV binding energy, which appears to form a circular equal energy contours in this energy range, as can be seen from the equal energy surfaces shown in Figure 4.6(d). The high energy resolution dispersion displayed in 4.6(e) and corresponding momentum distribution curves (MDCs) qualitatively confirm the prediction of the calculation. In the energy region of $0 - 100$ meV, there is a broad feature which corresponds to the predicted electron pocket that is broadened due to k_z broadening. At higher binding energies, a much sharper features emerges up to about 350 meV, which corresponds to the predicted surface state, which merges into the electron pocket close to the Fermi level. The surface state calculation presented here does therefore not perfectly describe the Fermi energy momentum (the Fermi surface wave vector is larger than in the experiment). However, such small quantitative deviations between ab-initio calculations and experimentally determined band dispersions are common, and may be due to an insufficient description of electron-electron interactions by the exchange correlation functional, or a small reconstruction of the atoms at the Fermi surface that may not be included in the model. Nevertheless, the surface state calculations presented here give a very good qualitative description of the band structure, and the identification of the surface state can further be corroborated by our photon energy dependent measurement of the band dispersion along $\overline{N} - \overline{\Gamma} - \overline{N}$, which is shown for a binding energy of 250 meV in Figure 4.6(g). As expected for a two-dimensional surface state, when changing the photon energy (i.e. effectively tuning k_z), the surface state bands do not disperse. The intensity modulation observed in Figure 4.6(g) is

most likely due to a change of the photoionization crosssection with photon energy, but does not constitute a periodic band dispersion along k_z. Thus, we can conclude that the there is a single surface state crossing between the TRIMs $\overline{\Gamma}$ and $\overline{N}$ (thus $\pi(\overline{\Gamma})\pi(\overline{N}) = -1$), but since our analysis of the [1 1 1] surface has shown that the strong index of $TaSb_2$ must be trivial $v_0 = 0$, this implies that the weak indices of $TaSb_2$must be nontrivial, and since the dark surface is on the [1 1 1] plane, this means that its topological index must be (0; 1 1 1), consistant with the theory prediction. This finding establishes $TaSb_2$ as the first material where a weak topological phase has been conclusively established by measuring the surface states on two nonequivalent surfaces. In the previous theory chapter, we have learned that $v_0 = 0$ implies $\pi(\overline{\Gamma})\pi(\overline{N})\pi(\overline{N}')\pi(\overline{L}) = 1$, and thus $\pi(\overline{\Gamma})\pi(\overline{L}) = 1$ (due to the symmetry equivalence $\pi(\overline{N}) = \pi(\overline{N}')$), but $\pi(\overline{N}')\pi(\overline{L}) = -1$. Thus, we would expect an even number of surface state crossings between $\overline{\Gamma}$ and $\overline{L}$, and an odd number of surface state crossings between $\overline{N}$ and $\overline{L}$. However, due to the strong contribution of bulk bands at the $\overline{L}$ point, we were not yet able to clearly confirm this prediction[9].

4.3.2 Potential topological surface states in $TaAs_2$ and $NbAs_2$

After establishing a weak topological phase in $TaSb_2$, we now want to present preliminary evidence that $TaAs_2$ and $NbAs_2$ are also topologically nontrivial. Identifying the topological surface states in both of these compounds is more challenging than in $TaSb_2$, since they are predicted to have a much small band gap at the Z-point (which can be seen in Figures 4.2(c-d)) which leads to a much smaller projected band gap along the $\overline{\Gamma} - \overline{N}$ direction on the [0 0 1] surface. In Figure 4.7(a) we present the experimental Fermi surface of $TaAs_2$, which agrees well with the symmetry of the [0 0 1] surface Brillouin zone boundary that is shown as a solid red line. We can see that the slit of the detector is slightly misaligned with the $\overline{R} - \overline{\Gamma} - \overline{R}$ direction,

[9] In fact, we obtained some data for the [0 0 1] surface that seems to indicate an even number of crossings between $\overline{\Gamma}$ and $\overline{L}$. However, the obtained data lacked sufficient momentum resolution and was not yet reproduced, and will therefore not be shown here.

but this should introduce only a small error in the subsequent analysis of the band dispersions. Figure 4.7(b) shows the band dispersion along the $k_x = 0$ line, which corresponds approximately to the $\overline{R} - \overline{\Gamma} - \overline{R}$ direction. We can see that there is a single band crossing at the Fermi level along $\overline{\Gamma} - \overline{R}$, indicated by a blue arrow. We suspect this band is a surface state similar to the one that we investigated in $TaSb_2$, and since there is no band crossing at the Fermi level between $\overline{N} - \overline{R}$, this would imply that there is an odd number of surface state crossings between the TRIMs $\overline{\Gamma}$ and $\overline{N}$, and that $TaAs_2$ is also topologically nontrivial. By comparison with the bulk band calculations shown in Figures 4.2(d) we can see that there should be a bulk electron pocket at the Fermi level along $\overline{\Gamma} - \overline{R}$ with a projected band gap underneath at slightly higher binding energies between 50-200 meV. We can see that the band that is crossing the Fermi level is extending into this projected bulk band gap (highlighted by a red arrow), which indicates its surface origin. In Figures 4.2(c,1-2) we show the photon energy dependence for this band at the Fermi level, and at binding energy $E_B = 200$ meV in the predicted projected band gap. Both plots indicate that the band that is crossing the Fermi level is nondispersive along k_z, which is the hallmark of a surface state. The intensity modulation at the Fermi level with photon energy may be due to the dispersion of the bulk electron pocket, or crosssection effects. Figure 4.2(d) shows the existence of a similar two dimensional state at the Fermi level of $NbAs_2$ (which may again co-exist with a bulk electron pocket), which suggests a similar topological classification as $TaAs_2$ and $TaSb_2$. However, the small projected band gap at higher binding energies (between 0.05 - 0.1 eV according to Figures 4.2(d)) along the $\overline{R} - \overline{\Gamma} - \overline{R}$ direction makes it challenging to distinguish bulk and surface states in the existing data on $NbAs_2$. Future experiments should therefore either measure this surface state with much higher energy resolution, or employ a different strategy to unambiguously determine the topological classification of $NbAs_2$, which will be discussed in detail below.

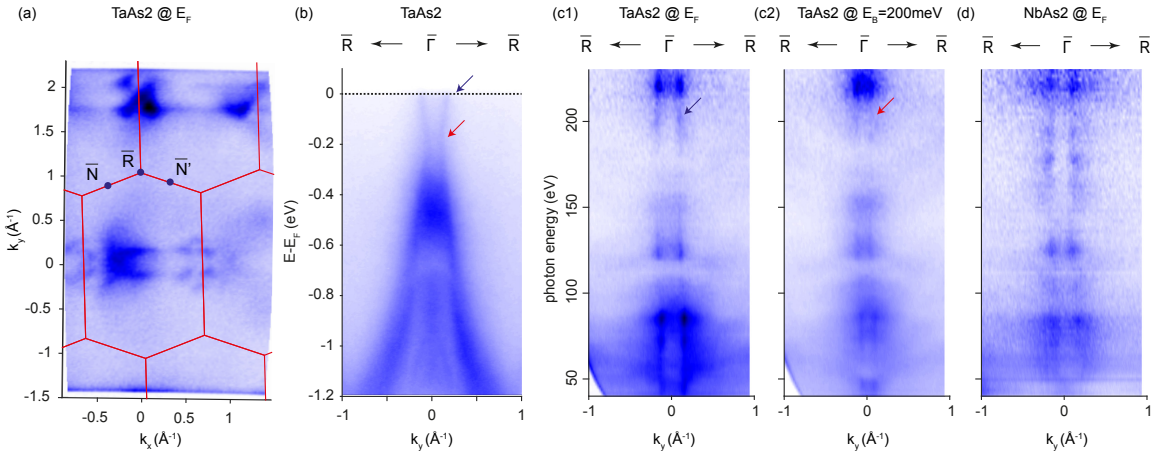


Figure 4.7: **Potential topological surface states in $TaAs_2$ and $NbAs_2$.** (a) Fermi surface of $TaAs_2$, red lines indicate the [0 0 1] surface Brillouin zone. Taken with photon energy hv=124 eV. (b) Band dispersion of $TaAs_2$ along the $k_x = 0$ direction, which approximately corresponds to the $\overline{R} - \overline{\Gamma} - \overline{R}$ direction. Taken with photon energy hv=124 eV. The blue arrow indicates a Fermi level crossing of a potential surface state, while the red arrow indicates that this surface state extends into the projected band gap. (c,1-2) Photon energy dependence of the potential surface state of $TaAs_2$ at the Fermi level, and at binding energy 200 meV, respectively. Red and blue arrows correspond to the arrows in (b). (d) Photon energy dependence of potential surface states in of $NbAs_2$. All data was taken with linear-horizontal polarization.

4.4 Discussion of the results and perspectives for future research

Before starting out discussion, let us briefly summarize the results presented above. We have shown that

1. The [1 1 1] surface of $TaSb_2$ hosts only trivial surface states that cross the Fermi level an even number of times between time-reversal invariant momenta (TRIMs). In contrast, the [0 0 1] surface of $TaSb_2$hosts a topological surface state that crosses an odd number of times between TRIMs. Thus, $TaSb_2$must be a weak topological semimetal with topological index (0; 1 1 1).

2. There is a single band crossing of a potential surface state along the $\overline{\Gamma} - \overline{R}$ direction of the [0 0 1] surface of $TaAs_2$ and $NbAs_2$, which suggests that they are also topologically nontrivial. Due to their similarity to $TaSb_2$ and the predictions made by ab-initio calculations, it seems intuitive that they should have the same topological index (0; 1 1 1).

Both of these results can be seen as the starting point for further investigations. As we have learned from the literature review in the beginning of the chapter, what distinguishes $TaSb_2$ from all previously investigated weak TI materials is that it can be cleaved on different nonequivalent surfaces, which allowed us to measure its trivial and topological surface states with momentum resolution and thus unambiguously confirm the weak topological phase. Topological surface states have been linked to exotic transport phenomena in Dirac- and Weyl semimetals (e.g. [112, 113]), and it will be interesting to see whether the weak topological phase may also be related to the exotic magnetotransport in $TaSb_2$, such as the negative longitudinal magnetoresistance that was discussed above. However, to utilize the potential of a weak topological insulator, such as spin-polarized edge states at step edges of the dark surface, it will most likely be necessary to try to introduce a global band gap

to localize the trivial bulk states and thus separate them from edge currents. From the previously discussed ab-initio calculations shown in Figures 4.2(c-e), we can see that increasing the strength of spin-orbit coupling by doping with heavier elements can reduce the number of bulk pockets and introduce local band gaps. It would be interesting to see whether further doping with even heavier elements, such as Bismuth for Antimony, may remove the remaining pockets and thus introduce a global gap. Furthermore, it was shown that for β-Bi_4I_4, strain can close and re-open a global gap and thus induce a topological phase transition [89], which may be a possible route to engineer a global gap in $TaSb_2$ as well, either by thin film deposition or external application of strain [106].

After establishing $TaSb_2$ as a weak topological semimetal, it becomes an interesting question to ask whether other materials in the same family also share the same topological properties, as was predicted by ab-initio calculations. Our investigation of $TaAs_2$ and $NbAs_2$ have shown that it is more challenging to identify their putative topological surface states on the [0 0 1] surface due to smaller projected bulk band gaps. An alternative route to measure the crossings of topological surface states would be to cleave the crystal along the [1 0 0] or [1 0 1] surfaces (nomenclature according to the primitive lattice vectors as defined in Figure 4.3(a)). These surfaces are almost orthogonal to both [0 0 1] and [1 1 1] surfaces and would thus allow to access the vicinity of the $\overline{\Gamma}$ point without overlapping bulk pockets at the Fermi level, which would make it easier to identify surface states and count their number of Fermi level crossings. This strategy seems plausible since we have already managed to cleave $TaSb_2$ along the [1 0 0] surface (data not shown here), and since $TaAs_2$ grows with large exposed [1 0 0] facets.

Finally, we would like to conclude our discussion by noting that it seems a strange coincidence that many of the previously discussed weak TI candidates (β-Bi_4I_4, β-Bi_4Br_4, and Bi_2TeI) are crystallizing in the same space group 12 as the transition-metal dipnictides and have similar ratios of lattice constants. This observation leads

us to speculate that a high-throughput search of cataloged materials from this space group with similar lattice parameter ratios and heavy elements with large spin-orbit coupling may yield more weak TI candidates. If this search turns out to be successful, it would be interesting to investigate why this space group seems to be suitable to host weak TIs.

References

[81] Yoichi Ando. Topological insulator materials. *Journal of the Physical Society of Japan*, **82**(10):102001, 2013.

[82] Liang Fu and Charles L Kane. Topological insulators with inversion symmetry. *Physical Review B*, **76**(4):045302, 2007.

[83] Zohar Ringel, Yaacov E Kraus, and Ady Stern. Strong side of weak topological insulators. *Physical Review B*, **86**(4):045102, 2012.

[84] M Zahid Hasan and Charles L Kane. Colloquium: topological insulators. *Reviews of Modern Physics*, **82**(4):3045, 2010.

[85] Roger SK Mong, Jens H Bardarson, and Joel E Moore. Quantum transport and two-parameter scaling at the surface of a weak topological insulator. *Physical Review Letters*, **108**(7):076804, 2012.

[86] Ying Ran, Yi Zhang, and Ashvin Vishwanath. One-dimensional topologically protected modes in topological insulators with lattice dislocations. *Nature Physics*, **5**(4):298, 2009.

[87] Yukinori Yoshimura, Akihiko Matsumoto, Yositake Takane, and Ken-Ichiro Imura. Perfectly conducting channel on the dark surface of weak topological insulators. *Physical Review B*, **88**(4):045408, 2013.

[88] Gabriel Autes, Anna Isaeva, Luca Moreschini, Jens C. Johannsen, Andrea Pisoni, Ryo Mori, Wentao Zhang, Taisia G. Filatova, Alexey N. Kuznetsov, Laszlo Forro, Wouter Van den Broek, Yeongkwan Kim, Keun Su Kim, Alessandra Lanzara, Jonathan D. Denlinger, Eli Rotenberg, Aaron Bostwick, Marco Grioni, and Oleg V. Yazyev. A novel quasi-one-dimensional topological insulator in bismuth iodide β-Bi4I4. *Nature Materials*, **15**(2):154–158, 2016.

[89] Cheng-Cheng Liu, Jin-Jian Zhou, Yugui Yao, and Fan Zhang. Weak topological insulators and composite Weyl semimetals: β- Bi 4 X 4 (X= Br, I). *Physical Review Letters*, **116**(6):066801, 2016.

[90] B Rasche, A Isaeva, M Ruck, S Borisenko, V Zabolotnyy, B Büchner, K Koepernik, C Ortix, M Richter, and J van den Brink. Stacked topological insulator built from bismuth-based graphene sheet analogues. *Nature Materials*, **12**(5):422–425, 2013.

[91] Christian Pauly, Bertold Rasche, Klaus Koepernik, Marcus Liebmann, Marco Pratzer, Manuel Richter, Jens Kellner, Markus Eschbach, Bernhard Kaufmann, Lukasz Plucinski, Claus M. Schneider, Michael Ruck, Jeroen van den Brink, and Markus Morgenstern. Subnanometre-wide electron channels protected by topology. *Nature Physics*, **11**(4):338–343, 2015.

[92] Markus Eschbach, Martin Lanius, Chengwang Niu, Ewa Mlynczak, Pika Gospodaric, Jens Kellner, Peter Schüffelgen, Mathias Gehlmann, Sven Doering, Elmar Neumann, Martina Luysberg, Gregor Mussler, Lukasz Plucinski, Markus Morgenstern, Detlev Gruetzmacher, Gustav Bihlmayer, Stefan BlÃŒgel, and Claus M. Schneider. Bi1Te1 is a dual topological insulator. *Nature Communications*, **8**:14976, 2017.

[93] Nurit Avraham, Andrew Norris, Yan Sun, Yanpeng Qi, Lin Pan, Anna Isaeva, Alexander Zeugner, Claudia Felser, Binghai Yan, and Haim Beidenkopf. Coexisting surface states in the weak and crystalline topological insulator Bi2TeI. *arXiv preprint arXiv:1708.09062*, 2017.

[94] IP Rusinov, TV Menshchikova, A Isaeva, SV Eremeev, Yu M Koroteev, MG Vergniory, PM Echenique, and EV Chulkov. Mirror-symmetry protected non-TRIM surface state in the weak topological insulator Bi2TeI. *Scientific reports*, **6**:20734, 2016.

[95] Peizhe Tang, Binghai Yan, Wendong Cao, Shu Chun Wu, Claudia Felser, and Wenhui Duan. Weak topological insulators induced by the interlayer coupling: A first-principles study of stacked Bi 2 TeI. *Physical Review B*, **89**(4):1–5, 2014.

[96] Yongkang Luo, R. D. McDonald, P. F. S. Rosa, B. Scott, N. Wakeham, N. J. Ghimire, E. D. Bauer, J. D. Thompson, and F. Ronning. Anomalous electronic structure and magnetoresistance in TaAs2. *Scientific Reports*, **6**(April):27294, 2016.

[97] Bing Shen, Xiaoyu Deng, Gabriel Kotliar, and Ni Ni. Fermi surface topology and negative longitudinal magnetoresistance observed in the semimetal NbAs2. *Physical Review B*, **93**(19):1–6, 2016.

[98] Zhujun Yuan, Hong Lu, Yongjie Liu, Junfeng Wang, and Shuang Jia. Large magnetoresistance in compensated semimetals TaAs2 and NbAs2. *Physical Review B*, **93**(18):1–12, 2016.

[99] Desheng Wu, Jian Liao, Wei Yi, Xia Wang, Peigang Li, Hongming Weng, Youguo Shi, Yongqing Li, Jianlin Luo, Xi Dai, and Zhong Fang. Giant semiclassical magnetoresistance in high mobility TaAs2 semimetal. *Applied Physics Letters*, **108**(4), 2016.

[100] Yupeng Li, Zhen Wang, Yunhao Lu, Xiaojun Yang, Zhixuan Shen, Feng Sheng, Chunmu Feng, Yi Zheng, and Zhu-An Xu. Negative Magnetoresistance in Topological Semimetals of Transition-Metal Dipnictides with Nontrivial Z2 Indices. *ArXiv e-prints*, pages 1–8, 2016.

[101] Zheng Wang, Yupeng Li, Yunhao Lu, Zhixuan Shen, Feng Sheng, Chunmu Feng, Yi Zheng, and Zhuan Xu. Topological phase transition induced extreme magnetoresistance in $TaSb_2$. *ArXiv e-prints*, 2016.

[102] Dominik Gresch, Quansheng Wu, Georg W. Winkler, and Alexey A. Soluyanov. Hidden Weyl points in centrosymmetric paramagnetic metals. *New Journal of Physics*, **19**(3):1–11, 2017.

[103] Chenchao Xu, Jia Chen, Guo Xiang Zhi, Yuke Li, Jianhui Dai, and Chao Cao. Electronic structures of transition metal dipnictides XPn2 (X=Ta, Nb; Pn= P, As, Sb). *Physical Review B*, **93**(19):1–6, 2016.

[104] S. C. Wang, H. B. Yang, A. K P Sekharan, H. Ding, J. R. Engelbrecht, X. Dai, Z. Wang, A. Kaminski, T. Valla, T. Kidd, A. V. Fedorov, and P. D. Johnson. Quasiparticle line shape of Sr 2RuO 4 and its relation to anisotropic transport. *Physical Review Letters*, **92**(13):0–4, 2004.

[105] Y Pennec, N J C Ingle, I S Elfimov, E Varene, Y Maeno, A Damascelli, and J V Barth. Cleaving-Temperature Dependence of Layered-Oxide Surfaces. *Phys. Rev. Lett.*, **101**(21):216103, nov 2008.

[106] Clifford W. Hicks, Mark E. Barber, Stephen D. Edkins, Daniel O. Brodsky, and Andrew P. Mackenzie. Piezoelectric-based apparatus for strain tuning. *Review of Scientific Instruments*, **85**(6):0–8, 2014.

[107] Yoichi Ando and Liang Fu. Topological Crystalline Insulators and Topological Superconductors : From Concepts to Materials. *Annual Review of Condensed Matter Physics*, **6**:361–81, 2015.

[108] K. Momma and F. Izumi. VESTA 3 for three-dimensional visualization of crystal, volumetric and morphology data. *Journal for Applied Crystallography*, **44**:1272–1276, 2011.

[109] MP Lopez Sancho, JM Lopez Sancho, JM Lopez Sancho, and J Rubio. Highly convergent schemes for the calculation of bulk and surface Green functions. *Journal of Physics F: Metal Physics*, **15**(4):851, 1985.

[110] Ivo Souza, Nicola Marzari, and David Vanderbilt. Maximally localized Wannier functions for entangled energy bands. *Physical Review B*, **65**(3):035109, 2001.

[111] Arash A Mostofi, Jonathan R Yates, Young-Su Lee, Ivo Souza, David Vanderbilt, and Nicola Marzari. wannier90: A tool for obtaining maximally-localised Wannier functions. *Computer physics communications*, **178**(9):685–699, 2008.

[112] Tian Liang, Quinn Gibson, Mazhar N Ali, Minhao Liu, RJ Cava, and NP Ong. Ultrahigh mobility and giant magnetoresistance in the Dirac semimetal Cd3As2. *Nature Materials*, **14**(3):280–284, 2015.

[113] Chandra Shekhar, Ajaya K. Nayak, Yan Sun, Marcus Schmidt, Michael Nicklas, Inge Leermakers, Uli Zeitler, Yurii Skourski, Jochen Wosnitza, Zhongkai Liu, Yulin Chen, Walter Schnelle, Horst Borrmann, Yuri Grin, Claudia Felser, and Binghai Yan. Extremely large magnetoresistance and ultrahigh mobility in the topological Weyl semimetal candidate NbP. *Nature Physics*, **11**(8):645–649, 2015.

[114] N. B. M. Schröter, J. Jiang, W. Shi, F de Juan, Y. F. Guo, L. X. Yang, C. Cheng, H. Peng, S. A. Ekahana, Y. Li, B. H. Yan, C. Felser, and Y. L. Chen. Discovery of a weak topological phase in a semimetal. (to be submitted).

Chapter 5

Discovery of Dirac-like bands in the monolayer limit of ultrathin Ge films on Au(111)

In this chapter, we will present our ARPES study of ultrathin Ge films grown epitaxially on Au(111), which was recently published in Ref. [116]. We will begin with with an introduction to describe our motivation to grow these films, as well as a brief review of previous theoretical and experimental investigations. Subsequently, we will describe the growth and characterization of films with various thicknesses, and show how their electronic structure evolves when tuning the layer thickness. By varying the polarization of the incident photon polarization, we are able to unmask multiple previously unreported conical bands that could originate from rotationally disordered germanene, a honeycomb lattice made of Ge atoms and 2D topological insulator candidate. The films presented here were grown and measured by the author with the support of the coauthors in Ref. [116]. All of the ARPES and STM data analysis was conducted by the author, and the analysis of the data presented in Figure 5.2 was supported by Matthew Watson.

5.1 Background and previous experiments on graphene analogues with strong spin-orbit coupling

In our previous discussion of the weak topological insulator candidate $Bi_{14}Rh_3I_9$ we noticed that there is a similarity of the 2D topological insulator stacking layers and graphene, which is a two-dimensional honeycomb structure made out of carbon atoms that host two-dimensional Dirac points[1] at the K/K' points of its Brillouin zone [117]. Indeed, graphene was the first proposed 2D topological insulator [118] with a spin-orbit coupling (SOC) induced gap at the Dirac points, which is bridged by spin-polarized edge states that are protected from backscattering by nonmagnetic impurities and may thus become relevant for device applications [119, 120]. However, since carbon is a relatively light element, SOC is weak and the resulting gap - which was predicted to be on the order of ~μeV [121] - was never reliably detected experimentally. The first realization of a 2D topological insulator was made in quantum well structure of HgTe/CdTe layers [122], which have a bulk band gap of typically only ~10 meV, which limits the use of potential devices to very low temperatures that are needed to suppress the thermal population of trivial conduction band states. An intriguing proposal to increase the band gap is to replace the carbon atoms in graphene with heavier elements, such as Si, Ge, or Sn, which were predicted to form stable but buckled honeycomb structures called silicene, germanene, and stanene, which host massive Dirac cones with band gaps of ~2 meV [123], ~24 meV [123], and ~100 meV [124] (see Figures 5.1(a-c)), respectively. Due to their much larger band gaps, devices based on germanene or stanene may thus allow operation at temperatures close to room temperature. Furthermore, decoration of these honeycomb structures with halogen atoms such as iodine could induce an even more exotic effect, the quantum anomalous Hall effect, which can realize a quantum Hall state in the

[1] The doubly degenerate band crossing that leads to a linear dispersion in its vicinity is conventionally called Dirac point with reference to the Dirac Hamiltonian of a massless paticle with dispersion relation $E(\boldsymbol{k}) = \hbar v_F \boldsymbol{k}$, where v_F is a velocity. If the Hamiltonian acquires a mass term m, the dispersion relation becomes gapped $E(\boldsymbol{k}) = \pm\sqrt{(\hbar v_F \boldsymbol{k})^2 + m^2}$ [115].

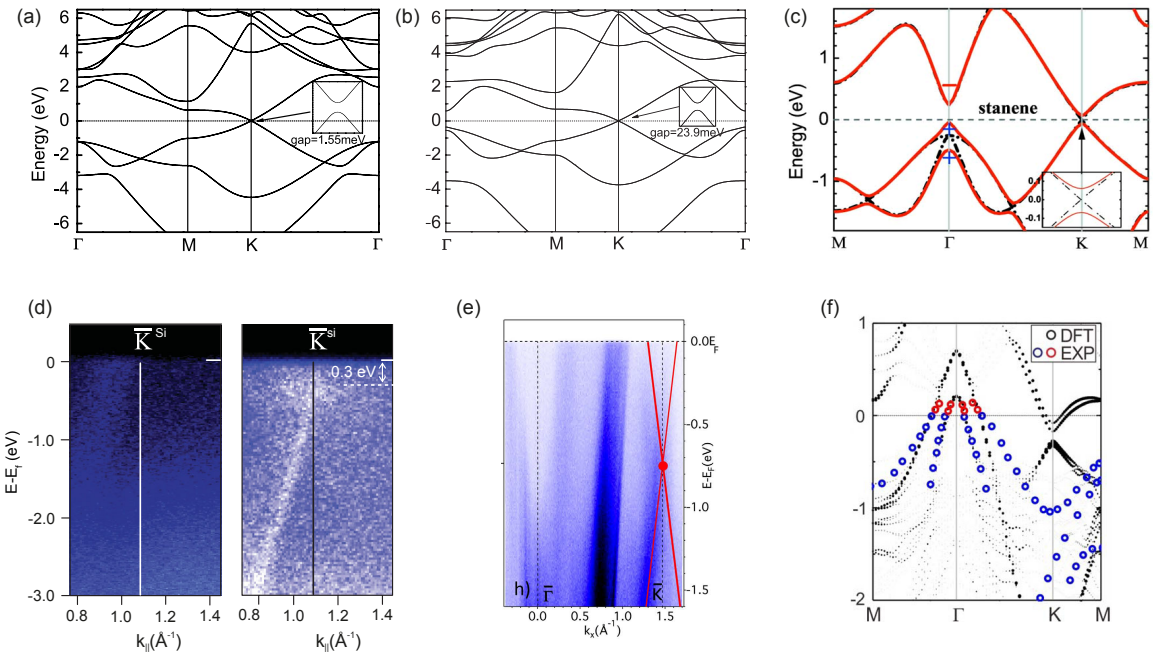


Figure 5.1: **Previous theoretical and experimental studies of silicene, germanene, and stanene.** (a-c) Band structure calculation of bulked honeycomb lattices made out of Si, Ge, Sn. Inset shows gapped Dirac cone and indicates the size of the gap. Taken from Refs. [123, 124]. (d) Experimental band dispersion of Si grown on Ag(1 1 1). Taken from Ref. [125] (e) Experimental band dispersion of Ge grown on Au(1 1 1). Taken from Ref. [126] (f) Experimental band dispersion of Sn grown on Bi_2Te_3(blue and red circles), compared to calculations (black circles). Taken from Ref. [127].

absence of a magnetic field [151]. However, unlike for graphene, there is no natural parent compound like graphite from which silicene, germanene, and stanene can be peeled off, but instead they need to be grown on a substrate.

For the cases of silicene and stanene, there have been growth attempts on various insulating and metal substrates, as well as ARPES studies. Initial reports claimed the existence of Dirac cones in silicene grown on Ag(111) [125], supported by ARPES measurements that showed a single linearly dispersing band (reproduced in Figure 5.1(d)), but subsequent investigations showed that this band is most likely due to substrate effects [132, 128, 129, 130, 131]. For stanene, a recent study reported the successful growth on Bi_2Te_3, however, it indicated a vulnerability to the saturation of the Sn p_z- orbitals, which leads to the destruction of the predicted massive Dirac

cone [127], as illustrated by the experimental dispersion shown with red and blue dots in Figure 5.1(f).

In contrast to silicene and stanene, there have been only a few spectroscopic studies that investigated the electronic structure of germanene, although there are various substrates on which synthesis has been reported: Pt(111) [133], Al(111) [134], Au(111) [135, 126], Ge_2Pt [136], and MoS_2 [137]. Two recent spectroscopic studies claim the existence of a Dirac cone in germanene: Scanning tunneling spectroscopy (STS) investigations of Ge films on MoS_2 report some evidence for the signature of a Dirac cone in the density of states (DOS) [137], but since they lack momentum resolution, they cannot provide conclusive evidence for a Dirac dispersion. Davila and coworkers performed an ARPES study on a thick film of Ge, which according to the authors corresponds to ~4.5 ML of germanene grown on Au(111). They report the appearance of an additional linear band crossing the Fermi level in the projected band gap in the vicinity of the $\overline{K}$ point of the Au(111) substrate surface Brillouin zone, which the authors relate to a Dirac cone of few-layer germanene [126]. However, since no conical shape was reported (see 5.1(e), red lines are guide to the eye but do not represent measured data), and the film consisted of multiple putative monolayers, it remains unclear whether this band is indeed related to the Dirac cone expected for a single layer. Furthermore, some ab-initio calculations predict that the Dirac bands of a buckled Ge honeycomb structure on metallic substrates, such as Al(111) or Au(111), will strongly hybridize with the underlying substrate bands. For instance, Chen et al. calculated the band structure for (3×3) germanene on ($\sqrt{19}\times\sqrt{19}$) Au(111) and found that the Dirac states at the K,K' points of germanene are completely washed out by hybridization [138]. However, the results of such calculations strongly depend on the assumed superstructure of the adlayer. Wang et al. determined that ($\sqrt{3} \times \sqrt{3}$)/($\sqrt{7} \times \sqrt{7}$) Ge/Au(111) and could be a good candidates for observing Dirac states, i.e. they hybridize with substrate bands, but not so strongly that the underlying Dirac dispersions are completely lost. Importantly, they also found the folding of the

Dirac points to the center of the superstructure Brillouin zone [139]. Fengping et al. calculated the electronic structure of Ge on Au(111) using two possible reconstructions - $(2 \times 2)/(\sqrt{7} \times \sqrt{7})$ and $(\sqrt{3} \times \sqrt{3})/(\sqrt{7} \times \sqrt{7})$ germanene/Au(1 1 1), which arrived at similar conclusions, also finding a folding of the Dirac states for the $(\sqrt{3} \times \sqrt{3})/(\sqrt{7} \times \sqrt{7})$ germanene/Au(1 1 1) superstructure [140]. Thus, the question of whether Dirac dispersions may be realized in a buckled honeycomb structure of Ge atoms on Au(111) is currently up for debate and requires experimental confirmation.

In the subsequent sections, we will study the evolution of the electronic structure of ultra-thin Ge films grown in Au(111) whilst tuning the film thickness from the sub-monolayer regime to the trilayer regime, which allows us to identify bands that are replica of the gold substrate. By tuning the light polarization, we can further identify conical Dirac-like bands that may originate from the formation of rotationally disordered germanene.

5.2 Characterization of ultrathin Ge films grown on Au(1 1 1)

Before the deposition of the Ge films, the Au(111) substrate crystals were sputtered and annealed over multiple cycles until a clean X-ray photoelectron spectroscopy (XPS) spectrum and a clear low-energy electron diffraction (LEED) pattern[2], including the characteristic $22 \times \sqrt{3}$ superstructure of the Au(111) surface, was obtained. Subsequently, an amorphous 0.8 Å thick film of Bi was deposited, which in preliminary experiments [143] was found to facilitate the subsequent epitaxial growth of the Ge layers. The nominal thickness of the Bi film and the subsequent Ge layers was monitored by a calibrating the growth rate with a quartz microbalance. Since there

[2]We used a standard XPS and LEED apperatus. The XPS and LEED working principle can be found in standard surface science textbooks, e.g. Ref. [142]

was no reflection high-energy electron diffraction (RHEED)[3] system available to determine the thickness of a Ge monolayer, we exploited a shift in the Ge 3d doublet peak to investigate the chemical environment of the Ge atoms. Figure 5.2(a) shows the evolution of the of the doublet peak positions for various film thicknesses. For the Ge film of nominal thickness of 1.0 Å, the core-level spectrum seems to consist of a single doublet at high binding energy, while for the much thicker film of nominally 7.2 Å the doublet is shifted to lower binding energies. We interpret this shift as two different chemical environments of the Ge atoms, one at the interface to the substrate, and the other in the bulk of the film. The nominally 2.6 Å thick film shows both interface and bulk contributions, and should thus be close but potentially slightly above to the monolayer limit. This finding is also corroborated by the structural transition that can be observed in the LEED patterns, shown in Figure 5.2(b). For the 1.0 Å films we see a complicated pattern that includes ~15x15 diffraction peaks, noted by the six purple circles, which may either be related to the Au(111) $22 \times \sqrt{3}$ supercell, or some new long range order. These peaks disappear in the thicker films and are replaced by an 8x8 superstructure [4], as well as additional rotational disorder peaks at 8x8R-6, 8x8R6, 8x8R24, 8x8R30, 8x8R36, which were already reported in the previous study by Davila and coworkers, and were related by those authors to a germanene adlayer on a 8x8 Au(111) supercell [135].

We also performed scanning tunneling microscopy (STM) measurements with an omnicron room temperature STM on a nominally 3.3 Å thick film, which is shown in Figure 5.3. Although we were not able to obtain atomic resolution, the average film thickness of the ultrathin Ge islands is of the order of ~2.5 Å. This topographic information on its own may not be conclusive to determine a Ge monolayer thickness (the islands found here may not be monolayers, or may be related to Au(111) step edges with height ~2.4 Å [144]), but in conjunction with the core level and LEED

[3]RHEED is a canonical tool to monitor the film thickness during epitaxial growth in molecular-beam epitaxy. More information about the technique can be found e.g. in Ref. [141].

[4]Note, however, that not all peaks fit the 8x8 structural model even when including rotational disorder, so there may be additional domains or a more complicated lattice structure present.

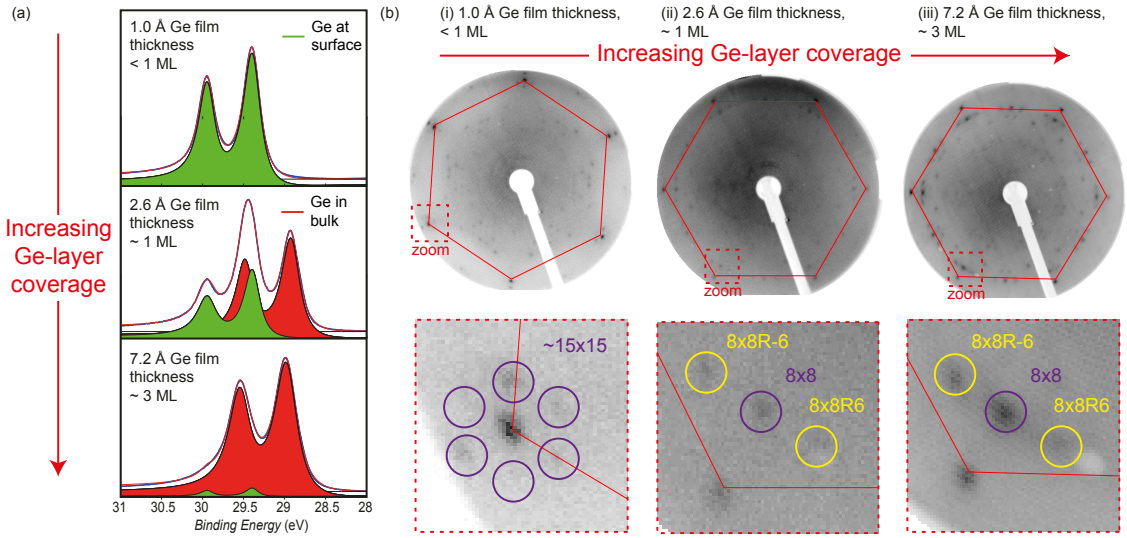


Figure 5.2: **Characterization of the Ge films by core level spectroscopy and LEED.** (a) Core level spectroscopy of the Ge 3d doublet for various film thicknesses. Green and red curves indicate the fitting of an interface doublet at high binding energies and a bulk doublet at lower binding energies. Addtionally, a background was subtracted . Measurements were taken with photon energy of 120 eV in linear-horizontal polarization. Figure courtesy of Matthew Watson. (b) Low-energy electron diffraction (LEED) image for various film thicknesses. Upper panels show the full diffraction pattern, with the red hexagon indicating position of the main Au(111) diffraction spots. Lower panels shows a zoom on the superstructure diffraction peaks, which are highlighted by purple and yellow circles. Figure was drawn in joint collaboration with Matthew Watson, Diamond Light Source, UK, and was published in Ref. [116].

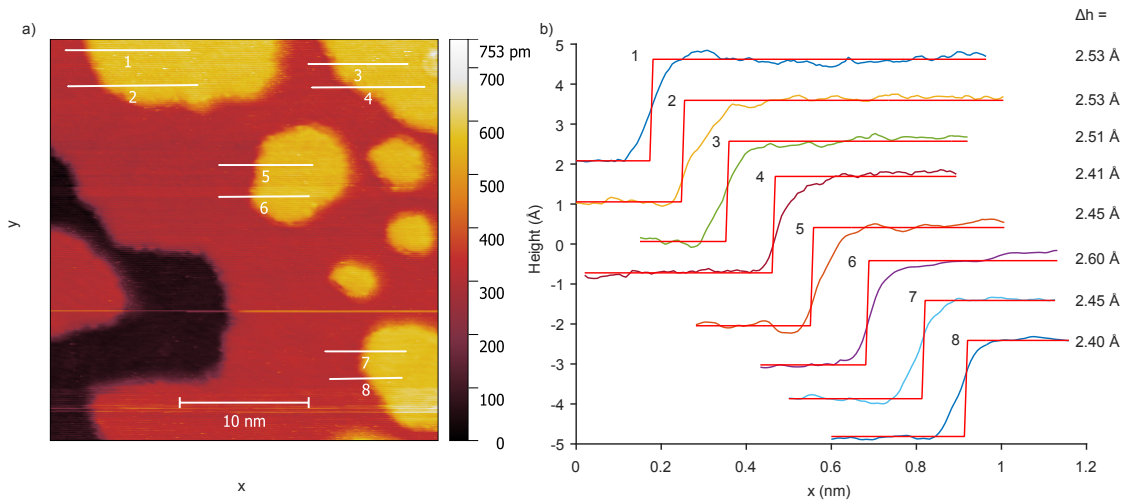


Figure 5.3: **Thickness characterization of Ge islands in film with nominal thickness of 3.3 Å.** (a) Scanning tunneling microscopy (STM) topographic image. (b) Hight profile at the edge of the four islands, indicated by the white lines shown in (a). Measurements were taken with a commercial Omnicron room temperature STM. This Figure was published before in the supplementary material of Ref [116].

measurements it suggests that our 2.6 Å thick films are either close to a Ge monolayer, or at least an important structural film unit. For the remainder of this chapter we will assume that it indeed corresponds to a Ge monolayer, although additional measurements are necessary to unambiguously determine the structure of these layers.

5.3 Band structure evolution with film thickness

Following from the discussion in the previous section, we will now refer to the nominally 1.0 Å, 2.6 Å and 7.2 Å thick films as sub-monolayer, monolayer, and trilayer Ge films. Let us begin with discussing the evolution of the Fermi surface when tuning the layer thickness, as illustrated in Figure 5.4. Figure 5.4(a) shows an overview of the pristine Au(111) Fermi surface, indicating the surface Brillouin zone (BZ) with a red solid line. The red dashed box indicates the magnified area around the projected bulk band gap in the vicinity of the $\overline{K}$ point, which is shown in 5.4(e). The triangu-

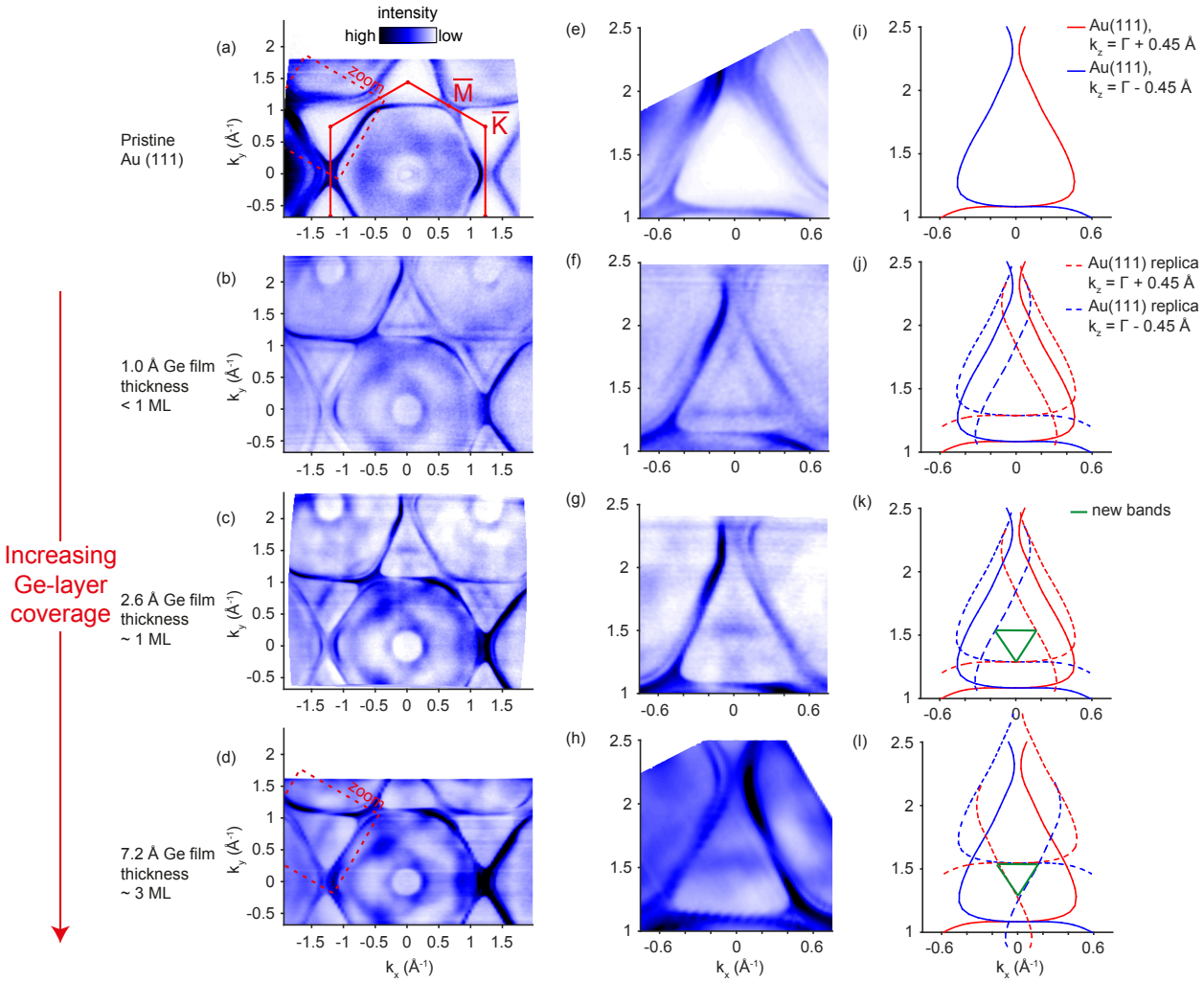


Figure 5.4: **Evolution of the Fermi surface with Ge film thickness.** (a-d) Fermi surface overview for pristine Au(111) and films of increasing thickness, respectively. Red solid lines indcate the boundary of the Au(111) surface Brillouin zone, and the red dashed lines indicate the zoomed areas shown in (e) and (h). (e-h) Close-up of the Fermi surface at the projected band gap of the Au(111) substrate in the vicinity of the $\overline{K}$ point. (i) Ab-initio calculation of the Au(111) Fermi surface for $k_z = \Gamma + 0.45$ Å^{-1} (red solid line) and $k_z = \Gamma - 0.45$ Å^{-1} (blue solid line). (j) Same as above, but with additional replica bands (dashed red and blue lines lines) constructed by a rigid momentum shift. (k) Same as above, but with green triangle that indicates the new bands present in the 2.6 Å thick film. (l) Same as above, but with additional replica bands (dashed lines). . All data taken with 120 eV photon energy and linear-horizontal polarization. This Figure was published in Ref. [116].

lar shape is further illustrated by our ab-initio calculations[5], which show bands with $k_z = \Gamma + 0.45$ Å^{-1} (red solid line) and $k_z = \Gamma - 0.45$ Å^{-1} (blue solid line), indicating the the triangular shape of the projected band gap appears due to k_z broadening. Once the 1.0 Å thick film got deposited, a large triangle appears in the projected band gap around $\overline{K}$, which can be seen in Figures 5.4(b,f). Based on the ab-initio calculations shows in Figure 5.4(j), we can understand that the triangle can be constructed by a rigid band shift of the substrate bulk bands along the $\overline{\Gamma} - \overline{K}$ direction, which leads to the replica bands shown by the dashed red and blue lines. Similar replica bands of quantum well states were previously observed in Cu films on Pt(111) substrates [145] due to a moire potential between adlayer and substrate. A possible explanation for the replica bands found here may therefore be a moire potential due to a lattice mismatch between a hexagonal adlayer and the underlying hexagonal Au(111) substrate. It is also interesting to note that the magnitude of the momentum vector seems to correspond to the ~15x15 reconstruction that we observed in the LEED pattern. Once the nominal film thickness further increases to 2.6 Å, the large triangular bands get suppressed, while smaller triangles appear in the band gap, as is shown in Figures 5.4(c,g,k). When further increasing the layer thickness, the large triangles completely vanish, but the new smaller triangular bands prevail, although two of the three edges seem to lose intensity (see Figures 5.4(d,h)). The new smaller triangle may also be explained by a rigid band shift with a larger shifting vector, as is shown in Figure 5.4(l). However, we will argue below that there may also be an alternative origin of these bands due to the formation of germanene.

After investigating the Fermi surface evolution, we now want to study the change of the band dispersion along the high-symmetry momenta $\overline{\Gamma} - \overline{K} - \overline{M}$ with changing layer thickness. For reference, we show the dispersion of the pristine Au(111) substrate

[5] Calculations were performed with the software Wien2k with a full-potential linearized augmented plane-wave and local orbitals basis, using the Perdew–Burke–Ernzerhof parameterization of the Generalized Gradient approximation, including spin-orbit coupling. The $R_{MT}K_{Max}$ parameter was set to 7, experimental lattice constants were used, and the k-point mesh was set to 10000 k-points in the Brillouin zone.

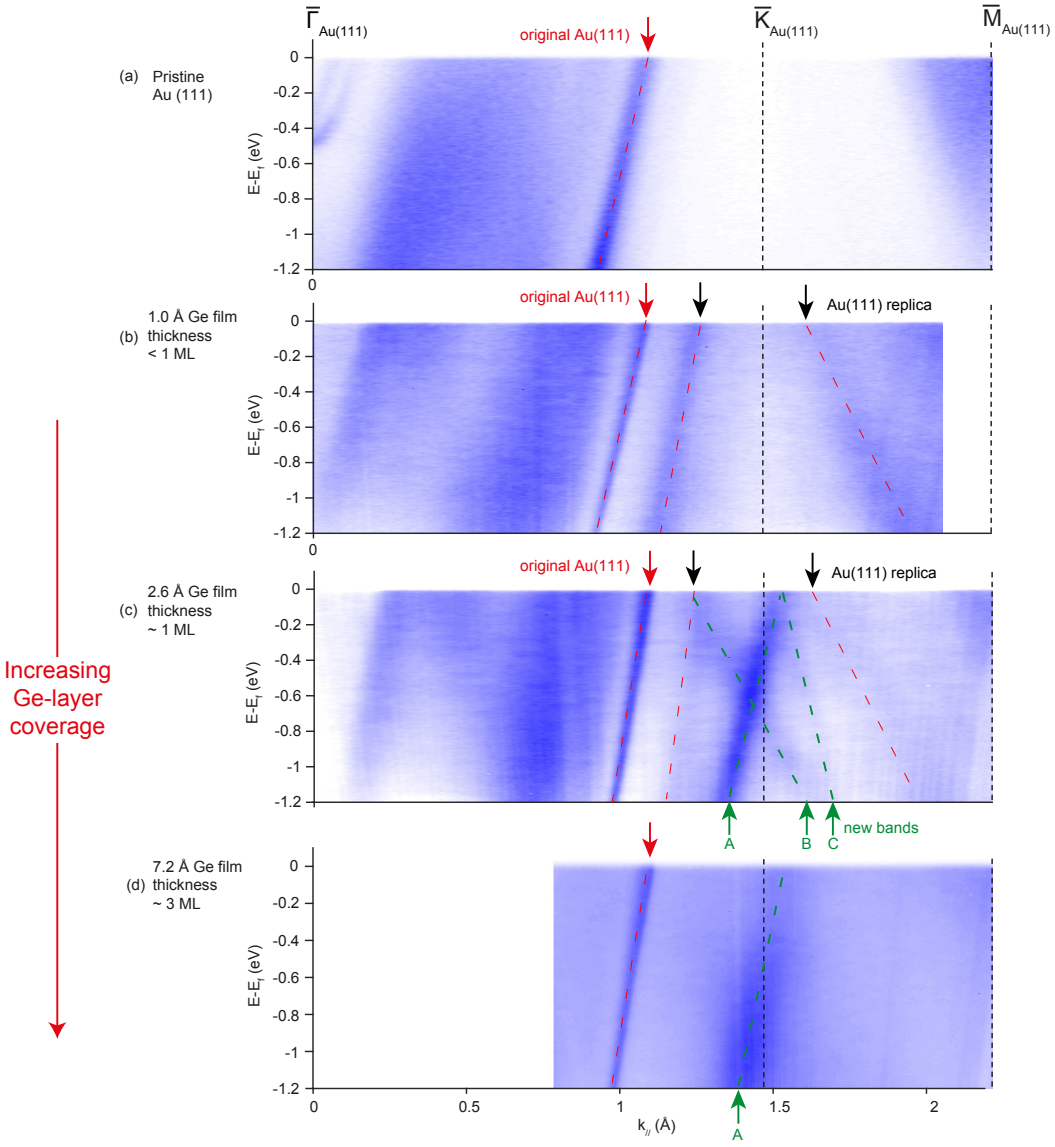


Figure 5.5: **Evolution of the Ge film band dispersion with layer thickness.** (a) Bands of the pristine Au(111) substrate. Red dashed line is guide to the eye of a strong substrate band. (b) Dispersions of the 1.0 Å thick Ge film, red dashed lines are guide to the eye of the original Au(111) band shown in (a) indicated by the red arrow, and new replica bands indicated by black arrows. (c) Dispersions of the 2.6 Å thick film, showing three new bands indicated by green arrows and dashed lines. (d) Dispersion of the 7.2 Å thick film, arrows and dashed lines as above. All data was taken with hv=120 eV photon energy and linear-horizontal polarization. This Figure was published in Ref. [116].

in Figure 5.5(a), which shows the well known Rashba surface state at $\overline{\Gamma}$, a strong band crossing between $\overline{\Gamma} - \overline{K}$, and a local band gap in the vicinity of $\overline{K}$. Once the 1.0 Å thick layer is deposited, two additional bands appear as shown in Figure 5.5(b), which are indicated by red dashed lines and black arrows. They are the bands that form the large triangles on the Fermi surface that we have seen in Figures 5.4(b,f), and they can be understood as replica of the Au(111) substrate band that is indicated by the red arrow. For the thicker 2.6 Å film, three additional bands appear that are marked by green dashed lines and arrows (A, B, C) in Figure 5.5(c). Bands A and B form the small triangles at the Fermi surface that we have seen in Figures 5.4(c,g), while band C will be discussed in detail below. Note that the band crossing between bands A and B should be right at the $\overline{K}$ point, but is shifted due to a distortion of the spectrum when using a straight analyzer slit and measuring bands that are not in the center of the detector[6]. This distortion is difficult to correct for all energies, but we made sure that the momentum k_f at which the strong Au(111) band is crossing the Fermi level is the same across all spectra, such that the momentum at the Fermi level should be well calibrated. For an even thicker film of 7.2 Å, the bands B, C and the band corresponding to the large triangle are fully suppressed, while band A appears broadened, as can be seen from Figure5.5(d).

All of the measurements presented above were taken with linear-horizontal polarization. When changing the polarization to linear-vertical, we can uncover additional bands for the thicker films, which point to a different origin other than substrate band folding. Figure 5.6(a-b) shows the band dispersions for the 2.6 Å and 7.2 Å thick Ge films, respectively. Interestingly, band C shown in Figure 5.5(c) now becomes far more pronounced and forms a conical pair with band A. conical bands appear around the $\overline{M}$ point. It now becomes an interesting question to ask whether these conical bands may be related to the Dirac cones predicted at the K points of the germanene Brillouin zone (BZ). Indeed, we speculate that the potential of the

[6]This effect is described in the thesis of Felix Schmitt [146], which is called *fanning*.

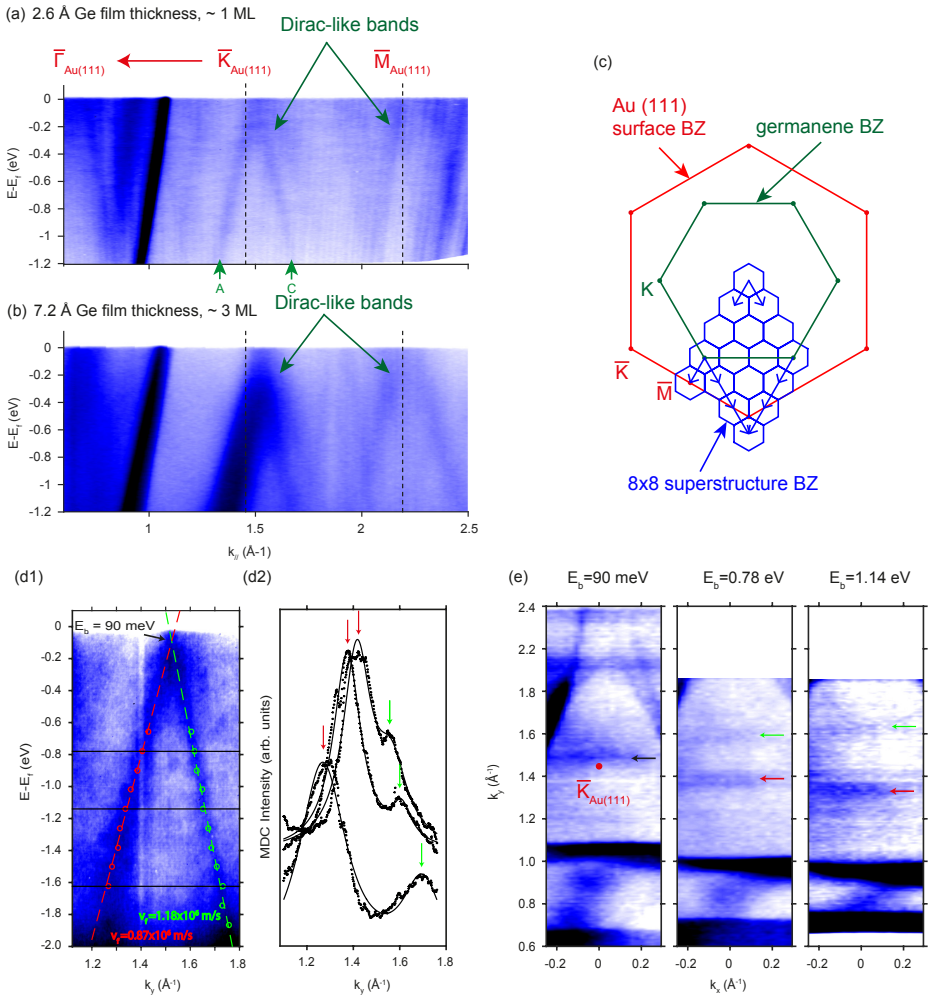


Figure 5.6: **Conical Dirac-like bands in 2.6 Å and 7.2 Å thick Ge films, visible with linear-vertical polarization.** (a-b) Experimental band dispersions for the 2.6 Å and 7.2 Å thick Ge films respectively. Green arrows indicate conical bands centered at the $\overline{M}$ and slightly off the $\overline{K}$ points. (c) Illustration of the Au(111) surface Brillouin zone (red solid line) the hypothetical germanene Brillouin zone (solid green line, based on a 10% enlarged lattice constant of calculated freestanding germanene), and 8x8 superstructure Brillouin zone (blue solid line). The blue arrows indicate folding vectors that would replicate the Dirac cone from the K point of the Germanene Brillouin zone to the $\overline{M}$ point and slightly off the $\overline{K}$ point of the Au(111) Brillouin zone. (d1) Close up of the conical band dispersion of the 2.6 Å thick film. Red and green dots represent the peak positions obtained from a momentum-distribution curve fitting. Dashed red and green lines correspond to a fitting of the peak positions. (d2) Representative momentum distribution curves (black dots are raw data, black solid lines are fitting data) at the energies shown by the black solid lines in (d1). Red and green arrows indicate the peak positions. (e) Equal energy surfaces for the 2.6 Å thick film at 0.09 eV, 0.78 eV and and 1.14 eV, respectively. Black, red and green arrows correspond to the apex, left and right leg of the band cone shown in (d), respectively. All experimental data was taken at hv=120 eV and linear-vertical polarization. This Figure was published in Ref. [116].

8x8 superstructure that we detected in our LEED patters shown above may provide a loophole for the Dirac cones to avoid hybridization by folding them into the projected band gap of the substrate around the $\overline{K}$ point. This hypothetical scenario is illustrated in Figure 5.6(c), which shows the Au(111) surface BZ (red lines), the BZ of germanene (based on a haxagonal lattice with lattice constant a = 4.4 Å, which is 10% larger than the theoretically predicted value for freestanding germanene [147]), and the 8x8 superstructure BZ (solid blue lines). We now assume that the potential of the superstructure is replicating the features at the K point of the germanene BZ (which is in the center of the superstructure BZ) to the $\overline{M}$ point and slightly off the $\overline{K}$ point of the Au(111) BZ, as is illustrated by the blue reciprocal lattice vectors of the superstructure BZ. Such a replication of Dirac cones would be similar to the Dirac cone replica of graphene on Iridium(111) due to the superstructure potential of the moire pattern between honeycomb adlayer and hexagonal substrate [148]. Figure 5.6(d,1-2) shows a close up of the putative Dirac cone of the 2.6 Å thick film, and results of a momentum distribution curve fitting that allows us to extract the cone apex (at around ~90 meV) and the Fermi velocities for the to legs of the cone (~ 10^6 m/s, in the same order of magnitude as graphene [149]). Figure 5.6(e) shows the equal energy for energies at the apex of the cone and two more higher binding energies. For a Dirac cone similar to graphene we would expect a circular Fermi surface, but here we only find two nearly parallel bands. A similar Fermi surface was found for rationally disordered graphene grown on copper [150], and may be related to the rotational domains of the 8x8 superstructure that we observed in the LEED patterns shown above.

5.4 Discussion and prospects for further study

Before we want to discuss our results, let us summarize our findings. We have reported a detailed core-level spectroscopy, LEED, and ARPES study of ultrathin Ge films with

nominal thicknesses between 1.0 Å and 7.2 Å. The core level spectra reveal different chemical environments of the Ge atoms that correspond to the interface and the bulk, and the LEED patterns show a structural transition between the 1.0 Å thick film and the films thicker than 2.6 Å. Our ARPES measurements reveal substrate replica bands for the thinnest films, and conical Dirac-like bands for the thicker films that may be related to Dirac cone replica from the formation of rotationally disordered germanene. This is surprising, since the Dirac cones of germanene on metallic substrates were previously expected to vanish due to hybridization with substrate bands, which may be overcome due to a folding of the Dirac cones by the 8x8 superstructure into the projected band gap of the substrate. However, at this point we cannot exclude the possibility that the Dirac-like bands may be related to substrate band replica. Thus, there is a strong motivation for further structural and spectroscopic studies. On the one hand, it will be interesting to investigate the microscopic structure of the Ge films, for instance by grazing incidence XRD, or atomically resolved scanning probe microscopy methods. Such structural information will be necessary to model the electronic structure of these films computationally, which can provide a comparison to our ARPES results. Furthermore, it would be interesting to also measure the unoccupied states of the Dirac-like bands, for instance by in-situ doping or pump-probe techniques, to probe the upper half of the putative Dirac cone.

Overall, we can conclude that similar to the putative honeycomb lattices made out of Si and Sn, conclusive evidence for the realization of germanene and its Dirac cones is still elusive. However, at the time of finishing this chapter, a study reporting the realization of a honeycomb lattice made out of Bismuth grown on SiC was published [152]. The authors report STM and LEED images showing a perfect honeycomb structure, whilst ARPES and STS confirm the existence of a massive Dirac cone with an extremely large gap of ~0.8 eV, as well as the existence of a metallic edge state in the bulk band gap. These findings make Bismuthene on SiC the most promising candidate for the realization of a room temperature quantum spin-Hall system.

References

[115] M Zahid Hasan and Charles L Kane. Colloquium: topological insulators. *Reviews of Modern Physics*, **82**(4):3045, 2010.

[116] Niels B M Schröter, Matthew D Watson, Liam B Duffy, Moritz Hoesch, Yulin Chen, Thorsten Hesjedal, and Timur K Kim. Emergence of Dirac-like bands in the monolayer limit of epitaxial Ge films on Au(1 1 1). *2D Materials*, **4**(3):031005, 2017.

[117] AH Castro Neto, F Guinea, Nuno MR Peres, Kostya S Novoselov, and Andre K Geim. The electronic properties of graphene. *Reviews of modern physics*, **81**(1):109, 2009.

[118] C. L. Kane and E. J. Mele. Quantum Spin Hall Effect in Graphene. *Physical Review Letters*, **95**:226801, Nov 2005.

[119] Xiao Zhang and Shou-Cheng Zhang. Chiral interconnects based on topological insulators. *Micro-and Nanotech. Sens., Sys., and App. IV*, **8373**:837309, 2012.

[120] Christoph Brune, Andreas Roth, Hartmut Buhmann, Ewelina M. Hankiewicz, Laurens W. Molenkamp, Joseph Maciejko, Xiao-Liang Qi, and Shou-Cheng Zhang. Spin polarization of the quantum spin Hall edge states. *Nature Physics*, **8**(6):485–490, 2012.

[121] Yugui Yao, Fei Ye, Xiao-Liang Qi, Shou-Cheng Zhang, and Zhong Fang. Spin-orbit gap of graphene: First-principles calculations. *Physical Review B*, **75**(4):041401, 2007.

[122] Markus König, Steffen Wiedmann, Christoph Brüne, Andreas Roth, Hartmut Buhmann, Laurens W Molenkamp, Xiao-Liang Qi,

and Shou-Cheng Zhang. Quantum spin Hall insulator state in HgTe quantum wells. *Science*, **318**(5851):766–770, 2007.

[123] Cheng-Cheng Liu, Wanxiang Feng, and Yugui Yao. Quantum Spin Hall Effect in Silicene and Two-Dimensional Germanium. *Physical Review Letters*, **107**(7):076802, 2011.

[124] Yong Xu, Binghai Yan, Hai-Jun Zhang, Jing Wang, Gang Xu, Peizhe Tang, Wenhui Duan, and Shou-Cheng Zhang. Large-Gap Quantum Spin Hall Insulators in Tin Films. *Physical Review Letters*, **111**(13):136804, 2013.

[125] Patrick Vogt, Paola De Padova, Claudio Quaresima, Jose Avila, Emmanouil Frantzeskakis, Maria Carmen Asensio, Andrea Resta, Benedicte Ealet, and Guy Le Lay. Silicene: Compelling Experimental Evidence for Graphenelike Two-Dimensional Silicon. *Physical Review Letters*, **108**(15):155501, 2012.

[126] Maria Eugenia Davila and Guy Le Lay. Few layer epitaxial germanene: a novel two-dimensional Dirac material. *Scientific Reports*, **6**:20714, 2016.

[127] Feng-feng Zhu, Wei-jiong Chen, Yong Xu, Chun-lei Gao, Dan-dan Guan, Can-hua Liu, Dong Qian, Shou-Cheng Zhang, and Jin-feng Jia. Epitaxial growth of two-dimensional stanene. *Nature Materials*, **14**(10):1020–1025, 2015.

[128] Zhi-Xin Guo, Shinnosuke Furuya, Jun-ichi Iwata, and Atsushi Oshiyama. Absence of Dirac Electrons in Silicene on Ag(111) Surfaces. *Journal of the Physical Society of Japan*, **82**(6):063714, 2013.

[129] Yun-Peng Wang and Hai-Ping Cheng. Absence of a Dirac cone in silicene on Ag(111): First-principles density functional calculations with a modified effective band structure technique. *Physical Review B*, **87**(24):245430, 2013.

[130] Chun-Liang Lin, Ryuichi Arafune, Kazuaki Kawahara, Mao Kanno, Noriyuki Tsukahara, Emi Minamitani, Yousoo Kim, Maki Kawai, and Noriaki Takagi. Substrate-Induced Symmetry Breaking in Silicene. *Physical Review Letters*, **110**(7):076801, 2013.

[131] S. K. Mahatha, P. Moras, V. Bellini, P. M. Sheverdyaeva, C. Struzzi, L. Petaccia, and C. Carbone. Silicene on Ag(111): A honeycomb lattice without Dirac bands. *Physical Review B*, **89**(20):201416, 2014.

[132] Paola Gori, Olivia Pulci, Fabio Ronci, Stefano Colonna, and Friedhelm Bechstedt. Origin of Dirac-cone-like features in silicon structures on Ag (111) and Ag (110). *Journal of Applied Physics*, **114**(11):113710, 2013.

[133] Linfei Li, Shuang-zan Lu, Jinbo Pan, Zhihui Qin, Yu-qi Wang, Yeliang Wang, Geng-yu Cao, Shixuan Du, and Hong-Jun Gao. Buckled Germanene Formation on Pt(111). *Advanced Materials*, **26**(28):4820–4824, 2014.

[134] Mickael Derivaz, Didier Dentel, Regis Stephan, Marie-Christine Hanf, Ahmed Mehdaoui, Philippe Sonnet, and Carmelo Pirri. Continuous Germanene Layer on Al(111). *Nano Letters*, **15**(4):2510–2516, 2015.

[135] M. E. Davila, L. Xian, S. Cahangirov, A. Rubio, and G. Le Lay. Germanene: a novel two-dimensional germanium allotrope akin to graphene and silicene. *New Journal of Physics*, **16**(9):095002, 2014.

[136] P Bampoulis, L Zhang, A Safaei, R Van Gastel, B Poelsema, and H J W Zandvliet. Germanene termination of Ge2Pt crystals on Ge (110). *Journal of Physics: Condensed Matter*, **26**(44):442001, 2014.

[137] L. Zhang, P. Bampoulis, A. Rudenko, Q. Yao, A. van Houselt, B. Poelsema, M. Katsnelson, and H.J.W. Zandvliet. Structural

and Electronic Properties of Germanene on MoS_2. *Physical Review Letters*, **116**(25):256804, 2016.

[138] M. X. Chen, Z. Zhong, and M. Weinert. Designing substrates for silicene and germanene: First-principles calculations. *Physical Review B*, **94**(7):075409, 2016.

[139] Yangyang Wang, Jingzhen Li, Junhua Xiong, Yuanyuan Pan, Meng Ye, Ying Guo, Han Zhang, Ruge Quhe, and Jing Lu. Does the Dirac cone of germanene exist on metal substrates? *Physical Chemistry Chemical Physics*, **18**(28):19451–19456, 2016.

[140] Li Fengping, Wei Wei, Yu Lin, Huang Baibiao, and Dai Ying. Interface effects between germanene and Au(1 1 1) from first principles. *Journal of Physics D: Applied Physics*, **50**(11):115301, 2017.

[141] Pekka Laukkanen, Janusz Sadowski, and Mircea Guina. Surface Studies by Low-Energy Electron Diffraction and Reflection High-Energy-Electron Diffraction. In *Semiconductor Research*, pages 1–21. Springer, 2012.

[142] D Phil Woodruff. *Modern techniques of surface science*. Cambridge University Press, 2016.

[143] Timur K Kim and Alexander A Baker. (private communication), 2015.

[144] JV Barth, H Brune, G Ertl, and RJ Behm. Scanning tunneling microscopy observations on the reconstructed Au (111) surface: Atomic structure, long-range superstructure, rotational domains, and surface defects. *Physical Review B*, **42**(15):9307, 1990.

[145] P Moras, PM Sheverdyaeva, C Carbone, D Topwal, L Ferrari, G Bihlmayer, S Ouazi, S Rusponi, A Lehnert, and H Brune. Electronic

states of moiré modulated Cu films. *Journal of Physics: Condensed Matter*, **24**(33):335502, 2012.

[146] Felix T.H. Schmitt. *Electronic Structure and Collective Excitations in Correlated Materials - Frequency and Time Domain Perspectives*. PhD thesis, Stanford University, 2011.

[147] S. Lebègue and O. Eriksson. Electronic structure of two-dimensional crystals from ab initio theory. *Phys. Rev. B*, **79**:115409, Mar 2009.

[148] I. Pletikosić, M. Kralj, P. Pervan, R. Brako, J. Coraux, A. T. N'Diaye, C. Busse, and T. Michely. Dirac Cones and Minigaps for Graphene on Ir(111). *Physical Review Letters*, **102**:056808, Feb 2009.

[149] David A. Siegel, Cheol-Hwan Park, Choongyu Hwang, Jack Deslippe, Alexei V. Fedorov, Steven G. Louie, and Alessandra Lanzara. Many-body interactions in quasi-freestanding graphene. *Proceedings of the National Academy of Sciences*, **108**(28):11365–11369, 2011.

[150] J Avila, Ivy Razado, Stephane Lorcy, Romain Fleurier, Emmanuelle Pichonat, Dominique Vignaud, Xavier Wallart, and Maria C. Asensio. Exploring electronic structure of one-atom thick polycrystalline graphene films: A nano angle resolved photoemission study. *Scientific Reports*, **3**:2439, 2013.

[151] Shu-Chun Wu, Guangcun Shan, and Binghai Yan. Prediction of Near-Room-Temperature Quantum Anomalous Hall Effect on Honeycomb Materials. *Physical Review Letters*, **113**(25):256401, 2014.

[152] F. Reis, G. Li, L. Dudy, M. Bauernfeind, S. Glass, W. Hanke, R. Thomale, J. Schäfer, and R. Claessen. Bismuthene on a SiC substrate: A candidate for a high-temperature quantum spin Hall material. *Science*, 2017.

Chapter 6

Electronic structure of topological crystalline insulator candidates in the antiperovskite family A_3BO (A=Ca, Sr; B=Sn, Pb)

In this penultimate chapter, we will discuss our measurement of the electronic structure of the antiperovskite material family A_3BO (A=Ca, Sr; B=Sn, Pb), which are predicted to host a topological crystalline insulator (TCI) phase. We will first present a brief introduction to the subject of TCIs. Subsequently, we will present out ARPES measurements for various A_3BO family members, which shows that their electronic structure is in good agreement with previously published ab-initio calculations. However, despite the repeated attempts of our collaborators to improve the sample growth, all of our so far measured samples remained intrinsically p-type doped, which leaves the predicted topological Dirac surface states unoccupied and therefore inaccessible to static ARPES. Therefore, we were so far unable to confirm the putative TCI phase in the antiperovskites. At the end of this chapter, we will propose further experiments to address this limitation. Furthermore, superconductivity was recently found for hole

doped Sr_3SnO, with was speculated to realize an exotic odd-parity superconducting state. Two recently published ab-initio calculations make conflicting predictions about the Fermi surface morphology of Sr_3SnO, which may affect the parity of the Cooper pairs. Here, we can clarify this discrepancy by comparison with our experiments. All the ARPES data presented in this chapter was measured by the author of this thesis at the beamline I05 of the Diamond Light Source with the support of Zhongkai Liu, Haifeng Yang, and Cheng Chen. All the data analysis and figure preparation was also performed by the author. All measurements were taken at a temperatures below T=20 K and in an UHV environment with base pressure better than 3×10^{-10} mbar. The samples used here were provided by Claus Mühle and Andreas Rost from the Max Planck Institute for Solid State Research in Stuttgart, Germany.

6.1 Introduction to topological crystalline insulators (TCIs)

After the discovery of $\mathbb{Z}_2$ topological insulators (TIs) with time-reversal symmetry, it became natural question to ask whether there can be a topological classification of insulators based on crystalline symmetries. Indeed, such classification was achieved theoretically [153], and the resulting materials were called topological crystalline insulators (TCIs). Similar to TIs, TCI also host metallic surface states on the boundaries to their topologically trivial environments. However, in contrast to strong TIs that display these surface states on all surfaces, the surface states of TCIs are only present on those cleavage planes that observe the bulk symmetries (e.g. mirror symmetry) that are needed to define the corresponding topological invariants. The most commonly applied topological invariant based on a mirror symmetry is the so called *mirror Chern number*, which is defined with respect to a mirror symmetry. The wavefunctions of a system with mirror symmtry can be decomposed into two subspaces with opposite eigenvalues $\pm i$. For each of the two subspaces, one can now define a Chern

number $N_{\pm}$. For systems that do not exhibit the quantum Hall state, the total Chern number $N = N_+ + N_-$ is zero, but it is still possible that the *mirror Chern number* $N_M = N_+ - N_-$ can be nonzero. This topological invariant defines a symmetry protected insulating phase, in the sense that if the underlying mirror symmetry remains preserved, the topological classification and presence of surface states can only change if the bulk band gap closes [154].

The first prediction for a TCI phase in real compounds was made for the SnTe material class in 2012 [155], and shortly afterwards, experimental evidence for the existence of topological surface states [156, 157] and their helical spin structure [158] was found in different family members. Interestingly, their surface states are predicted to have quite different properties compared to the single Dirac cone surface states in ordinary TIs. The SnTe family has a rocksalt crystal structure, and the mirror plane that is used to define the mirror Chern number, is the (110) mirror plane. There are three types of surfaces that observe this mirror symmetry, namely the (001), (111) and (110) surface; the respective bulk and surface Brillouin zones (BZs) are shown in Figure 6.1(a). As it turns out, the possible surface states differ between the surfaces, which is shown in Figure 6.1(b). On the one hand, the (001) and (110) surfaces display double-Dirac cones at the $\overline{X}$ points, which are due to the hybridization of Dirac cones from band inversions at two different L points in the bulk BZ, and are shown in more detail in Figure 6.1(c). The fact that the cones are not lying on, but are slightly off time-reversal invariant moments (they are centered at the moments $\overline{\Lambda}_1, \overline{\Lambda}_2$) bears evidence to the fact that the underlying symmetry guaranteeing the existence of the surface state is not time-reversal symmetry, but a crystalline mirror-symmetry. As a result of these unusual properties of the surface states in the bulk band gap, the fermi surface is drastically changing its shape when the Fermi energy is changing: at low Fermi energies it consists of two disconnected pockets which merge into a large electron pocket and a small hole pocket at higher Fermi energies. This change from disconnected to connected Fermi surfaces is referred to as Lifshitz transition and leads

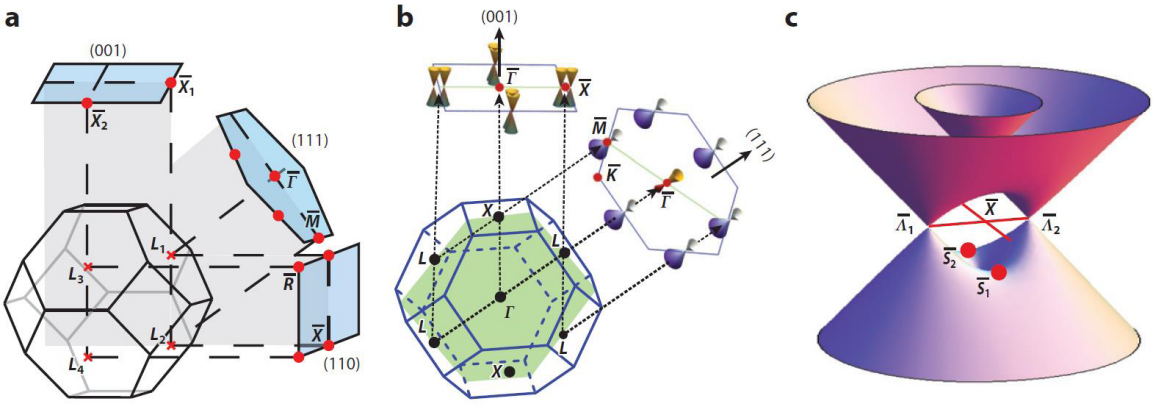


Figure 6.1: **TCI surface states in the SnTe material class.** (a-b) Bulk and surface Brillouin zones, indicating the surfaces observe the bulk mirror symmetries that support TCI surface states, as well as the two different types of Dirac surface states. (c) Unusual double Dirac cone predicted for the (001) surface, which leads to a Lifshitz transition and Van Hove singularity. Figures were taken from Ref. [154].

to a Van Hove singularity at the transition point [154]. On the other hand, on the (111) surface, the Dirac cones originating from different L points do not hybridize, and therefore resemble more closely the surface states known from ordinary TIs.

Besides the fundamental interest in their unusual physical properties, the research in TCI phases is also driven by potential device applications. Scanning tunnelling microscopy (STM) experiments have shown that distortions of the crystal lattice can selectively break one out of two mirror symmetries in $Pb_{1-x}Sn_xSe$ and thereby generate a bandgap in two out of four TCI Dirac cones [159] Theoretical calculations show that right- and left-polarized light is absorbed differently in different gapped Dirac cones, which would allow for selective excitations in certain cones, with possible applications in valleytronics [160]. Another proposal involves thin films of TCIs that allow for an opening and closing of Dirac cones by applying an out of plane electric field, which could be used for a topological transistor device [161]. Another interesting question is how robust the TCI surface states are against perturbations, such as disorder. In the presence of time-reversal symmetry, it is expected that due to disorder averaging, and the average mirror symmetry continuous to protect the surface states (see e.g. Ref. [154]). However, in the presence of Rashba spin-orbit coupling, this protection

may be lifted [162].

6.2 TCI phase in the antiperovskite family A_3BO (A=Ca, Sr; B=Sn, Pb)

The antiperovskite family A_3BX, with A=Ca, Sr; B=Pb, Sn; and X=O is the inverted form of the better known perovskite structure, where the oxygen is swapped from the centre to the face-centred positions, as shown in Figure 6.2(a). The simple cubic unit cell of the antiperovskites leads to a simple cubic Brillouin zone, which is shown in Figure 6.2(b), which also includes the high-symmetry points. Density functional theory calculations have shown that some members of this material family show an unusual band structure close to the Fermi energy [163]. The normal band ordering of an ionic insulator corresponds to bands derived from the d-orbitals of the A^{2+} cations lying energetically above bands derived from the p-orbitals of the B^{4-} anion. However, it turned out that for some family members of this antiperovskite class, the band parity ordering at the Fermi energy is inverted due to spin-orbit coupling (SOC), for instance for the compound Sr_3PbO, while others show the trivial ordering of an ionic insulator, such as Ca_3SnO. This band inversion leads to the formation of a bulk Dirac point in the vicinity of the Γ-point, which is gapped (forming massive Dirac fermions) due to SOC. Although the inverted antiperovskites are trivial in the $\mathbb{Z}_2$ classification of topological insulators, Hsieh and co-workers [163] found that a nonzero mirror Chern number indicates a topologically non-trivial TCI phase for the family members with inverted band structure. The density functional theory band structure calculation for various compounds in shown in Figure 6.2(c-f), which also indicates the parity ordering of the bands, thus distinguishing the topologically trivial Ca_3SnO from the other topologically nontrivial compounds. Additional evidence for the nontrivial topological character was later on provided by Chiu and coworkers [165], whose surface state calculations for Ca_3PbO indicate the existence of Dirac sur-

face states on various surfaces, as shown in Figure 6.2(g-i). Measuring the dispersion of these predicted surface states, for instance with ARPES, would therefore allow us to experimentally confirm the topological classification of the antiperovskites. To the best of our knowledge, there exists so far no conclusive experimental evidence for a topologically nontrivial oxide material, despite numerous theoretical proposals (for a summary, see for instance Ref. [166]). Given that oxide compounds are a very important material class that can typically be grown with very high crystalline quality and host various physical phenomena, such as superconductivity, ferroelectricity, ferromagnetism, and transparent conductivity [166], it would be an important proof of principle to find a topological phase in the A_3BO oxide family, which may pave the way to combine oxide functionality with the exotic physics of topological insulators.

Moreover, hole doped Sr_3SnO (where the doping may be caused due to Sr deficiencies) was recently found to display superconductivity with a transition temperature of $T_c \approx 5$ K, and it was speculated that it may realize exotic odd-parity superconductivity due to spin-orbit coupling induced p-d orbital mixing of the bands at the hole pocket around the Γ point [167], as illustrated in Figure 6.3(a). However, there are two different theoretical predictions about the Fermi surface morphology. Oudah and coworkers predict a global gap and no bands close to the Fermi level at the R point of the charge neural stochiometric Sr_3SnO compound (see Figure 6.3(b)), whilst Hsieh and coworkers predict the existence of a hole pocket at its R point (see Figure 6.3(c)). As a result, the hole doped Sr_3SnO that shows superconductivity should either have only hole pockets at Γ (the Oudah prediction), which could realize the unconventional odd-parity pairing due to the p-d orbital mixing, or hole pockets at Γ and R (the Hsieh prediction), which could alter the paring due to the substantial additional density of states at the R pocket that are not involved in any band inversion and should therefore not be affected by orbital mixing. The difference between the two results may be used by the different programs used to calculate the band structures (which use slightly different approximations), or different levels of resolution used to

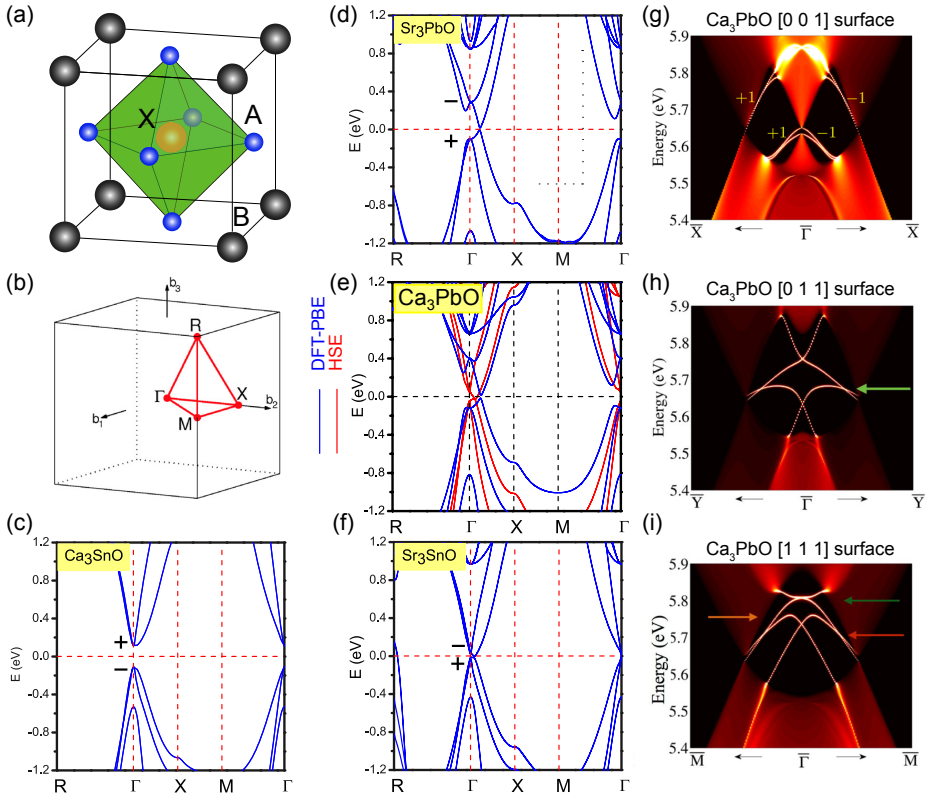


Figure 6.2: **Overview of the crystal- and bandstructure of the antiperovskite family.** (a) Simple cubic unit cell of the cubic antiperovskites, where A = Ca, Sr, Ba; B=Pb, Sn and X = O. (b) Resulting simple cubic bulk Brillouin zone, indicating high symmetry points. (c-f) Ab-initio calculations for topologically trivial Ca_3SnO and non-trivial Sr_3PbO, Ca_3PbO, and Sr_3SnO. The ± signs indicate the parity of the conduction and valence bands. Blue lines indicate calculation results from the Perdew-Burke-Ernzerhof (PBE) functional, red lines indicate results obtained with the Heyd-Scuseria-Ernzerhof (HSE) hybrid-functional. (g-i) Surface state calculations for different cleavage planes of Ca_3PbO, colored arrows indicate the position of the Dirac points. The numbers in (g) indicate the mirror eigenvalues of the surface states. Figures (a,c-f) were taken from Ref. [163], Figure (b) was taken from Ref. [164], and Figures (g-i) were taken from Ref. [165].

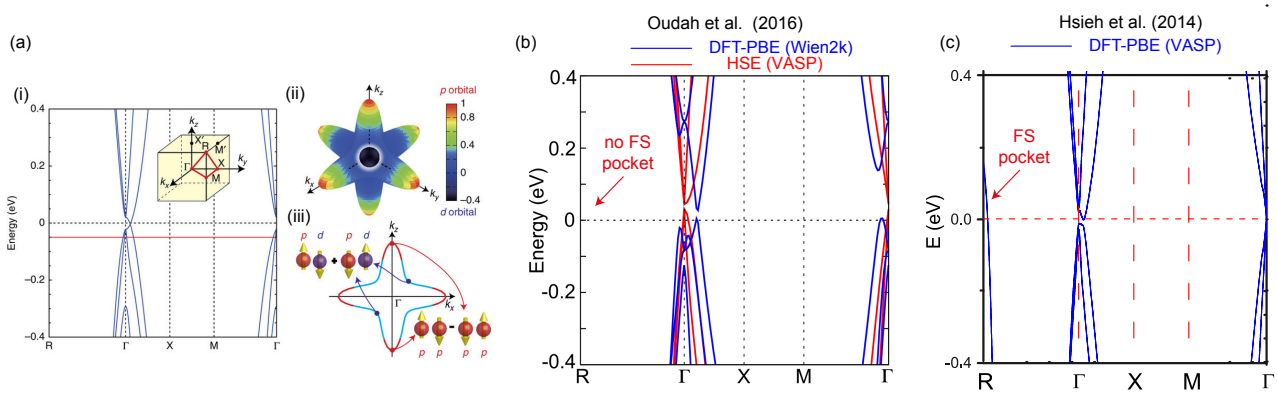


Figure 6.3: **Odd-parity superconductivity in hole doped Sr_3SnO and inconsistant ab-initio calculations.** (a,i) Tight binding model for Sr_3SnO obtained by fitting to the ab-initio calculation. The red solid line indicates the hypothesized position of the Fermi level in the hole doped compounds. (a,ii) Resulting hole-like Fermi pocket at the Γ point, indicating different degrees of contribution from p- and d- orbitals due to the band-inversion induced hybridization. (a,iii) Possible pairing scenarios for Cooper pairing at the Fermi surface. If pairing is dominated by quasiparticles in the blue region where there is strong p-d orbital mixing, then odd-parity pairing is favoured. If pairing is dominated by the red region, even parity pairing is favoured. (b) Bulk band structure calculations for Sr_3SnO as reported by Ouda et al., red lines were calculated with the HSE method in the program VASP, and blue lines with the PBE method in the program Wien2k. Both methods show no hole pocket at the R point. (c) Bulk band structure calculations for Sr_3SnO as reported by Hsieh et al., blue lines with the PBE method in the program VASP. There is a hole-like pocket predicted at the R point. Figures (a-b) were taken from Ref. [167], and Figure (c) was taken from Ref. [163]. Parameters used for the ab-initio calculations can be found in the two references.

perform the calculations (Oudah et al. discretize the irreducable Brillouin zone on a k-space grid of $20 \times 20 \times 20$, while Hsieh et al. discretize on a grid of $11 \times 11 \times 11$), or slightly different lattice parameters used (Oudah et al. stick to experimentally determined lattice parameters, while Hsieh et al. allow the atoms to relax in order to minimize the overall energy). However, given that it was recently shown that most density functional theory codes converge towards very similar results [168], and it can be assumed that the authors of both papers did a convergence study of the k-space grid that they used, it is surprising to see such a drastic qualitative difference in their results which shows the need for experimental verification.

6.3 ARPES study Sr_3SnO, $(Ca_{1-x}La_x)_3PbO$, and Sr_3PbO

We now turn to the results of our ARPES study for three different compounds from the antiperovskite family. Let us begin with our investigation of ARPES data from the [1 1 1] surface of Sr_3SnO, which was reported to show superconductivity that may originate from unconventional odd-parity paring. Figure 6.4(a) shows the three dimensional simple cubic Brillouin zone, which was aligned such that the k_z direction points along [1 1 1] direction. As a result, the in-plane momentum measured for a fixed photon energy will be in the k_x vs. k_y plane. If the photon energy corresponds to $k_z = \Gamma$, then the measured bulk Brillouin zone boundary should correspond to the solid blue line that indicates a sixfold symmetry. For the subsequent photon energy dependent measurements, it is also helpful to illustrate the Brillouin zone boundary in the k_z vs. k_y plane, which is shown as a red solid line. From our photon energy dependent measurements, we can extract the Fermi surface in the k_z vs. k_y plane (displayed in Figure 6.4(b), an inner potential of $V_0 = 12$ eV was used to convert the data), which shows excellent agreement with the expected periodicity. From this measurement it appears that there are only Fermi surface pockets at the Γ point, but not at the R point (as was predicted in the calculation by Hsieh et al.). It may be possible that the pockets at the R points may be invisible due to matrix element effects (the photon energy dependent measurement was only taken with LH polarization), but since there is not even a faint signature of any bands at R (and selection rules are often slightly relaxed), and the band evolution can be tracked well for all binding energies along k_z, it seems unplausible that different bands would become visible at other polarizations. Thus, it is most likely that the superconductivity in Sr_3SnO will be governed by the quasiparticle pairing of the only existing pocket at the Γ point that may be odd parity due to p-d mixing, as hypothesized by Oudah et al. From the Fermi surface in the k_z vs. k_y plane we can also determine the photon energies corresponding to the $k_z = \Gamma$ plane, one of which is 148 eV. The corresponding cut

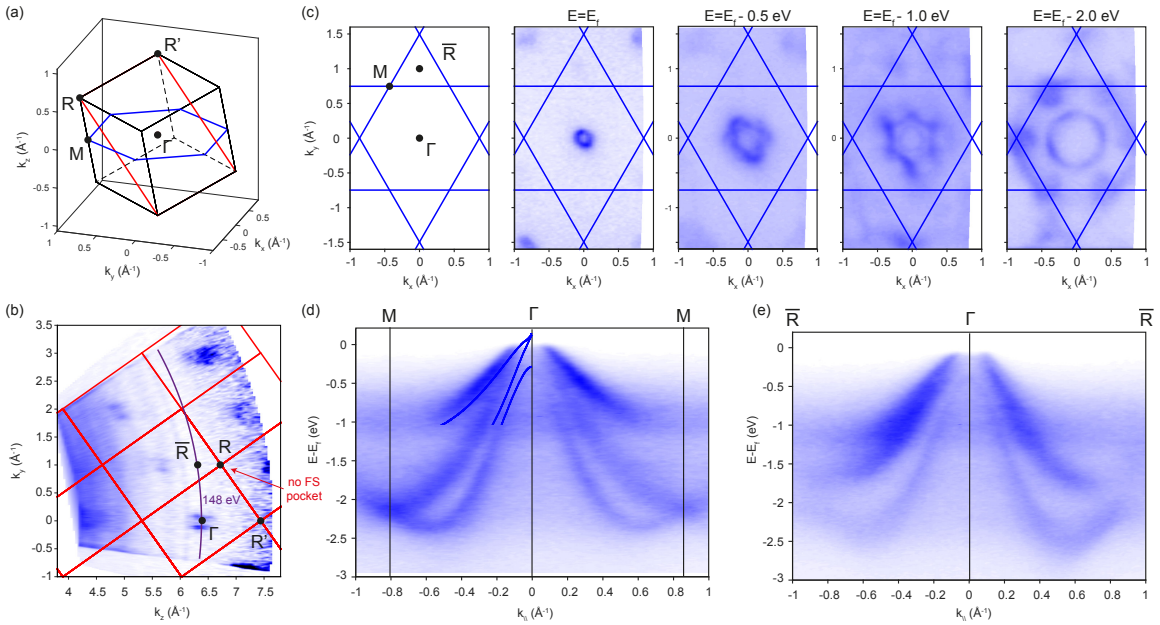


Figure 6.4: **Experimental band structure of Sr_3SnO determined from its [1 1 1] cleavage plane.** (a) Three dimensional simple-cubic Brillouin zone (BZ), rotated such that the [1 1 1] direction points along the k_z axis. The blue solid line indicates the BZ boundary in the k_x vs. k_y plane for a value of$k_z = \Gamma$. The red solid line indicates the BZ boundary of the k_z *vs.* k_y plane. (b) k_z *vs.* k_y plane obtained from a photon energy dependent measurement (inner potential used for k_z conversion $V_0 = 12$ eV). The magenta line indicates the momentum position of the Fermi surface obtained at a photon energy of 148 eV, which corresponds to the $k_z = \Gamma$ plane. (c) Equal energy surfaces in the k_x *vs.* k_y plane for various binding energies, taken with 148 eV photon energy. The blue lines indicate the boundaries of the bulk Brillouin zone. (d-e) Energy vs. momentum dispersions taken with 148 eV photon energy along the $M - \Gamma - M$ direction, and $\bar{R} - \Gamma - \bar{R}$ direction, respectively. The solid blue lines represent the calculated band structure taken from Ref. [163], computed with the Perdew-Burke-Ernzerhof (PBE) functional, which was shifted by ~150 meV to fit the data. All experimental data shown here was taken with linear-horizontal polarization.

through momentum space is shown by the magenta line in Figure 6.4(b). The equal energy surfaces taken at this photon energy are shown in Figure 6.4(c), which perfectly match the expected sixfold symmetry from the Brillouin zone boundary in the $k_z = \Gamma$ plane, shown in blue. From this map, we can extract to energy vs. momentum dispersions displayed in 6.4(d-e), one along $M - \Gamma - M$, and another along $\overline{R} - \Gamma - \overline{R}$ (the momentum position of $\overline{R}$ is shown in Figures 6.4(b,c)). From the comparison with the calculation by Hsieh et al. for the $M - \Gamma - M$ direction, we can see that our measured samples are indeed hole doped (most likely due to a Sr deficiency as in the samples reported by Oudah et al.), which leads to a Fermi energy shift of ~150 meV to higher binding energies. As a result, we are unable to investigate the predicted massive Dirac cone (which would be a signature of the band inversion) or the predicted TCI surface states in the unoccupied states. Our collaborators tried to substitute Sr with La during the growth in order to raise the Fermi level above the charge neutrality point, which has not been achieved yet.

We also investigated a lanthanum doped Ca_3PbO (called here $(Ca_{1-x}La_x)_3PbO$) and pristine Sr_3PbO compounds that were cleaved along the [0 0 1] direction. According to energy-dispersive X-ray spectroscopy (EDX) measurements, 5-10% of the $(Ca_{1-x}La_x)_3PbO$ compounds consisted of lanthanum, however, as we can see from the Fermi surface in the k_z *vs.* k_y plane shown in Figure 6.5(a), there are still large hole pockets on the Fermi surface, which can also be seen in the energy vs. momentum dispersion in Figure 6.5(b) along the $X - \Gamma - X$ direction (taken with 102 eV photon energy, which corresponds to the $k_z = \Gamma$ plane, as can be seen from Figure 6.5(a)). The red solid lines shown here display the calculations from Hsieh et al. (computed with the Heyd-Scuseria-Ernzerhof (HSE) hybrid-functional, which was in better agreement with the data than the DFT-PBE method), which indicated a Fermi level shift of ~350 meV due to hole doping. Comparing the calculation from Hsieh et al. for the dispersion along the $X - \Gamma - X$ direction in Sr_3PbO yields a similar shift of the Fermi level due to hole doping. Thus, similar to Sr_3SnO, also in Ca_3PbO

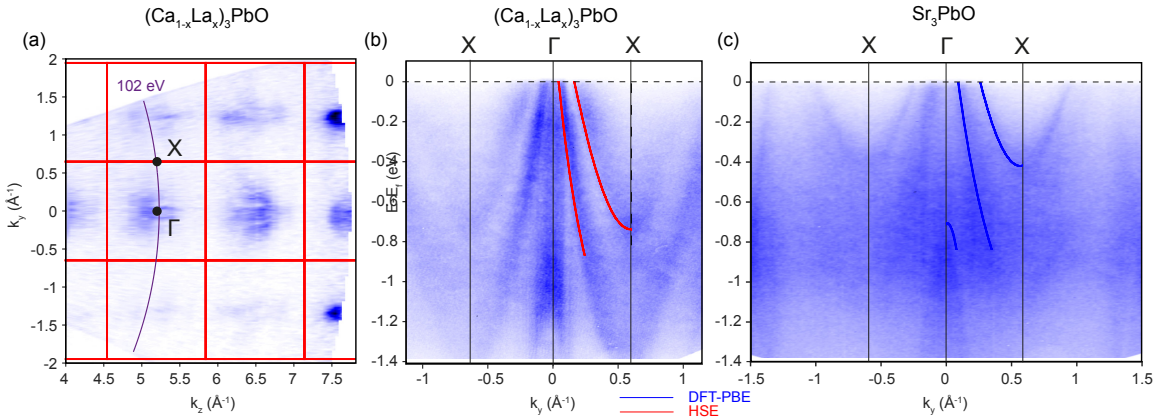


Figure 6.5: **Experimental band structure of $(Ca_{1-x}La_x)_3PbO$ and Sr_3PbO determined from their [0 0 1] cleavage planes.** (a) k_z *vs.* k_y plane for $(Ca_{1-x}La_x)_3PbO$ obtained from a photon energy dependent measurement (inner potential $V_0 = 7$ eV). The magenta line indicates the momentum position of the Fermi surface obtained at a photon energy of 102 eV, which corresponds to the $k_z = \Gamma$ plane. (b) Energy vs. momentum dispersion taken with 102 eV photon energy for $(Ca_{1-x}La_x)_3PbO$ along the $X - \Gamma - X$ direction. Red lines indicate the calculated band structure taken from Ref. [163], computed with the Heyd-Scuseria-Ernzerhof (HSE) hybrid-functional, which was shifted by ~350 meV to fit the data. (c) Energy vs. momentum dispersion taken with 148 eV photon energy for Sr_3PbO along the $X - \Gamma - X$ direction. Blue lines indicate the calculated band structure taken from Ref. [163], computed with the Perdew-Burke-Ernzerhof (PBE) functional, which was shifted by ~350 meV to fit the data. All experimental data shown here was taken with linear-horizontal polarization.

and Sr_3PbO we are unable to investigate the predicted massive Dirac cone and TCI surface states in the unoccupied states, which leaves the question whether they may be topologically nontrivial unresolved.

6.4 Discussion of the results and prospects for further study

Before we start the discussion of our results, let us briefly summarize them. We have shown that

1. Hole doped Sr_3SnO appear to have only hole pockets at Γ, but not at R, which resolves the questions raised by conflicting ab-initio predictions of its Fermi surface morphology. As a result, the superconductivity observed in hole doped Sr_3SnO should be governed by the quasiparticles at Γ, which are predicted to form bands of mixed p-d orbital character. It has been speculated that this configuration may support unconventional odd-parity superconductivity.

2. Sr_3SnO, $(Ca_{1-x}La_x)_3PbO$, and Sr_3PbO are all intrinsically hole doped compounds, possibly due to Sr or Ca vacancies. As a result, the predicted massive Dirac cones and topological crystalline surface states remain unoccupied, and therefore become inaccessible to static ARPES measurements. Hence, we were so far unable to investigate the validity of the predicted band inversion on topological crystalline phase.

The prospect of unconventional odd parity superconductivity in hole doped Sr_3SnO is certainly very exciting, since it may realize so called topological superconductivity that can host Majorana zero modes [167], quasiparticles that have unusual exchange statistics that may be exploited for fault tolerant quantum computing [169]. However, since the Fermi surface does not only consist of p-d mixed quasiparticles, also even parity pairing is possible, and further experiments will be necessary to clarify the real

pairing mechanism. If Sr_3SnO can indeed realize topological superconductivity, it may be possible to detect Majorana zero modes in vortex cores via tunneling spectroscopy, similar to the experiments recently conducted on the surface of $FeTe_{1-x}Se_x$ [170].

Due to the intrinsic hole doping of the antiperovskites, the predicted massive Dirac cones (which indicate a band inversion) and TCI surface states remain so far inaccessible for static ARPES. To overcome this limitation, laser based pump-probe ARPES may be used to initially populate and then probe the unoccupied states. This technique may be particularly suitable for the antiperovskites, since the features of interest are all located in the vicinity of the Γ point, and can therefore be probed with laser ARPES at very high momentum resolution, due to the low photon energies that are typically employed, which are in the order of 6-7 eV. Alternatively, quasi-particle interference scanning-tunneling microscopy (STM) can also be used to visualize topological surface states that are not unoccupied in the pristine compounds, as has been shown for Fermi arcs in Weyl semimetals, such as TaAs [171]. Since the cleavage surface of the single crystal antiperovskite compound is often rugged and therefore unsuitable for STM studies, it is helpful that some antiperovskites have been recently synthesized as thin films [173, 172], which may enable future experiments.

References

[153] Liang Fu. Topological Crystalline Insulators. *Physical Review Letters*, **106**:106802, Mar 2011.

[154] Yoichi Ando and Liang Fu. Topological Crystalline Insulators and Topological Superconductors: From Concepts to Materials. *Annual Review of Condensed Matter Physics*, **6**(1):361–381, 2015.

[155] Timothy H Hsieh, Hsin Lin, Junwei Liu, Wenhui Duan, Arun Bansil, and Liang Fu. Topological crystalline insulators in the SnTe material class. *Nature Communications*, **3**:982, 2012.

[156] Y Tanaka, Zhi Ren, T Sato, K Nakayama, S Souma, T Takahashi, Kouji Segawa, and Yoichi Ando. Experimental realization of a topological crystalline insulator in SnTe. *Nature Physics*, **8**:800–803, 2012.

[157] P. Dziawa, B. J. Kowalski, K. Dybko, R. Buczko, A. Szczerbakow, M. Szot, E. Lusakowska, T. Balasubramanian, B. M. Wojek, M. H. Berntsen, O. Tjernberg, and T. Story. Topological crystalline insulator states in $Pb_{1-x}Sn_xSe$. *Nature Materials*, **11**:1023, 2012.

[158] Su-Yang Xu, Chang Liu, N. Alidoust, M. Neupane, D. Qian, I. Belopolski, J. D. Denlinger, Y. J. Wang, H. Lin, L. A. Wray, G. Landolt, B. Slomski, J. H. Dil, A. Marcinkova, E. Morosan, Q. Gibson, R. Sankar, F. C. Chou, R. J. Cava, A. Bansil, and M. Z. Hasan. Observation of a topological crystalline insulator phase and topological phase transition in $Pb_{1-x}Sn_xTe$. *Nature Communications*, **3**:1192, 2012.

[159] Yoshinori Okada, Maksym Serbyn, Hsin Lin, Daniel Walkup, Wenwen Zhou, Chetan Dhital, Madhab Neupane, Suyang Xu, Yung Jui Wang, R. Sankar, Fangcheng Chou, Arun Bansil, M. Zahid Hasan, Stephen D. Wilson, Liang Fu, and Vidya Madhavan. Observation of Dirac Node Formation and Mass Acquisition in a Topological Crystalline Insulator. *Science*, **341**(6153):1496–1499, 2013.

[160] Motohiko Ezawa. Valleytronics on the surface of a topological crystalline insulator: Elliptic dichroism and valley-selective optical pumping. *Physical Review B*, **89**:195413, May 2014.

[161] Junwei Liu, Timothy H Hsieh, Peng Wei, Wenhui Duan, Jagadeesh Moodera, and Liang Fu. Spin-filtered edge states with an electrically tunable gap in a two-dimensional topological crystalline insulator. *Nature Materials*, **13**(2):178–183, 2014.

[162] Bart de Leeuw, Carolin Küppersbusch, Vladimir Juričić, and Lars Fritz. Stability of the $X - Y$ phase of the two-dimensional C_4 point group insulator. *Physical Review B*, **91**:235430, Jun 2015.

[163] Timothy H. Hsieh, Junwei Liu, and Liang Fu. Topological crystalline insulators and Dirac octets in antiperovskites. *Physical Review B*, **90**:081112, Aug 2014.

[164] Wahyu Setyawan and Stefano Curtarolo. High-throughput electronic band structure calculations: Challenges and tools. *Computational Materials Science*, **49**(2):299–312, 2010.

[165] Ching-Kai Chiu, Y-H Chan, Xiao Li, Y Nohara, and AP Schnyder. Type-II Dirac surface states in topological crystalline insulators. *Physical Review B*, **95**(3):035151, 2017.

[166] Xiuwen Zhang, Leonardo B. Abdalla, Qihang Liu, and Alex Zunger. The Enabling Electronic Motif for Topological Insulation in ABO3 Perovskites. *Advanced Functional Materials*, **27**(37):1701266–n/a, 2017. 1701266.

[167] Mohamed Oudah, Atsutoshi Ikeda, Jan Niklas Hausmann, Shingo Yonezawa, Toshiyuki Fukumoto, Shingo Kobayashi, Masatoshi Sato, and Yoshiteru Maeno. Superconductivity in the antiperovskite Dirac-metal oxide $Sr_{3-x}SnO$. *Nature Communications*, **7**:13617, 2016.

[168] Kurt Lejaeghere, Gustav Bihlmayer, Torbjörn Björkman, Peter Blaha, Stefan Blügel, Volker Blum, Damien Caliste, Ivano E. Castelli, Stewart J. Clark, Andrea Dal Corso, Stefano de Gironcoli, Thierry Deutsch, John Kay Dewhurst, Igor Di Marco, Claudia Draxl, Marcin Dułak, Olle Eriksson, José A. Flores-Livas, Kevin F. Garrity, Luigi Genovese, Paolo Giannozzi,

Matteo Giantomassi, Stefan Goedecker, Xavier Gonze, Oscar Grånäs, E. K. U. Gross, Andris Gulans, François Gygi, D. R. Hamann, Phil J. Hasnip, N. A. W. Holzwarth, Diana Iuşan, Dominik B. Jochym, François Jollet, Daniel Jones, Georg Kresse, Klaus Koepernik, Emine Küçükbenli, Yaroslav O. Kvashnin, Inka L. M. Locht, Sven Lubeck, Martijn Marsman, Nicola Marzari, Ulrike Nitzsche, Lars Nordström, Taisuke Ozaki, Lorenzo Paulatto, Chris J. Pickard, Ward Poelmans, Matt I. J. Probert, Keith Refson, Manuel Richter, Gian-Marco Rignanese, Santanu Saha, Matthias Scheffler, Martin Schlipf, Karlheinz Schwarz, Sangeeta Sharma, Francesca Tavazza, Patrik Thunström, Alexandre Tkatchenko, Marc Torrent, David Vanderbilt, Michiel J. van Setten, Veronique Van Speybroeck, John M. Wills, Jonathan R. Yates, Guo-Xu Zhang, and Stefaan Cottenier. Reproducibility in density functional theory calculations of solids. *Science*, **351**(6280), 2016.

[169] A Yu Kitaev. Fault-tolerant quantum computation by anyons. *Annals of Physics*, **303**(1):2–30, 2003.

[170] D. Wang, L. Kong, P. Fan, H. Chen, Y. Sun, S. Du, J. Schneeloch, R. D. Zhong, G. D. Gu, L. Fu, H. Ding, and H. Gao. Observation of pristine Majorana bound state in iron-based superconductor. *ArXiv e-prints*, June 2017.

[171] Hiroyuki Inoue, András Gyenis, Zhijun Wang, Jian Li, Seong Woo Oh, Shan Jiang, Ni Ni, B. Andrei Bernevig, and Ali Yazdani. Quasiparticle interference of the Fermi arcs and surface-bulk connectivity of a Weyl semimetal. *Science*, **351**(6278):1184–1187, 2016.

[172] D Samal, H Nakamura, and H Takagi. Molecular beam epitaxy of three-dimensional Dirac material Sr3PbO. *APL Materials*, **4**(7):076101, 2016.

[173] YF Lee, J Narayan, and J Schwartz. Tunable electronic structure in dilute magnetic semiconductor Sr3SnO/c-YSZ/Si (001) epitaxial heterostructures. *Journal of Applied Physics*, **116**(16):164903, 2014.

Chapter 7

Summary and conclusions

In the preface of this thesis we described two objectives for our ARPES studies presented here. One the one hand, we tried to find new materials that combine already known topological phenomena with new functionalities, or improve existing materials to enable applications. On the other hand, we attempted to discover new topological phases. In the following, we will summarize our results and conclusions under these two categories.

7.1 Investigation of new candidate materials of existing topological phases

7.1.1 ARPES study of LaBi

Our study of LaBi was motivated by the prediction of a strong topological phase in a semimetal that exhibits an extremely large magnetoresistance (XMR), which remains unsaturated at large magnetic fields. Our ARPES studies identified Dirac surface states close to the Fermi level in the surface Brillouin zone of LaBi, which experimentally verifies the theoretical prediction. This strong topological phase may be unique among the lanthanum monopnictides, since similar ARPES studies of LaSb

indicate the absence of topological surface states and a spin-orbit coupling induced band inversion, which is most likely due to the weaker spin-orbit coupling of the lighter pnictogen atom. Therefore, LaAs and LaP can also be expect to be topologically trivial.

Although a strong topological phase was already found in a large number of other compounds, our finding is still significant for two reasons. Firstly, it gives hope that topological phases may also be found in other members of the large family of rare-earth monopnictides, some of which exhibit correlation effects that may realize novel topological phenomena. Secondly, LaBi's predicted nontrivial topology was speculated to be related to its XMR effect. This hypothesis gained new relevance in light of our ARPES investigation of LaBi's electron and hole pocket volumes, which yielded a large imbalance between electron and hole carrier densities, thus casting doubts on the widely assumed perfect carrier compensation scenario as the origin of the XMR. However, it remains an open question whether the Fermi surface pocket volumes determined by ARPES give a true indication of the bulk carrier densities, or whether they can be influenced by surface effects, which may be the origin of the discrepancies between carrier densities determined by ARPES and quantum oscillations in YSb. So far, no quantum oscillation studies were able to detect a frequency component corresponding to the large outer hole pocket in LaBi, but we hope that our ARPES result will motivate improved quantum oscillation experiments that can overcome this limitation in the future, as was demonstated for LaSb.

7.1.2 ARPES study of ultrathin Ge films grown on Au(1 1 1)

The growth of ultrathin Ge films on Au(1 1 1) was motivated by reports that indicated the formation of germanene, a buckled honeycomb analogue of graphene, that may realize a quantum spin Hall phase with much larger band gap than existing materials, which could enable devices operating close to room temperature. Our ARPES measurements indicated a strong dependence of the observable band structure on the

nominal Ge film thickness (nominal meaning the thickness determined from the deposition rate, which was determined by a quartz micro balance). For films of nominal thickness of 1 Å, we observe bands that appear to be replica of the Au(1 1 1) substrate band structure. When increasing the film thickness to 2.6 Å, we observe a change of the chemical environment and structural ordering of the Ge atoms (as observed from core level and LEED images, respectively) that may indicate the formation of a bulk environment, and may signify the completion of at least one monolayer. In this limit, Dirac-like conical linear bands emerge, which may originate from replicated Dirac cones of rotationally disordered germanene, or which may be yet another replication of the substrate bands. Those cones also persist in thicker films of nominally 7.2 Å.

Although our discovery of the Dirac-like conical bands may be exciting and offer hope that the synthesis of germanene on Au(1 1 1) may be possible, the lack of knowledge about the microscopic crystal structure of those films make it challenging to pin down the precise origin of the Dirac-like bands. The early excitement about Dirac-like bands in ultra thin films of silicon, which initially were considered to originate from silicene, but were subsequently attributed to the silver substrate, should serve as a warning not to overinterpret the significance of ARPES spectra without additional structural information. However, our findings should serve as a strong motivation for future experiments with techniques more suitable to determine the atomic arrangement of these ultrathin Ge films, such as scanning probe microscopy or grazing incidence XRD.

7.1.3 ARPES study of hole doped Sr_3SnO, Ca_3PbO, and Sr_3PbO

The antiperovskite family A_3BO (A=Sr, Ca; B=Sn, Pb) is predicted to represent topological crystalline insulators (TCI) that are characterized by a nonzero mirror Chern number and hosts topological surface states that are protected by mirror symmetries. Although TCIs are not uncommon, there is so far no experimental verification of a topological oxide, which makes these antiperovskites interesting candidates to

study the interplay of topology and oxide functionality. However, the as-grown compounds Sr_3SnO, Ca_3PbO, and Sr_3PbO are intrinsically hole doped, which leaves the predicted bulk and surface Dirac cones unoccupied and thus inaccessible for ARPES. All attempts to electron dope the samples, for instance with lanthanum, were so far unsuccessful. The topological character of the antiperovskites therefore remains unverified. However, the very good agreement of the measured band structure and the ab-initio calculations gives hope that other techniques – which can probe unoccupied states, such as pump-probe ARPES or scanning tunneling spectroscopy – will be able to confirm the predicted TCI phase. Moreover, our ARPES measurements of hole doped Sr_3SnO, which exhibits superconductivity, indicate the absence of a hole pocket at the R-point of the Brillouin zone, which resolves conflicting predictions in the literature. The parity of the Cooper pair wave function will therefore only be determined by the orbital character of the bands in the vicinity of the Γ-point, which are predicted to be of mixed p-d orbital character, and could therefore realize elusive odd-parity superconductivity that may display the exotic physics of Majorana zero modes in vortex cores. However, the possibility of odd-parity pairing remains so far a theoretical prediction that is purely based on band structure calculations, but lacks any experimental foundation. Further experimental investigations along the lines of other odd-parity pairing candidates, such as Sr_2RuO_4, can be expected.

7.2 Discovery of a weak topological phase in a family of transition-metal dipnictides

The possibly most interesting result reported in this thesis is our ARPES investigation of $TaSb_2$, which is a member of a transition-metal dipnictide family that was predicted to host a weak topological phase. Topological insulators (TIs) can be divided into two classes, strong TIs that host topological surface states on all surfaces, and weak TIs, which host topological surface states (TSSs) only on some surfaces. Since it

was initially assumed that disorder would localize the TSSs in weak TIs without breaking time-reversal symmetry, weak TIs became the neglected siblings of their strong counter parts. Although subsequent theoretical studies rehabilitated their reputation by predicting a multitude of unique phenomena, the layered nature of most weak TI candidates made it impossible to investigate their topological surface states, since all cleaved surfaces turned out to be trivial. With the advent of topological Dirac and Weyl semimetals, interest faded and the field moved on, leaving the rich physics of weak TIs largely unexplored.

What distinguishes $TaSb_2$ from other weak TI material candidates is that it can be cleaved on multiple surfaces. We utilized this property to measure its surface electronic structure on the [1 1 1] surface, which hosts only trivial surface states, and the [0 0 1] surface, which hosts topological surface states. By combining the information from both surfaces we can conclusively determine the topological index of $TaSb_2$, despite the fact that trivial bulk pockets are covering a time-reversal invariant moment on the [0 0 1] surface, thus making it impossible to track the TSSs in its vicinity. The similarity of the surface states on the [0 0 1] surface of $TaAs_2$ and $NbAs_2$ to the ones in $TaSb_2$ suggest that they are also topologically nontrivial.

We can therefore report the experimental verification of a weak topological phase, which to the best of our knowledge was not reported before. However, the existing transition-metal dipnictide material family has the severe limitation to posses only a local, but no global energy gap. As a result, trivial bulk electrons will presumably always dominate transport measurements, which may hinder the observation of the exotic phenomena predicted for weak TIs. Increasing spin-orbit coupling by elemental substitution may be a route to realize a global gap (since $TaSb_2$ has less bulk pockets than $TaAs_2$ and $NbAs_2$, according to the calculations), but the even heavier compound $TaBi_2$ has not been synthesized yet. Alternatively, strain (epitaxial or otherwise) or chemical pressure may tune the bandstructure, but should leave the topological classification intact, as long as the local band gap does not close. Thus, there could

be many routes to realize a weak TI candidate that has a global gap, but has a cleavage plane that leaves its topological surface states accessible for ARPES (see also our speculations at the end of chapter 4). We challenge the reader to find a good candidate.